ASTES

Advances in Science, Technology & Engineering Systems Journal

VOLUME 10-ISSUE 1|JAN-FEB 2025

www.astesj.com
ISSN: 2415-6698

Editorial

In the evolving landscape of science and engineering, multidisciplinary research continues to push boundaries, drive innovation, and address pressing technological and societal challenges. The current issue of our journal highlights a diverse collection of studies that exemplify this spirit of inquiry, presenting solutions to real-world problems ranging from power systems to pharmaceutical formulations, from AI integration in education to cryptographic resilience in mobile networks. Each contribution provides significant theoretical or practical advancements, reflecting the collaborative effort and intellectual rigor of the global research community.

A novel lightning detection system tailored for wind turbine applications is developed using a large-diameter Rogowski coil paired with an analog integrator. The coil, with a lower cutoff frequency of 0.1 Hz, and the integrator circuitry effectively reconstruct the original lightning current waveform. Verified across a range of current types—including AC, damped sinusoidal, and rectangular pulses—the system offers a broad bandwidth from 0.1 Hz to 100 kHz. This makes it not only compliant with standard performance criteria but also cost-efficient, positioning it as a viable alternative to commercial lightning detection systems [1].

A comprehensive physicochemical stability analysis of extemporaneous omeprazole-based formulations identifies environmental and compositional factors influencing drug shelf life. The study utilizes a 2k factorial design with temperature, luminosity, and diluent type as variables. Physiological saline solution emerges as the most stable and accessible diluent, offering a shelf-life of over five hours under optimal conditions. The findings underscore the critical importance of evaluating environmental conditions prior to drug administration to ensure patient safety and treatment efficacy [2].

Addressing the pedagogical challenges faced by digital universities in Africa, an exploration into the use of AI-powered chatbots reveals their potential to transform learner-content interaction. By leveraging platforms such as Rasa and Moodle, the study presents a model where chatbots facilitate personalized learning, improve student engagement, and support formative assessments. Comparative analysis of different chatbot frameworks further illuminates the technological considerations necessary for seamless integration, reinforcing the role of intelligent systems in reducing dropout rates and enhancing academic outcomes [3].

The physical principles underpinning rotor slot skewing in squirrel-cage induction machines are rigorously analyzed, leading to a set of derived formulas that account for synchronous and asynchronous parasitic torques. Through comparative analysis of magnetic motive force (MMF) curves and detailed case studies, the study provides a theoretical framework for targeted skew application. The development of theorems on residual torque and differential leakage attenuation marks a significant advancement in the precise and noise-mitigated design of induction machines [4].

In an era where mobile data transmission faces increasing threats, an enhanced ZUC algorithm is proposed to reinforce LTE network security using chaos-based dynamic S-boxes. The updated algorithm generates highly randomized key streams and demonstrates superior resistance to cryptographic attacks. Implemented on a Xilinx FPGA platform, the architecture proves both resource-efficient and high-performing, achieving a throughput of over 2500 Mbps. This design not only meets modern data protection demands but also aligns with the constraints of real-time mobile applications [5].

To address the complexities of handwritten text line segmentation in Myanmar scripts, a segmentation method based on average linkage clustering is proposed. Utilizing connected

component analysis and convex hull re-segmentation, the system adeptly handles overlapping characters and irregular line spacing. With high Intersection over Union (IU) scores on two datasets, the method outperforms existing clustering algorithms such as DBSCAN, thus representing a robust solution for enhancing optical character recognition (OCR) in complex handwritten scripts [6].

Expanding the analytical framework of rotor slot number selection for 5-phase motors, this study applies a previously validated method across a comprehensive range of machine configurations. By incorporating the Noise Component Equivalence Measure, the analysis allows precise prediction of torque oscillations and acoustic noise, guiding optimal rotor slot number decisions. The resulting design rules are systematic and adaptable to various stator and pole configurations, offering an unprecedented level of granularity and predictability in multiphase motor design [7].

In summary, the papers featured in this issue collectively demonstrate the ingenuity and relevance of applied research in addressing modern engineering and technological challenges. From ensuring power system integrity and secure data transmission to optimizing educational outcomes and mechanical design, these studies not only advance their respective fields but also offer scalable and practical solutions. It is our hope that these contributions will inspire further innovation and interdisciplinary collaboration.

References:

[1] S. Pramualsingha, K. Yamamoto, R. Tanaka, “Lightning Detection System for Wind Turbines Using a Large-Diameter Rogowski Coil,” Advances in Science, Technology and Engineering Systems Journal, 10(1), 1–6, 2025, doi:10.25046/aj100101.

[2] E. Cruz-Pérez, J. Locia-Espinoza, J.J. Díaz-Vallejo, M.O. Pérez-Vásquez, L.M. de la Vega, L.I. Pascual-Mathey, “Evaluation of physicochemical stability in extemporaneous omeprazole-based preparations,” Advances in Science, Technology and Engineering Systems Journal, 10(1), 7–12, 2025, doi:10.25046/aj100102.

[3] K. Sylla, B. Babou, M. Amar, S. Ouya, “Impact of Integrating Chatbots into Digital Universities Platforms on the Interactions between the Learner and the Educational Content,” Advances in Science, Technology and Engineering Systems Journal, 10(01), 13–19, 2025, doi:10.25046/aj100103.

[4] G. Kovács, “Analytical Study on the Effect of Rotor Slot Skewing on the Parasitic Torques of the Squirrel Cage Induction Machine,” Advances in Science, Technology and Engineering Systems Journal, 10(1), 20–36, 2025, doi:10.25046/aj100104.

[5] M. Madani, E.-B. Bourennane, S. El Assad, “Hardware and Secure Implementation of Enhanced ZUC Steam Cipher Based on Chaotic Dynamic S-Box,” Advances in Science, Technology and Engineering Systems Journal, 10(1), 37–47, 2025, doi:10.25046/aj100105.

[6] N. Phyo Wai, N. War, “Text Line Segmentation on Myanmar Handwritten Document using Average Linkage Clustering Algorithm,” Advances in Science, Technology and Engineering Systems Journal, 10(1), 48–59, 2025, doi:10.25046/aj100106.

[7] G. Kovács, “Selection of Rotor Slot Number in 3-phase and 5-phase Squirrel Cage Induction Motor; Analytic Calculation,” Advances in Science, Technology and Engineering Systems Journal, 10(01), 60–74, 2025, doi:10.25046/aj100107.

Editor-in-chief

Prof. Passerini Kazmersk

ADVANCES IN SCIENCE, TECHNOLOGY AND ENGINEERING SYSTEMS JOURNAL

Volume 10 Issue 1 January-February 2025

CONTENTS

Advances in Science, Technology and Engineering Systems Journal Vol. 10, No. 1, 01-06 (2024)

www.astesj.com

Special Issue on Computing, Engineering and Multidisciplinary Sciences 2024

ASTESJ

ISSN: 2415-6698

Lightning Detection System for Wind Turbines Using a Large-Diameter Rogowski Coil

Sarawuth Pramualsingha*, Kazuo Yamamoto, Rikuto Tanaka

Graduate School of Electrical and Electronic Engineering, Chubu University, Kasugai, 487-8501, Japan

ARTICLE INFO

Article history:
Received: 15 March, 2024
Revised: 31 December, 2024
Accepted: 01 January, 2025
Online: 16 January, 2025

Keywords:
Lightning detection
Wind turbines
Large-diameter Rogowski coil
Wideband integrator
High-current measurement

ABSTRACT

A lightning detection system based on a large-diameter Rogowski coil and an analog integrator was developed for wind turbine applications and is presented in this paper. To accurately detect lightning current, the Rogowski coil was designed with a lower cutoff frequency of 0.1 Hz. The analog integrator, comprising an inverting active integrator, and an amplifier, was used to restore the original waveform of the lightning current. Tests were conducted to verify the bandwidth of the system using alternating current, damped sinusoidal current, and a rectangular pulse. The system demonstrated a bandwidth of 0.1 Hz to 100 kHz, which is within the standard acceptable range. This lightning detection system offers a significantly lower cost compared to commercial alternatives, making it highly suitable for practical applications.

1. Introduction

For sustainable development and achieving carbon neutrality, wind turbines are increasingly being used for power generation [1]. Over the past decade, Japan has been the second-largest wind power installer in the world, with a cumulative capacity of 5,213 MW [2]. Wind turbines operate effectively in areas with strong winds, such as coastal or offshore locations, but this also places them at a high risk of being struck by lightning [3]-[5]. It is important to stop wind turbines and perform manual inspections after a lightning event is detected to prevent further damage and ensure safety. To achieve this, a lightning detection system (LDS) is deployed to identify such events.

As stated by the JEM and IEC standards [6],[7], the LDS consisting of a large-diameter Rogowski coil and an analog integrator is one of the alternative methods for the detection of lightning events. In practice, this coil is securely installed at the wind turbine tower near the foundation, wrapped around its exterior. This configuration allows the detection of impulse current from the tower.

Rogowski coil induces voltage is proportional to the time derivative of the lightning current (i_l), and its transfer function exhibits a positive slope gain. To retrieve the original shape of the lightning current i_l and maintain its gain constantly, an analog integrator is used. It has a negative slope gain in its transfer function, which cancels out the slope gain of the Rogowski coil.

In this paper, a cost-effective lightning detection system for wind turbine applications is presented. The system has a bandwidth of 0.1 Hz to 100 kHz and comprises a large-diameter Rogowski coil and an analog integrator. The design details are presented in Section 2. Frequency characteristic tests were performed to ensure sufficient bandwidth and are presented in Sections 3 and 4. Finally, the conclusion is presented in Section 5.

2. Lightning Detection System

The possibility of a lightning strike at the blade tip of wind turbines is high, as it typically becomes the highest point during operation. A permanently mounted air-termination system, known as a receptor, serves as the contact point between wind turbines and lightning [7]. Once lightning strikes, lightning current i_l flows from the receptor, a down-conducting system, wind turbine tower, and eventually reaches an earth-termination system at a foundation, as illustrated in Figure 1.

As lightning current i_l flows to the earth-termination system, it generates a time-varying magnetic field (B) around its conductor. This enables current sensors, such as the Rogowski coil, to detect lightning events if installed anywhere along this current path.

Commercially available Rogowski coil-based LDS units can cost a million yen or more each. In contrast, the developed LDS has a total cost of approximately 33,000 yen, comprising 23,000

*Corresponding Author: Sarawuth Pramualsingha, Chubu University, sarawuth.pr@kmitl.ac.th

https://dx.doi.org/10.25046/aj100101

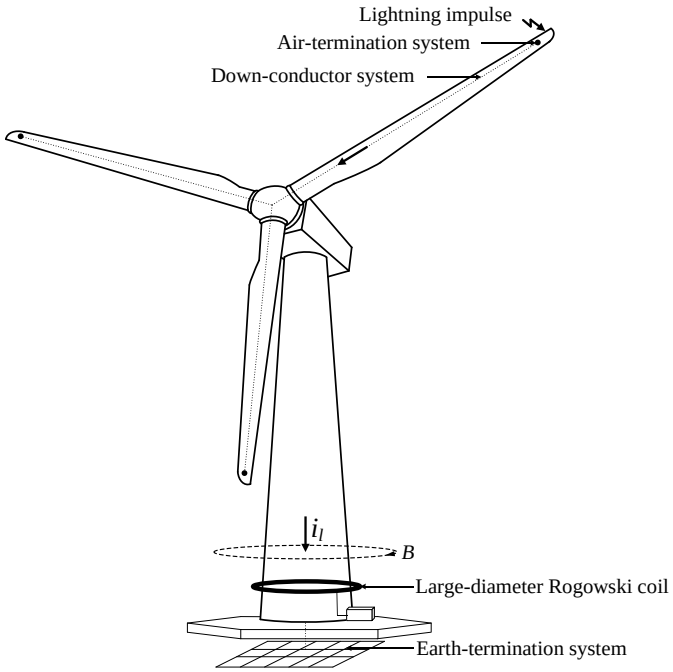

Figure 1: Wind turbine lightning protection system components and the location of the Rogowski coil-based lightning detection system [7].

yen for the large-diameter Rogowski coil and 10,000 yen for the analog integrator making them significantly cost-effective.

Since the output voltage from the Rogowski coil feeds into the integrator, the frequency characteristics of the LDS can be analyzed by multiplying the Rogowski coil transfer function $H_r(s)$ and the integrator transfer function $H_i(s)$ as in (1)

$$H_l(s) = H_r(s) \cdot H_i(s) \tag{1}$$

Details for obtaining the Rogowski coil and integrator transfer function are as follows.

2.1. Large-diameter Rogowski coil

Rogowski coils were introduced in 1912 by German physicist [8]. For simplicity in investigation, it is modeled using lumped parameters, as illustrated in Figure 2, where M represents mutual inductance, L_s represents self-inductance, R_s represents self-resistance, C_s represents stray capacitance, R_d represents damping resistance, i_2 represents coil loop current, and v_r represents the coil output voltage [9]. Applying Kirchhoff's voltage law, loop voltage is

$$M\, di_l(t)/dt = L_s\, di_2(t)/dt + R_s i_2(t) + v_r(t) \tag{2}$$

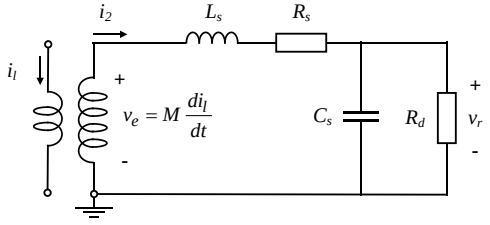

Figure 2: Lumped parameter equivalent circuit of the large-diameter Rogowski coil [9].

Assume that $L_s \cdot di_2(t)/dt \gg R_s \cdot i_2(t) + v_r(t)$, and stray capacitance C_s are neglected, so voltage drops across self-resistance R_s and damping resistance R_d can be neglected. Hence, loop current $i_l(t) \approx L_s \cdot i_2(t)/M$. This type of coil is known as a self-integrating Rogowski coil, suitable for detecting very short-duration current pulses [10].

To obtain the coil output voltage in the time domain $v_r(t)$, apply Kirchhoff's current law, and the current loop is

$$i_2(t) = C_s\, dv_r(t)/dt + v_r(t)/R_d \tag{3}$$

Substitute (3) into (2) and then apply integration with respect to time (t). In practice, stray capacitance C_s and L_s / R_d are assumed to be approximately zero. The voltage drops across self-inductor L_s and the current consumed by stray capacitor C_s can, therefore, be neglected. Thus,

$$i_l(t) \approx (R_s + R_d/R_d\, M) \int_{t=0}^{t=\infty} v_r(t)dt \tag{4}$$

From (4), lightning current i_l can be reconstructed using an external integrator. This type of Rogowski coil is known as an external-integrating Rogowski coil, which is suitable for relatively long-duration current pulses and was utilized as part of LDS in this study [11].

The frequency characteristics of Rogowski coils can be determined from their transfer function by substituting (3) into (2) and applying Laplace transform. The transfer function of the Rogowski coil, $H_r(s)$, is

$$H_r(s) = sMR_d \Big/ \left(s^2 L_s C_s + sL_s + sR_s C_s R_d + R_s + R_d\right) \tag{5}$$

Rogowski coil is a helical toroidal coil of wire. Lead from one end returns to another end through the center of the helical coil. Hence, both terminals are positioned at the same end. Mutual inductance M, self-inductance L_s, stray capacitance C_s, and self-resistance R_s can be calculated from its dimensions as in (6) to (9), respectively [12]-[15].

$$M = \left(\mu_0 N/2\right)\left(\sqrt{r_o} - \sqrt{r_i}\right)^2 \tag{6}$$

$$L_s = MN \tag{7}$$

$$R_s = \frac{\rho}{A}\left[\pi\left(r_i + r_o\right) + N\pi\sqrt{\left(\left(r_o + r_i\right)/N\right)^2 + \left(r_o - r_i\right)^2}\right] \tag{8}$$

$$C_s = 4\pi^2 \varepsilon_0 (r_o + r_i) \Big/ \log_{10}\left((r_o + r_i)/(r_o - r_i)\right) \tag{9}$$

Where r_i is the coil inner radius, r_o is the coil outer radius, N is the number of turns, u_0 is the permeability of free space ($4\pi \times 10^{-7}$ H/m), ε_0 is the permittivity of free space (8.85×10^{-12} F/m), and ρ is the resistivity of the coil wire.

The developed large-diameter Rogowski coil has an inner radius r_i of 2 m, allowing it to wrap around the tower of a wind

turbine. To achieve a bandwidth of 0.1 Hz to 100 kHz, Rogowski coils are designed with an outer radius r_o of 2.04 m and 1400 turns. The coil, made from commercially available wire-reinforced PVC ducting with a diameter of 40 mm, costs approximately 23,000 yen. Aluminum wire is used for the coil, with a cross-sectional area of 1.78×10^{-8} m² and resistivity ρ of 2.7×10^{-8} Ω/m. The damping resistance R_d is derived from the impedance of an RG-58 50 Ω coaxial cable, resulting in an infinite damping resistance R_d. From (6) to (9), mutual inductance M, self-inductance L_s, stray capacitance C_s, and self-resistance R_s are calculated as 15.65 µH, 0.22 mH, 766 pF, and 291.3 Ω, respectively. The gain and phase characteristics of the coil, analyzed by (5), are shown in Figure 4 and 5 respectively. It exhibits a linear gain slope of approximately 20 dB/decade and a phase shift of roughly -90 degrees for a frequency range from 0.1 Hz to 100 kHz, which satisfies the target range. The external integrator used with the Rogowski coil has been designed to cancel out the coil gain slope, and the detailed design is presented in the following section.

2.2. Analog Integrator

Analog integrators for the Rogowski coil serve two purposes: to regain the original shape of the lightning current i_l and to maintain a constant gain. In previous studies, integrators were usually designed with two poles and one or no zeros [10],[16],[17]. The interaction between poles can lead to more complex dynamic behavior in the integrator [18]. The analog integrator used in this study is shown in Figure 3. It is designed to have a single pole with no zero, resulting in more predictable and stable behavior. The analog integrator consists of an inverting active integrator and an amplifier. Bias resistors R_2 and R_3 minimize the effect of offset voltage, while R_5 and R_8 limit the bias current. The amplifier circuit is utilized to make it more effective for the digital recorder to record the output voltage v_o.

Let V_n and V_p denote inverting and non-inverting operational amplifier (Op-amp) terminal voltages, respectively, with respect to ground. I_n and I_p denote bias currents entering inverting and non-inverting Op-amp terminals, respectively. For simplicity in analysis, let $V_p \approx V_n$, $I_p \approx 0$, and $I_n \approx 0$ [19]. The transfer function of the developed analog integrator, $H_i(s)$, is

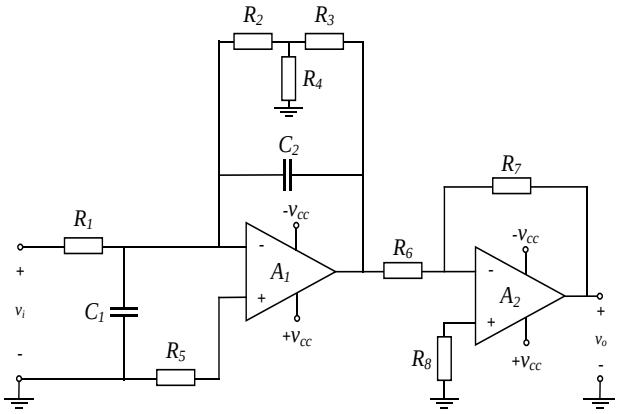

Figure 3: Developed analogue integrator.

$$H_i(s) = \frac{R_3/R_1 + R_2/R_1 + R_2R_3/R_1R_4}{1 + s\left(C_2R_3 + C_2R_2 + C_2R_2R_3/R_4\right)} \cdot \frac{R_7}{R_6} \tag{10}$$

To achieve a gain of about -20 dB/decade and phase shift of -90 degrees from a frequency of 0.1 Hz to 100 kHz, circuit parameters for R_1, C_1, R_2, R_3, R_4, R_5, C_2, R_6, R_7, and R_8 were set to 10 kΩ, 2.25 µF, 200 kΩ, 200 kΩ, 100 kΩ, 6.8 kΩ, 2.25 µF, 10 kΩ, 100 kΩ, and 10 kΩ, respectively. Resulting in a pole at approximately -0.556, ensuring the stability of the system. LT112 operational amplifiers were used for both Op-amps A_1 and A_2 due to their high slew rate of 60 V/µs. Power supplies were used. An output voltage was set to 15 V_{DC} and -15 V_{DC} for V_{cc} and V_{ee}, respectively. The overall cost of assembling the analog integrator was approximately 10,000 yen. The frequency characteristics of the developed integrator, analyzed by (10), show a linear gain slope of -20 dB/decade and a phase shift of approximately -90 degrees as illustrated in Figure 6 and 7 respectively for the frequency range of 0.1 Hz to 100 kHz, which satisfies the target range.

3. LDS Frequency Characteristic Test

Frequency characteristic tests were performed to verify that LDS is capable of measuring lightning current i_l without attenuation or phase error. To ensure that each component in the LDS is functioning as designed, three separate frequency characteristic tests were conducted: a bandwidth test on the large-diameter Rogowski coil, the analog integrator, and the LDS.

To demonstrate the alignment between the test results and the analysis, the assessment includes the calculation of the maximum relative error (MRE), defined as

$$MRE = \max_{i=1}^{n} \left| \frac{\hat{y}_i - y_i}{\hat{y}_i} \right| \tag{11}$$

where $\hat{y}_i$ and y_i represent the ith element of analysis and test result, and n is the total number of considered data points [20].

3.1. Frequency Characteristic Test of the Rogowski Coil

The test was conducted using alternating current (AC) voltage as recommended by the JEM standard [6]. A sinusoidal waveform from a function generator and a bipolar voltage amplifier were used to generate a variable-frequency voltage. A sufficient bandwidth shunt resistor (R_{sh}) was employed to draw current from the source and serve as a reference current measuring point. Schematic for the test is shown in Figure 8, with the analog integrator removed. The test results for gain and phase shift are presented in Figures 4 and 5 respectively.

At frequencies lower than 100 kHz, the MRE of gain and phase is 0.31 and 0.11, occurring at frequencies of 50 kHz and 1 Hz, respectively, demonstrating good alignment between the analysis and test results. At frequencies higher than 100 kHz, the stray capacitance between each turn of the coil wire becomes significant, impacting the coil characteristics and resulting in large errors between the analysis and test results. However, these frequencies are beyond the intended use and do not affect the overall performance of the LDS.

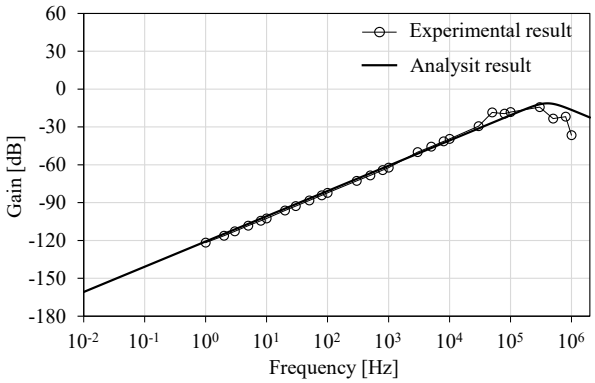

Figure 4: Analysis and test results of gain characteristics of the developed large-diameter Rogowski coil.

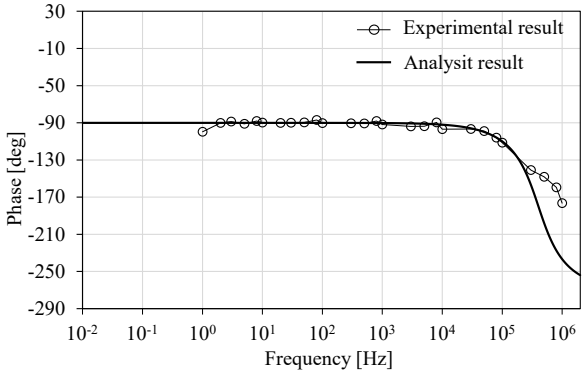

Figure 5: Analysis and test results of phase shift characteristics of the developed large-diameter Rogowski coil.

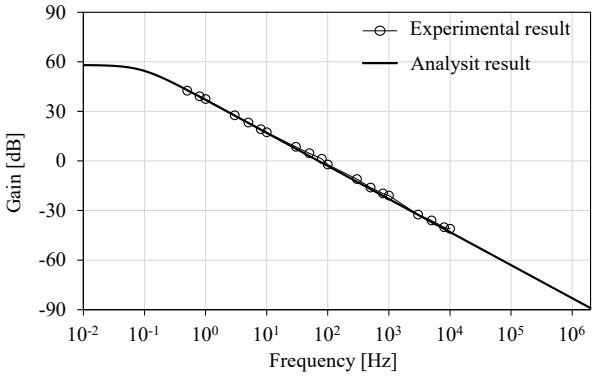

Figure 6: Analysis and test results of gain characteristics of the developed analog integrator.

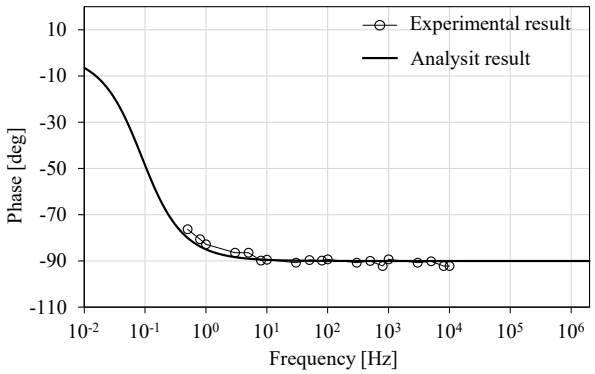

Figure 7: Analysis and test results of phase shift characteristics of the developed analog integrator.

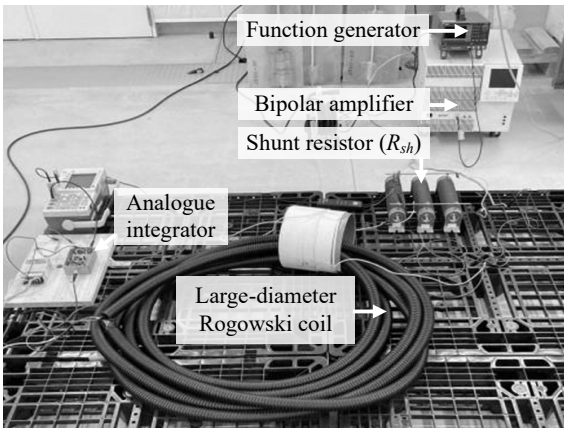

(a)

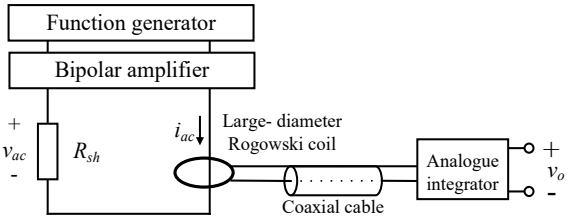

(b)

Figure 8: Alternating current (AC) power circuit and LDS under test: (a) Actual test setup, (b) Schematic diagram.

3.2. Frequency Characteristic Test of Analogue Integrator

To assess the frequency characteristics of the developed analog integrator, a sinusoidal waveform from a function generator was directly applied to the integrator. Comparing the amplitude of the input and output voltages, the test results for gain and phase shift are presented in Figures 6 and 7 respectively. MSE is 2.25 and 0.04 for gain and phase at frequencies of 80 Hz and 0.8 Hz respectively ensuring well alignment of analysis and the test results.

3.3. Frequency Characteristic Test of LDS

Frequency characteristic testing of LDS was divided into two ranges: below 30 kHz and above 30 kHz. The test schematic and actual test are depicted in Figure 8. Test results for gain and phase shift are shown in Figures 9 and 10, respectively. Analysis using (1) and test results are well aligned. For frequencies below 100 kHz, the MSE of gain and phase is 0.04 and 0.08, occurring at approximately 30 kHz and 100 kHz, respectively. At higher frequencies, the analog integrator components exhibit bandwidth limitations. However, these frequencies are beyond the range of interest and will not affect the LDS performance in practical use. The test details are as follows.

- LDS test at a frequency below 30 kHz, the test was conducted with its schematic and actual test configuration depicted in Figure 8, using AC voltage as a source. Input current and output voltage were measured to determine gain and phase shift.
- LDS test at a frequency above 30 kHz, a relatively high current is required to assess frequency characteristics. To overcome this challenge, tests were conducted using damped alternating current (DAC), the waveform suggested as an alternative by the JEM standard [6].

alternative by the JEM standard [6].

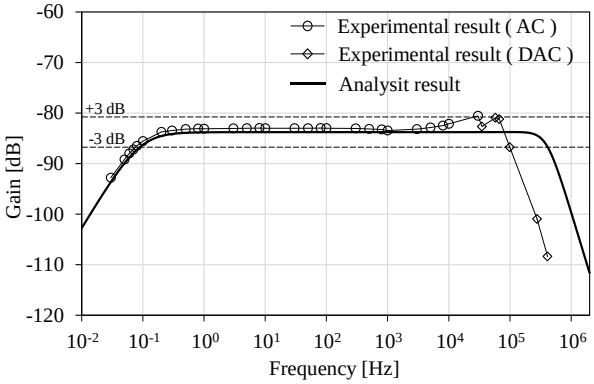

Figure 9: Analysis and test results of gain characteristics of the LDS.

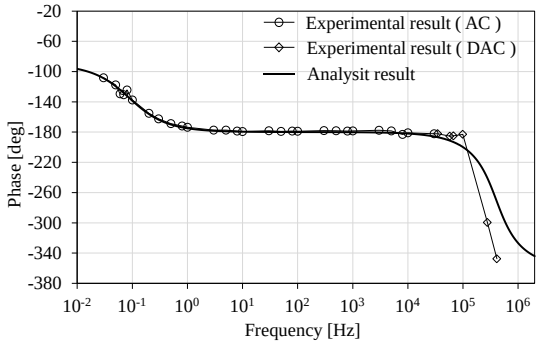

Figure 10: Analysis and test results of phase shift characteristics of the LDS.

4. LDS Low Cutoff Frequency Verification

A low cutoff frequency of LDS is a crucial parameter as it directly impacts measurements of total charge. To verify the cutoff frequency, a rectangular pulse response of LDS is compared to that of a known low-pass filter with a specific cutoff frequency.

Due to its sharp transitions, a rectangular pulse contains a broad spectrum of sinusoidal frequencies. When applied to a low-pass filter, the flat top of the pulse gradually decays toward zero. The higher the cutoff frequency, the faster this decay occurs. To confirm the cutoff frequency of the LDC at 0.1 Hz, a first-order low-pass filter with a cutoff frequency of about 0.08 Hz was selected. The filter was composed of a 15 kΩ resistor and a 130 µF capacitor [21].

The test was conducted as schematic shown in Figure 11. The pulse had an amplitude of approximately 1000 A and a duration of 450 ms. The reference pulse response was obtained by replacing the LDS with the filter. Input current and output voltage were measured, and the results, shown in Figure 12, demonstrate good alignment for the time range of approximately 0 to 450 ms. This confirms that the LDS has a lower cutoff frequency of at least about 0.08 Hz, meeting the intended design specification of 0.1 Hz.

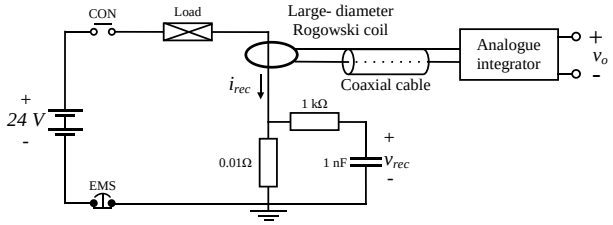

Figure 11: Schematic of rectangular pulse power circuit and LDS under test.

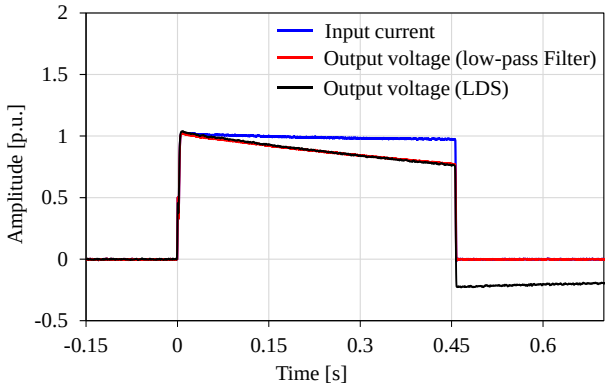

Figure 12: Rectangular pulse response of the LDS and the reference low-pass filter.

5. Conclusion

A lightning detection system for wind turbine applications is presented in this paper. The system consists of the large-diameter Rogowski coil and the analog integrator. It operates with a bandwidth range of 0.1 Hz to 100 kHz and a linear gain of approximately -83 dB. The developed large-dimeter Rogowski coil is designed with a diameter of 4 m, 1400 turns in total, and a slope of 20 dB/decade. The developed analog integrator has a slope gain of -20 dB/decade and consists of the inverting active integrator and an amplifier.

A series of tests were conducted to assess the frequency characteristics of the LDS, particularly the lower and upper cutoff frequencies. LDS frequency characteristics were measured using alternating current (AC) for frequencies below 30 kHz and damped alternating current (DAC) for higher frequencies. The results align well with the analysis, with a maximum gain error of less than 3 dB, confirming the upper cutoff frequency to be 100 kHz. Additionally, the lower cutoff frequency of the LDS was verified using a rectangular pulse response, confirming that it is lower than 0.1 Hz.

The developed LDS complies with the standard required bandwidth while offering significant cost-effectiveness compared to commercial alternatives. This makes the LDS suitable for field applications in lightning detection for wind turbines.

Acknowledgment

Authors would like to give special acknowledgment to High Voltage Laboratory, Graduate School of Electrical and Electronic Engineering, Chubu University for the support and facilities.

References

[1] G. Council, "GWEC global wind report 2019," *Global Wind Energy Council*, **(2017)**: [page numbers missing], 2017

[2] G. Council, "GWEC global wind report 2024," *Global Wind Energy Council*, **(2024)**: [page numbers missing], 2024

[3] K.L. Cummins, "Overview of the Kansas Windfarm 2013 Field Program," *Lightning Detection Conference, Vaisala*, **(2014)**: [page numbers missing], 2014

[4] D. Wang, N. Takagi, T. Watanabe, H. Sakurano, M. Hashimoto, "Observed characteristics of upward leaders that are initiated from a windmill and its lightning protection tower," *Geophysical Research Letters*, **35(2)**: [page numbers missing], 2008

[5] M. Ishii, M. Saito, M. Chihara, D. Natsuno, "Transferred charge and specific energy associated with lightning hitting wind turbines in Japan," *IEEJ Transactions on Power and Energy*, **132(3)**: 294–295, 2012

[6] N.P.G.S. Lightning current detection-Part, "1515: Test methods of Lightning current detection system for wind turbines," *The Japan Electrical Manufacturers' Association, JEM*, **(2023)**: 1515, 2023

[7] W. Turbines-Part, "24: Lightning protection," *International Electrotechnical Commission, IEC*, **(2010)**: 61400-24, 2010

[8] W. Rogowski, W. Steinhaus, "Die messung der magnetischen spannung," *Electrical Engineering (Archiv für Elektrotechnik)*, **1(4)**: 141–150, 1912

[9] I.T. Transformers-Part, "10: Lightning protection," *International Electrotechnical Commission, IEC*, **(2017)**: 61869-10, 2017

[10] Y. Liu, F. Lin, Q. Zhang, H. Zhong, "Design and construction of a Rogowski coil for measuring wide pulsed current," *IEEE Sensors Journal*, **11(1)**: 123–130, 2010

[11] W. Li, C. Mao, J. Lu, "Study of the virtual instrumentation applied to measure pulsed heavy currents," *IEEE Transactions on Instrumentation and Measurement*, **54(1)**: 284–288, 2005

[12] G. Robles, M. Argueso, J. Sanz, R. Giannetti, B. Tellini, "Identification of parameters in a Rogowski coil used for the measurement of partial discharges," *IEEE Instrumentation & Measurement Technology Conference*, **(2007)**: 1–4, 2007

[13] J. Hlavacek, R. Prochazka, K. Draxler, V. Kvasnicka, "The Rogowski coil design software," *IMEKO TC4 International Symposium*, **(2008)**: 295–300, 2008

[14] M. Xiang, H. Gao, B. Zhao, C. Wang, C. Tian, "Analysis on transfer characteristics of Rogowski coil transducer to travelling wave," *International Conference on Advanced Power System Automation and Protection*, **2**: 1056–1059, 2011

[15] M. Rezaee, H. Heydari, "Mutual inductances comparison in Rogowski coil with circular and rectangular cross-sections and its improvement," *IEEE Conference on Industrial Electronics and Applications*, **(2008)**: 1507–1511, 2008

[16] W. Limcharoen, P. Yutthagowith, "Rogowski coil with an active integrator for measurement of switching impulse current," *International Conference on Electrical Engineering/Electronics, Computer, Telecommunications and Information Technology*, **(2013)**: 1–4, 2013

[17] B. Wang, D. Wang, W. Wu, "A Rogowski coil current transducer designed for wide bandwidth current pulse measurement," *International Power Electronics and Motion Control Conference*, **(2009)**: 1246–1249, 2009

[18] K. Ogata, *Modern Control Engineering*, United Kingdom: Prentice Hall, 2010

[19] C.K. Alexander, M.N.O. Sadiku, M. Sadiku, *Fundamentals of Electric Circuits*, Boston, MA, USA: McGraw-Hill Higher Education, 2007

[20] J.D. Hoffman, S. Frankel, *Numerical Methods for Engineers and Scientists*, CRC Press, 2018

[21] D. Chattopadhyay, P.C. Rakshit, *Fundamentals of Electric Circuit Theory*, S. Chand Publishing, 2000

Advances in Science, Technology and Engineering Systems Journal Vol. 9, No. 1, 7-12 (2025)

www.astesj.com

Special Issue on Innovation in Computing, Engineering Science & Technology 2024-25

ASTESJ

ISSN: 2415 6698

Evaluation of Physicochemical Stability in Extemporaneous Omeprazole-Based Preparations

Ezri Cruz-Pérez[1,2], José Locia-Espinoza[1,2], Joel Jahaziel Díaz-Vallejo[1,2,3], Magda Olivia Pérez-Vásquez[1,2], Luis Morales de la Vega[1], Luz Irene Pascual-Mathey*[1,2],

[1]*Facultad de Química Farmacéutica Biológica, Universidad Veracruzana, Xalapa, 91000, Veracruz, México*

[2]*Maestría en Farmacia Clínica, Universidad Veracruzana, Xalapa, 91000, Veracruz, México*

[3]*Centro de Alta Especialidad "Dr. Rafael Lucio", Xalapa, 91020, Veracruz, México*

ARTICLE INFO

Article history:
Received: 20 November, 2024
Revised: 18 December, 2024
Accepted: 19 December, 2024
Online: 19 January, 2025

Keywords:
Omeprazole
Stability
Extemporaneous preparation

ABSTRACT

Extemporaneous omeprazole-based preparations are commonly used in hospitals; however, there are no validated studies about physicochemical stability. This study aimed to determine if temperature, luminosity, and the type of diluent affect the stability of omeprazole in the extemporaneous preparation. For stability, the methodology validated previously by our group was used. The 2k experimental design included Temperature (25ºC and 35ºC) and Luminosity (covered by light and 400 Lx) variables. Diluents were evaluated at five levels: 1) Citric acid + polyethylene glycol solution, 2) Polyethylene glycol solution, 3) Physiological saline solution, 4) Citric acid + polyethylene glycol solution + physiological saline solution, and 5) Polyethylene glycol solution + physiological saline solution. Minitab 18 software was used for data analysis, and the degradation kinetics were determined by linear regression. The optimal condition for physicochemical stability was a temperature of 25ºC covered by light (OM1-3h 49', OM2-3h 2', SSF-5h 8', OM1SSF-2h 27', OM2SSF-6h 23'). The diluent based on physiological saline solution provided more than five hours of shelf-life, and more than six hours, the diluent based on OM2 + SSF. However, the best option is physiological saline solution, considering the accessibility of the diluent. In conclusion, environmental conditions should be considered in extemporaneous omeprazole-based preparation since they are affected by temperature, luminosity, and type of diluent. Assessing shelf-life prior to administration is necessary to provide a safe and effective drug, avoiding the occurrence of side effects in patients.

1. Introduction

Omeprazole (OMZ) is one of the most widely used drugs in hospitals, increasing its use every year. However, the indiscriminate use of extemporaneous omeprazole-based preparations represents a health risk. Up to 73% of patients who receive omeprazole do not require it, and 38% of these have shown adverse effects, which can prolong their hospital stay [1], [2].

The requirements for evaluating stability are indicated in the NOM-073 "Stability of drugs and medicines, as well as herbal remedies" for determining the shelf-life of medicines as marketed by the pharmaceutical industry [3]. However, in the case of extemporaneous drugs, there is no national regulation; the shelf-life should be determined by the conditions in which the extemporaneous preparation is made. Proper preservation is a prerequisite to maintaining the pharmacological and therapeutic properties. Therefore, it is important to improve safety since it can decrease effectiveness and modify safety due to the toxicity of degradation products [4].

Moreover, information on the stability and storage conditions of extemporaneous preparations is limited since pharmacovigilance is not a common practice in our country. In addition, generally, the unit in charge of performing such activity

*Corresponding Author: Luz Irene Pascual Mathey, Facultad de Química Farmacéutica Biológica, Universidad Veracruzana, Xalapa, C.P. 91000, Veracruz, México, +522281251392, lupascual@uv.mx

https://dx.doi.org/10.25046/aj100102

is the nursing. This can lead to errors, such as inadequate formulation, microbial contamination, concentration, and wrong dose calculation. Therefore, it is essential to evaluate the stability of the drug prior to its administration to patients to avoid the risk of adverse effects or toxicity [5].

The main conditions to retain the physicochemical stability and the microbiological properties within the quality specifications established in the formulation during its shelf-life and throughout storage time, are temperature, humidity, luminosity, and type of diluent [4], [6], [7]. Such variables can accelerate the degradation kinetics of active ingredients and alter their efficacy and safety [2], [3].

The shelf-life of a drug is measured by the concentration of the active ingredient, which should be < 10% of the total dose indicated on the product label. A percentage greater than 10% pointed out that the drug is losing effectiveness. Also, the degradation products could cause adverse or toxic effects on the patients [3], [5], [8], [9], [10], [11].

The 2k design systematizes and reduces the variables to simplify the procedure and evaluates the main effects and their interactions [12]. In 2k factorial designs, the 2 represents the two levels at which each variable is tested, identified as low (-) and high (+). The k represents each of the independent variables. The design (2*2) performs four different experiments; the variables are identified with the letters A and B, and the interaction between these two variables is identified with AB [13], [14].

Additionally, photosensitive drugs need to be kept covered by light due to their characteristics [11]. Those indications are usually mentioned in the package insert or technical data sheet. All photosensitive drugs should be kept in appropriate containers (protected from light) to avoid deterioration, both in the pharmaceutical services and the hospitalization units. Many of them are packaged by the pharmaceutical industry (in topaz glass ampoules) to protect them from light. If this does not occur, they should always be kept in the original package or wrapped in aluminum foil or other opaque paper [11].

In the internal medicine area of a tertiary care hospital in the state of Veracruz, a medication preparation service has been available since 2014, which has allowed a decrease in the adverse effects associated with medication (dosage, preparation, among others). However, there are no stability studies on extemporaneous preparations. Therefore, this study aimed to determine whether the factors of temperature, luminosity, and type of diluent are associated with the stability of omeprazole in extemporaneous preparations.

2. Methods

An experimental study was carried out in the Pharmaceutical Technology Laboratory of the School of Pharmaceutical Biological Chemistry, Universidad Veracruzana, Mexico.

The experimental steps carried out in this study are described in Figure 1.

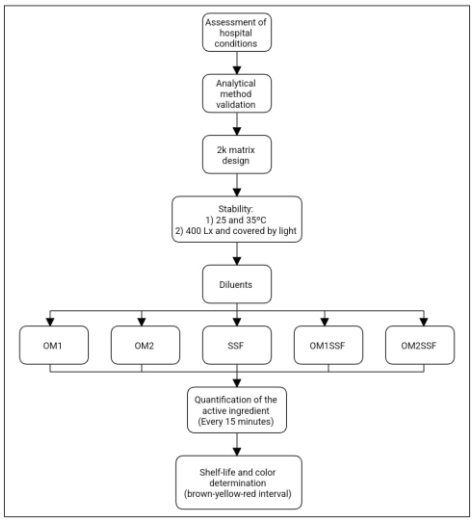

Figure 1: The flowchart summarizes the experimental design used in this study

2.1. Reagents:

The hospital provided two intravenous omeprazole trademarks (OMZ1 lot T18J487 and OMZ2 lot OM18I15). The OMZ reference standard was purchased from Sigma-Aldrich, purity 99.6%, lot LRAC0716, with the supplier's certificate of analysis.

2.2. Analytical equipment:

- UV Spectrophotometer, Beckman, model DU-7000.

- Stove, RIOS Rocha, model HS-33 adapted with 400Lx LED lamp.

2.3. Matrix of 2^k desing:

In this study a factorial design was used, since in each trial or complete replication of the experiment all possible combinations of factor levels were investigated [15]. Factorial designs produce more adequate experiments, since each observation provides information on all factors. Thus, the response to any factor observed under different conditions indicates whether the factors act independently on the experimental units. Interaction between factors occurs when their action is not independent [16].

The independent variables evaluated were Temperature, Luminosity, and Type of diluent. The dependent variable was the shelf-life. We performed a 2^k design to determine the association of factors involved in the stability of the active agent [13], [14]. Analyses were repeated ten times until the concentration of the active in the extemporaneous preparation decreased by more than 10 percent. Temperature includes 25 and 35 degrees Celsius (ºC). Luminosity includes covered by light and 400 Luxes (Lx). The diluent was evaluated at five levels, described in the next section. The variables and their levels are shown in Table 1.

The conditions used in this study were according to standards. The temperature of 25ºC is the optimal for the preparation and storage of non-thermolabile drugs. The second temperature was selected after reviewing the areas of administration of the extemporaneous preparations, with the maximum temperature at

35ºC. Concerning the luminosity, 400 Lx is what a standard hospital lamp provides.

Table 1. Factors and levels included in the 2^k desing.

Factors	Levels	
	Low (-)	High (+)
Temperature	25ºC	35ºC
Luminosity	Covered by light	400 Lx

Lx= luxes.

The proposed design (2^k) defines a total of 4 tests for each evaluation. The combinations used in each test are presented in Table 2.

Table 2. Matrix of 2^k desing

Test	Temperature	Luminosity
1	(-) 25ºC	(-) Covered by light
2	(+) 35ºC	(-) Covered by light
3	(-) 25ºC	(+) 400 Lx
4	(+) 35ºC	(+) 400 Lx

Lx= luxes.

For each diluent, a four-test assay matrix was assigned. The diluent preparation is shown below:

Diluents:

-SSF: Intravenous OMZ diluted with Physiological Saline Solution 0.9%.

-OM1: Intravenous OMZ diluted with its diluent (Solution with Citric Acid + Polyethylene Glycol).

-OM2: Intravenous OMZ diluted with its diluent (Polyethylene glycol solution).

-OM1SSF: Intravenous OMZ diluted with OM1 + SSF (50:50).

-OM2SSF: Intravenous OMZ diluted with OM2 + SSF (50:50).

SSF, OM1, and OM2 are commercial diluents that the hospital provides and used in the internal medicine area. The manufacturers did not indicate the OM1 and OM2 diluent concentrations. A matrix of two hundred determinations was performed considering the design matrix (4 tests), the diluents (5), and the ten sampling times.

Quantification method (Validation and quantification):

The OMZ quantification was previously reported and validated by our working group [17].

Stability:

Physicochemical stability (quantification of OMZ) was performed at the conditions of 25°C ± 2°C and 35°C ± 2°C, with a lamp providing 400 Lx. Samples prepared with the diluents were analyzed each 15 min until the concentration of OMZ decreased > 10% [3].

Color determination

The method was obtained from the analysis 0181 "Solution color" described in the United Mexican States Pharmacopoeia (2014). It is based on the visual color of the sample (in solution) against reference standards in a specific color range under established conditions [18].

The color presented in the sample, will be within the brown-yellow-red interval. A solution is considered colorless if its appearance is the same as that of the water or solvent used to reconstitute it (not more intense than the reference solution B9)

Preparation of standard solutions:

Solutions were prepared as indicated in Annex II of the FEUM "Preparation of reference solutions."

Procedure:

We prepared reference solutions in 10 mL tubes of equal diameters. Then, we transfer 5 mL of the sample of omeprazole preparation to a 10 mL test tube of equal diameter to those of the reference solutions. Compare the sample with the reference solutions in a horizontal plane separated from each other by 3 cm on a white background with indirect light.

3. Results and discussion

Shelf-life

The results of the stability of the drug OMZ in its different extemporaneous preparations are shown in Table 3 and Figure 2, where the shelf-life times (time in hours to reach 10% degradation of the active principle) are presented.

Regarding shelf-life, the optimal condition is covered by light at 25°C (Test 1). According to the literature, this condition prevents the degradation of the active ingredients [19], [20].

The diluents with the best shelf-life times (obtained in all the conditions evaluated) were SSF and OM2SSF (Table 3 and Figure 2).

Table 3. Shelf-life times (hours).

Tests	Diluents				
	OM1	OM2	SSF	OM1SSF	OM2SSF
1	3h 49'	3h 2'	5h 8'	2h 27'	6h 23'
2	01h 4'	01h 16'	02h 25'	01h 10'	01h 22'
3	01h 57'	01h 57'	01h 48'	01h 48'	02h 20'
4	01h 4'	01h 15'	02h 19'	02h 00'	01h 6'

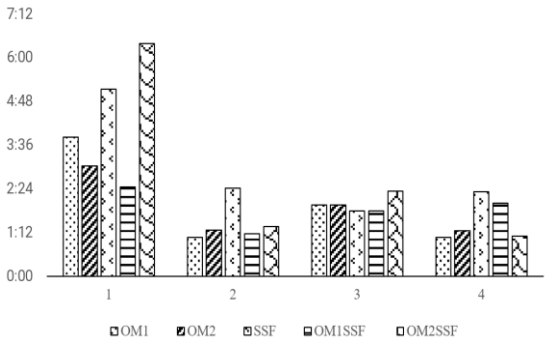

Figure 2. The graph shows the shelf-life of the different conditions (Tests identified from 1 - 4, see Table 2) and the diluents evaluated.

The above results differ from those reported in the Stabilis 4.0 page, which indicates shelf-life times of 6 hours with 5% glucose solution covered by light, without considering the temperature. The values closest to those previously reported are those obtained

for preparations with OM2SSF diluent (06h 23), followed by the preparation with SSF diluent (05h 08) of shelf-life, both at conditions of 25°C and covered by light. The literature indicates that preparations with the SSF-based diluent presents a shelf-life of 12 hours. However, the present study shows lower shelf-life times than previously reported. Those results allow us to point out that it is necessary to verify the shelf-life times reported in the literature and check the operating conditions of each institution center.

In the tertiary hospital where extemporaneous preparations of OMZ are prepared, the shelf-life used is four hours, according to the information indicated in the inserts (at room temperature <no more than 30°C> covered by light).

Concerning the results obtained in this study, the stability conditions recommended by the manufacturers in the insert were not met. For OM1 (diluent with citric acid and polyethylene glycol), under the conditions of 25°C and covered by light, a shelf-life of 03h 49 hours was obtained. For the OM2 solution (diluent with polyethylene glycol), a shelf-life of 03h 02 hours was obtained. On the other hand, the conditions of 35°C and 400 Lx (OM1 and OM2) showed a shelf-life above two hours for both solutions without completing the shelf-life mentioned in the insert.

Figure 3 shows the predictions obtained using the Arrhenius method for the 30°C condition of the diluents of solutions OM1 and OM2, where the comparison with the temperatures of 25°C (circle) and 35°C (triangle), both covered by light, can be seen. The red line on the Y axis indicates 90% of the active; the X axis indicates the time marked on the label of the two drugs (4 hours).

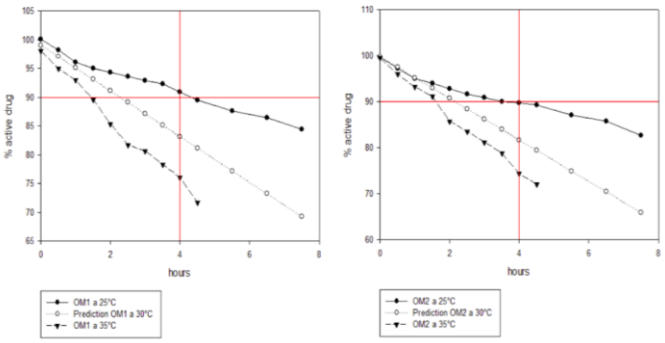

Figure 3. Predicted degradation of omeprazole at 30ºC (lines identified by white circles) compared to 25ºC (lines identified by black circles) and 35ºC (lines identified by triangles) with both diluents (OM1 and OM2). The intersection of the red lines determines the time of 4 hours concerning a concentration of 90% of the active ingredient.

Analysis of main effects (2^k design)

The original design proposed in this study is a 2^k, which considers the variables temperature and luminosity for each diluent analyzed. The results obtained for the main effects and interaction are reported below.

Regarding the analysis of the main effects (Figure 4), the impact of temperature on the shelf-life is more significant in the average variation of response compared to luminosity in the different tests with the diluents, except the SSF where the main effect is luminosity compared to temperature. The plots of the main effects corroborate the significance of each of the diluents tested.

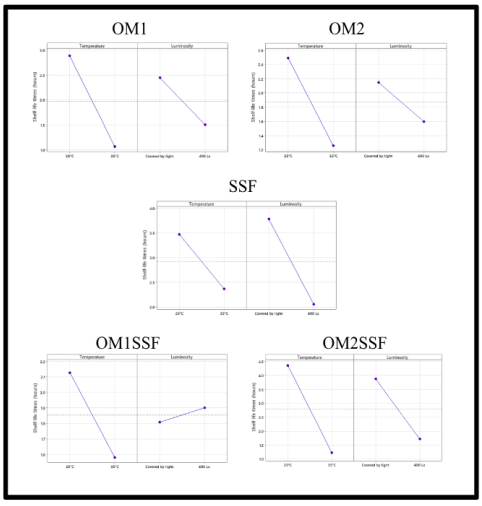

Figure 4: Plots of the main effects. Behavior of OMZ with temperature and luminosity factors in the different diluents.

Regarding the interaction effect, all the diluents present a possible interaction between temperature and luminosity. However, there is a complete interaction in the diluent OM1SSF, corroborated in the interaction graphs in Figure 5.

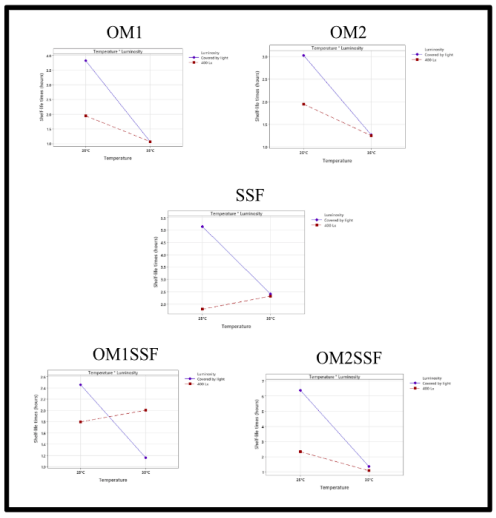

Figure 5. Interaction graphs. The behavior of OMZ concerning the interaction of temperature and humidity factors in the different diluents.

The SSF diluent is the best option for the extemporaneous preparation of OMZ, considering the luminosity, since it is the variable that most affects it. Those will provide better control of the preparation since it is easier to control the luminosity [11].

The diluent least affected by the main effects and by the interaction is the OM2SSF, presenting good shelf-life times. The difficulty of the preparation is the availability of the diluent polyethylene-glycol since its preparation is limited to the manufacturer's availability [7].

On the other hand, the diluent with the greatest variation was the OM1SSF, where temperature and luminosity decreased the shelf-life. This preparation presented the biggest interaction and the lowest shelf-life.

Solution color

Simultaneously to the quantification of the active ingredient, color determinations were made by comparison with standards. The results are presented in Figure 4.

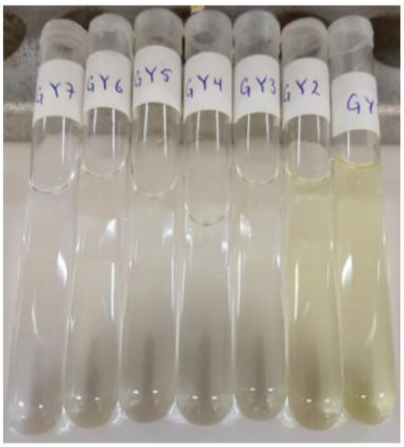

Figure 4. Color standards used for solution color testing. GY = color scale according to pharmacopoeia within the brown-yellow-red interval. GY1 represents the highest intensity.

Omeprazole is a photosensitive drug, so when exposed to light, it shows slight coloration, as evidenced in this test. Tables 4, 5, and 6 show the samples that presented coloration when exposed to 400 Lx. The coloration with the greater intensity was at 25ºC temperature. There were no visual differences between the diluents (OM1 versus OM2, and SSF versus OM2SSF) (Tables 4 and 5) except the OM1SSF mixture (Table 6), which exhibits a coloration that occurs at 25ºC with 400 Lx.

In this analysis, there is no direct relationship between the appearance of color in the preparation and the degradation of omeprazole. However, there is a direct relationship between the color appearance in the solution and the exposure to 400 Lx luminosity. These results suggested a decrease in the appearance of color in extemporaneous preparations of omeprazole intravenous solution.

One of the main limitations of this study is that stability studies could not be performed during storage time; however, the results indicate that pharmacovigilance studies applied to extemporaneous preparations are necessary to inform the nursing department about the correct conditioning of the extemporaneous preparation to provide a safe and effective drug, avoiding the occurrence of side effects in patients [5].

Table 4. Staining of the diluent solution OM1 and OM2.

	T0	T1	T2	T3	T4	T5	T6	T7	T8	T9
25°C – C/L	GY7	GY7	GY7	GY7	GY7	GY6	GY6	GY5	GY4	GY3
35°C – C/L	GY7	GY7	GY7	GY6	GY6	GY6	GY5	GY4	GY4	GY3
25°C – 400lx	GY7	GY7	GY6	GY6	GY4	GY3	GY3	GY2	GY2	GY2
35°C – 400lx	GY7	GY7	GY7	GY6	GY5	GY5	GY4	GY3	GY2	GY2

GY = color scale according to pharmacopoeia within the brown-yellow-red interval. GY1 represents the highest intensity. C/L = cover of light. No difference was observed between solutions OM1 and OM2.

Table 5. Staining of the diluent solution SSF and OM2SSF

	T0	T1	T2	T3	T4	T5	T6	T7	T8	T9
25°C – C/L	GY7	GY7	GY7	GY7	GY6	GY6	GY5	GY5	GY4	GY3
35°C – C/L	GY7	GY7	GY7	GY6	GY6	GY6	GY5	GY4	GY4	GY3
25°C – 400lx	GY7	GY7	GY6	GY6	GY4	GY3	GY3	GY2	GY2	GY2
35°C – 400lx	GY7	GY7	GY7	GY6	GY5	GY5	GY4	GY3	GY2	GY2

GY = color scale according to pharmacopoeia within the brown-yellow-red interval. GY1 represents the highest intensity. C/L = cover of light. No difference was observed between solutions SSF and OM2SSF.

Table 6. Staining of the diluent solution OM1SSF

	T0	T1	T2	T3	T4	T5	T6	T7	T8	T9
25°C – C/L	GY7	GY7	GY7	GY7	GY6	GY6	GY5	GY4	GY3	GY3
35°C – C/L	GY7	GY7	GY7	GY6	GY6	GY5	GY4	GY4	GY3	GY3
25°C – 400lx	GY7	GY6	GY6	GY6	GY3	GY3	GY2	GY2	GY2	GY2
35°C – 400lx	GY7	GY7	GY7	GY6	GY5	GY4	GY4	GY3	GY2	GY2

GY = color scale according to pharmacopoeia within the brown-yellow-red interval. GY1 represents the highest intensity. C/L = cover of light.

4. Conclusion

The stability of the extemporaneous preparation of OMZ - intravenous solution is affected by temperature, luminosity, and type of diluent. Temperature was the variable with the main impact on shelf-life, with the shelf-life at 25°C except for the SSF solution, whose effect was mainly due to luminosity. Regarding luminosity, the optimal condition is preparing extemporaneous solutions covered by light. The optimal diluent for the extemporaneous preparation of OMZ is based on a physiological saline solution due to its longer shelf-life and no commercial brand limitations for its preparation. Concerning the staining of solutions, it is necessary to protect Omeprazole preparations from light, regardless of the diluent used, to ensure the effectiveness and safety of the drug. These conditions are necessary for the good management of omeprazole in the hospital setting, for its suitability for clinical use, and to avoid ineffectiveness and toxic effects associated with its irrational use.

Conflict of Interest

The authors declare no conflict of interest.

Acknowledgment

The authors thank the Centro de Alta Especialidad “Dr. Rafael Lucio” for the support of this work.

References

[1] F. Carranza, “Seguridad del omeprazol: ¿es adecuada la duración de los tratamientos?” Farmacéuticos Comunitarios, **7(1)**: 5–9, 2015, DOI: https://doi.org/10.5672/fc.2173-9218.(2015/vol7).001.02.

[2] Castro, C. M. De Argila, A. Albillos, “Consideraciones prácticas en el manejo de los inhibidores de la bomba de protones,” Revista Española de Enfermedades Digestivas (Madrid), **108**: 145–153, 2016, http://scielo.isciii.es/pdf/diges/v108n3/es_revision.pdf.

[3] Secretaría de Salud, "NOM-073-SSA1-2005, Estabilidad de fármacos y medicamentos," **2005**, https://salud.gob.mx/unidades/cdi/nom/073ssa105.html.

[4] J. R. Falconer, K. J. Steadman, "Extemporaneously compounded medicines," Australian Prescriber, **40(1)**: 5–8, 2017, DOI: https://doi.org/10.18773/austprescr.2017.001.

[5] M. R. Mattos da Silva, D. L. Pereira, E. P. dos Santos, J. E. Ricci, "Preparation of extemporaneous oral liquid in the hospital pharmacy," Brazilian Journal of Pharmaceutical Sciences, **56**: e18358, 2020, DOI: https://doi.org/10.1590/s2175-97902019000418358.

[6] V. K. Yellepeddi, "Stability of extemporaneously prepared preservative-free prochlorperazine nasal spray," American Journal of Health-System Pharmacy, **75(1)**: e28–e35, 2018, DOI: https://doi.org/10.2146/ajhp160531.

[7] N. Barrueco, I. Escobar-Rodríguez, B. García-Díaz, M. E. Gil-Alegre, E. López-Lunar, M. G. Ventura Valares, "Estabilidad de medicamentos en la práctica clínica: de la seguridad a la eficiencia," Farmacia Hospitalaria, **37(3)**: 175–177, 2013, DOI: https://dx.doi.org/10.7399/FH.2013.37.3.587.

[8] M. Yu, J. Qian, D. Guo, L. Li, X. Liu, "Severe adverse reactions caused by omeprazole: A case report," Experimental and Therapeutic Medicine, **12(2)**: 1103–1106, 2016, DOI: https://doi.org/10.3892/etm.2016.344V.

[9] FEUM, "Suplemento para establecimientos dedicados a la venta y suministro de medicamentos y demás insumos para la salud," **6a. Edición**, 2019, México.

[10] E. Casaus, "Guía de buenas prácticas en la administración de medicamentos en servicios de farmacia hospitalaria," Farmacia Hospitalaria, **2024**, https://www.sefh.es/sefhpdfs/GuiaBPP_JUNIO_2014_VF.pdf.

[11] I. Sánchez, M. D. Nájera, A. Espuny, J. C. Titos, "Revisión de la estabilidad de los medicamentos fotosensibles," Farmacia Hospitalaria, **35(4)**: 204–215, 2011, DOI: https://doi.org/10.1016/j.farma.2010.05.005.

[12] A. Correa, P. Grima, X. Tort-Martorell, "Experimentation order with good properties for 2k factorial designs," Journal of Applied Statistics, **36(7)**: 743–754, 2009, DOI: https://doi.org/10.1080/02664760802499337.

[13] J. Lu, "On finite-population Bayesian inferences for 2k factorial designs with binary outcomes," Journal of Statistical Computation and Simulation, **89(5)**: 927–945, 2019, DOI: https://doi.org/10.1080/00949655.2019.1574793.

[14] P. Paengkoum, C. Yuangklang, S. Paengkoum, "Robust 2k factorial designs: non-normal symmetric distributions," Pakistan Journal of Statistics, **77(2555)**: 73–77, 2012, https://avesis.anadolu.edu.tr/yayin/5e5440d7-fa53-4f62-b152-d7f40e35d981/robust-2k-factorial-designs-non-normal-symmetric-distributions.

[15] D. Montgomery, "Diseño y análisis de experimentos," **2a. Edición**, Limusa Wiley, **2010**, México.

[16] L. Kuehl, "Diseño de Experimentos: Principios estadísticos para el diseño y análisis de investigaciones," **2a. Edición**, Thomson Learning, **2001**, España.

[17] E. Cruz, I. Camacho, J. Locia, L. I. Pascual, M. O. Pérez, J. J. Diaz, "Validation of a UV spectrophotometric method for quantification of Omeprazole using different types of diluents," IEEE International Conference on Engineering Veracruz (ICEV), **2023**, DOI: 10.1109/ICEV59168.2023.10329709.

[18] FEUM, "Métodos generales de análisis," **11a. Edición**, **2014**, México.

[19] Secretaría de Salud, "NORMA Oficial Mexicana NOM-249-SSA1-2010, Mezclas estériles: nutricionales y medicamentosas, e instalaciones para su preparación," **2010**, http://www.dof.gob.mx/normasOficiales/4327/salud/salud.htm.

[20] A. Tellez, "Modelo nacional de farmacia hospitalaria," Secretaría de Salud, **2009**, https://www.uaeh.edu.mx/investigacion/icsa/LI_UsoMedic/Ana_Tellez/modelo.pdf.

ASTES

Advances in Science, Technology and Engineering Systems Journal Vol. 10, No. 1, 13-19 (2025)

www.astesj.com

Special Issue on AI-empowered Smart Grid Technologies and EVs 2024

ASTESJ

ISSN: 2415-6698

Impact of Integrating Chatbots into Digital Universities Platforms on the Interactions between the Learner and the Educational Content

Khalifa Sylla [1,*], Birahim Babou [2], Mama Amar [1], Samuel Ouya [3]

[1] *Science, Technology and Digital Center, Cheikh Hamidou Kane Digital University (ex UVS) of Senegal, 15126 Dakar-Fann, Senegal*

[2] *Infrastructure and Information Systems Department, UNCHK of Senegal, 15126 Dakar-Fann, Senegal*

[3] *LITA Laboratory, Polytechnic High School, Cheikh Anta Diop University of Senegal, 5085 Dakar-Fann, Senegal*

ARTICLE INFO

Article history:
Received: 01 November, 2024
Revised: 06 January, 2025
Accepted: 07 January, 2025
Online: 20 January, 2025

Keywords:
Artificial Intelligence
Chatbot
Moodle
Machine Learning
Rasa

ABSTRACT

The rapid expansion of digital universities across Africa addresses the need for scalable higher education solutions, but challenges such as limited physical infrastructure and high dropout rates persist. In digital learning environments, effective interaction with educational content is crucial for student success. This article explores the transformative role of chatbots integrated into digital university platforms, with a specific focus on their impact on learner-content interactions. Leveraging the frequent use of messaging applications and advances in Artificial Intelligence (AI), we examine how chatbot integration enhances student engagement, facilitates personalized access to core educational modules, and supports formative assessments to reinforce learning outcomes. Using the Rasa open-source framework and the Moodle Learning Management System (LMS), we present a model that not only delivers content efficiently but also provides an interactive learning experience through AI-driven dialogue systems. Furthermore, a comparison of the different AI tools used for educational chatbots will be presented, to determine the most suitable solutions for digital teaching. This analysis will consider various aspects such as efficiency, customization, flexibility and ease of integration of the tools into educational environments. This study highlights how chatbots can foster a more dynamic and responsive learning ecosystem, ultimately improving student retention and mastery of key concepts in digital universities. In this article, we explore the broader impact of chatbots on learner interaction with educational content, not just their integration. It also emphasizes student engagement and retention.

1. Introduction

In recent years, digital universities have emerged across several African countries as a response to the growing demand for higher education. To address the challenges of massification and limited physical infrastructure, various digital universities [1], [2], [3] have introduced innovative pedagogical models, often relying on open digital spaces (ODS) to complement virtual environments. These ODS provide students with collaborative spaces to address pedagogical, technical, administrative, and social issues [4].

Students in digital universities primarily rely on distance learning platforms to access their educational materials. However, challenges related to the user experience and accessibility of certain Learning Management Systems (LMS) have contributed to increased dropout rates. To address these issues and improve access to educational content, universities have implemented various solutions, such as integrating social media and providing pedagogical support through tutors.

To further enhance the interaction between students and educational content, this paper proposes the integration of a chatbot into digital university platforms. By offering an intuitive and responsive interface, the chatbot aims to streamline content access and improve the overall learning experience. A chatbot is an advanced tool for automated, context-aware communication

* Corresponding Author: Khalifa SYLLA, Cheikh Hamidou Kane Digital University (ex UVS) of Senegal, khalifa.sylla@unchk.edu.sn

https://dx.doi.org/10.25046/aj100103

between users and systems, utilizing natural language processing for a conversational approach [5].

The remainder of this article is structured as follows: first, we will examine the related work in this area, followed by an overview of fundamental chatbot concepts. Next, we will discuss the design and implementation of our proposed solution, concluding with insights for future development.

2. The State of the Art

Artificial intelligence has left no stone unturned. Several researchers specializing in the field have carried out studies on the impact of AI in the education sector, and in digital universities.

Such is the case of authors of [5] who, in their article, propose the integration of conversational chatbots for educational remediation within the framework of covid-19. Among other things, the chatbot enables learners to self-train on parts of the course they haven't quite mastered.

It is connected to a Moodle platform, enabling learners to continue their learning at a distance. The chatbot is integrated as a Moodle plugin and can be used on other LMSs.

Researchers in [6], who propose and describe a new recommendation approach based primarily on the use of a chatbot linked to the Moodle platform.

The authors in [7], have proposed an intelligent agent in the form of a chatbot on the IBM Bluemix platform. This agent automates interaction between users and the Moodle training platform. This is a very interesting proposal, but it is specific to a technology belonging to IBM.

In [8], the authors set up a chatbot for a mobile application enabling interaction between users and a Moodle LMS platform. This tool is used on a specific LINE Chat application and meets a need of the Japanese community.

In [9], the authors have proposed a methodology to improve the quality of e-learning, chatbot architectural design, to help learners self-regulate their learning by accompanying them via a chatbot within the Moodle platform, which constitutes a metacognitive virtual assistant.

In [10], the authors with their chatbot in place, have enabled their institution's administration to reduce the amount of work they have to do to provide the required information to students, thus reducing their workload by continuing to answer all student questions. They also confirm that chatbot systems can be used in a wide range of sectors, including education, healthcare and marketing.

In [11] the authors conducted a comprehensive survey of recent deep learning techniques for chatbots, enhancing developers' understanding of effective chatbot design. In [12], the authors illustrates the design and development of illustrate at bot software, which integrates with a user website to manage student queries through defined intents. The article discusses the chatbot system utilizing a Recurrent Neural Network (RNN) for language processing, a Convolutional Neural Network (CNN) for image handling, and Dialogflow for intention and entity representation, along with keyword matching techniques. In [13], the authors have created three chatbots to support teaching in their university's Department of Electronics and Multimedia Telecommunications. The first, KEMTbot, is available on the department's website, providing information from the web and about the staff. The second chatbot assists students during exercises in the "Databases" course, while the third is an Amazon Alexa skill that responds to questions regarding the department on Amazon Echo devices.

3. Presentation of Artificial Intelligence (AI) tools used for educational chatbots

Natural language understanding (NLU) platforms are at the core of all chatbots. Conducting a comparative analysis of tools like Rasa, IBM Watson, Dialogflow, and TensorFlow is crucial to assess their strengths, weaknesses, and suitability for educational platforms such as Moodle.

3.1. Rasa

Rasa [14] is an open-source software that includes two main modules: Rasa NLU and Rasa Core. Rasa NLU focuses on natural language understanding, while Rasa Core handles dialogue management. The goal, according to its creators, is to bridge the gap between research and real-world applications, bringing recent advancements in machine learning to a wider audience, including those with limited experience who want to develop conversational agents.

3.2. Dialogflow

Dialogflow [15] is a natural language processing (NLP) platform developed by Google that enables the creation of chatbots and virtual assistants capable of understanding and responding to user interactions in natural language.

3.3. TensorFlow

TensorFlow is an open-source platform developed by Google, designed for machine learning and artificial intelligence applications. It provides a comprehensive library and flexible ecosystem of tools that allow developers to build and deploy machine learning models efficiently. TensorFlow is widely used for tasks such as natural language processing, image recognition, and deep learning, making it an essential tool for developing sophisticated AI applications, including chatbots [16].

Its scalability makes it a popular choice for integrating intelligent capabilities into digital learning platforms.

3.4. IBM Watson

IBM Watson [17] is notable for its robustness and capacity to handle vast amounts of data. It offers predefined templates tailored to various sectors, such as banking, and includes a visual dialog editor, making it accessible for non-programmers to create conversation flows easily. In [18], the authors analyze this platform alongside others in terms of functionality and usability.

To summarize, this description of AI tools used in educational chatbots will offer a technical reference guide to help select the most suitable solutions for the needs of digital universities, while also delving into the technical aspects of integrating chatbots into learning systems like Moodle.

4. Basic Concepts and Tools Used

To provide a foundation for understanding the integration of chatbots in digital learning environments, this section will cover the fundamental concepts and tools essential for developing and deploying chatbot solutions in educational contexts.

4.1. Chatbots

The first Chatbot, ELIZA, was developed by Joseph Weizenbaum at the Massachusetts Institute of Technology (MIT) in 1966. Researchers define chatbots in various ways, including terms such as conversational AI entities, virtual assistants, chatterbots, digital assistants, and chatbots. Regardless of terminology, the primary goal of a chatbot remains to simulate human conversation. [19], [20], [21].

Advancements in Artificial Intelligence (AI) and Machine Learning (ML) have positioned conversational agents as essential tools across various industries. Many organizations adopt these solutions to both reduce physical staffing needs and enable rapid, automated responses based on predefined implementation criteria [22].

A conversational agent, also known as a chatbot or dialogue system, interacts with users in natural language, enabling it to understand and respond in a way that resembles human conversation. These systems can operate through text or voice-based interactions [23].

Conversational agents are widely applied in fields such as human resources, healthcare, and education, showcasing their versatility and impact across diverse sectors [24], [25].

4.2. Moodle

Moodle (Modular Object-Oriented Dynamic Learning Environment) is a free Learning Management System distributed under the GNU General Public License. It is developed in PHP. In addition to the possibility of creating courses with integrated tools and categorizing content by course, cohort level, sub-category, etc., the platform offers the possibility of being interconnected with external tools via secure APIs.

4.3. Interoperability between the chatbot and the Moodle platform using API

An API (Application Programming Interface) is a tool enabling different systems to communicate with each other. It defines the methods by which the two systems can communicate.

Moodle offers several APIs for interaction between the chatbot and its system. To retrieve data from the Moodle platform, authentication is required via a time-limited Token. To enable the chatbot to access the APIs, an authentication function must be implemented [26].

4.4. Natural Language Processing (NLP)

NLP (Natural Language Processing) is a branch of computer science focused on developing systems that enable computers to communicate with people using everyday language [27].

The intelligent conversation system is the foundation on which all Chatbots are built. It enables us to understand user requests and respond in a relevant way. This type of system is often built on top of an understanding and categorization algorithm. Let's now focus on the different elements of language processing: NLG (Natural Language Generation) and NLU (Natural Language Understanding).

Most chatbots operate on a basic model of these three properties, namely: Entities, Intentions, Response.

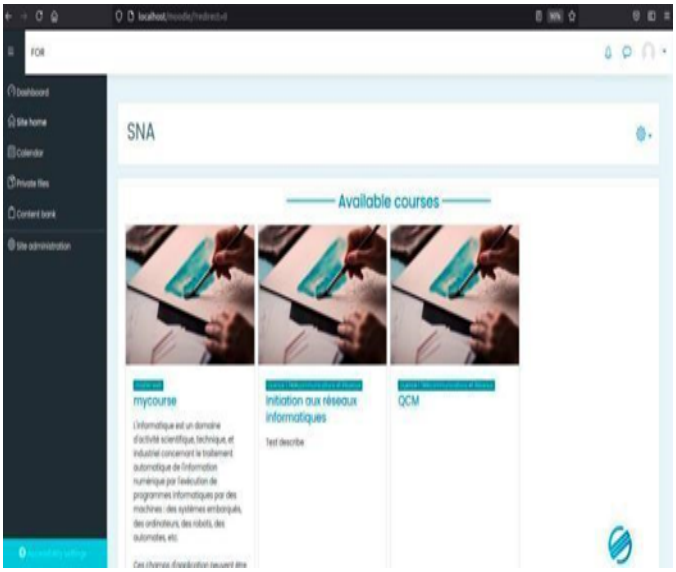

Figure 1: Moodle Platform Homepage

4.5. Key stages in the learning process

The first part consists of creating the NLU and discussion models, commonly known as the training phase. As Rasa is based on Machine Learning, it requires training data.

- For the NLU part (Rasa-NLU), the training data are sample sentences that the user might utter, in which intent and entities are specified. A configuration file is also required to set the algorithm parameters.
- For the discussion part (Rasa-CORE), a set of stories must be defined so that the agent learns to choose its next action. The configuration file accompanying the stories contains lists of intentions, entities, slots and actions.

4.6. Advantages of integrating chatbot into the learning system

An API (Application Programming Interface) is a tool enabling different systems to communicate with each other. It defines the methods by which the two systems can communicate.

Moodle offers several APIs for interaction between the chatbot and its system. To retrieve data from the Moodle platform, authentication is required via a time-limited Token. To enable the chatbot to access the APIs, an authentication function must be implemented.

5. Solution Implementation and Results

The implementation of a conversational agent involves several stages, including preparation and selection of the solution,

development, and finally management and continuous improvement.

5.1. Chatbots

The first Chatbot, ELIZA, was developed by Joseph Weizenbaum at the Massachusetts Institute of Technology (MIT) in 1966. Researchers define chatbots in various ways, including terms such as conversational AI entities, virtual assistants, chatterbots, digital assistants, and chatbots. Regardless of terminology, the primary goal of a chatbot remains to simulate human conversation.

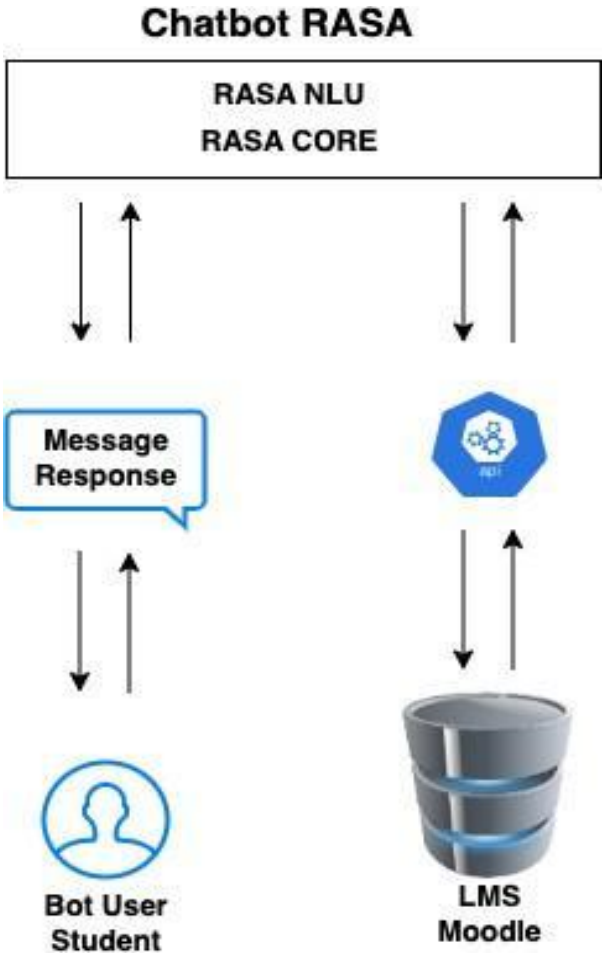

Figure 2: System architecture

5.2. Solution Development

There are several stages in the development of the solution:

- Step 1: Installing Rasa
- Step 2: Project creation
- Step 3: Defining intentions and examples
- Step 4: Defining responses
- Step 5: Creation of dialogue stories
- Step 6: Model training and testing
- Step 7: Creating the graphical interface

Once the prerequisites have been set up, the next step is to train the model and test it in console mode.

Below are additional features that we have implemented to predict the learning outcome and to personalize the learning path.

```
$ch = curl_init();

    curl_setopt($ch, CURLOPT_URL, 'http://localhost/moodle/login/token.php?username=' $frm->username '&password=' $frm->password '
        &service=moodle_mobile_app');
    curl_setopt($ch, CURLOPT_RETURNTRANSFER, 1);

    $result = curl_exec($ch);

    $json_res = json_decode($result, true);

setcookie("user", $json_res['token'], time() + (86400), "/"); // 86400 = 1 day
    if (curl_errno($ch)) {
        echo 'Error:' . curl_error($ch);
    }
    curl_close($ch);
```

Figure 3: Moodle authentication and token recovery function

- **Learning Outcomes Prediction**

The objective is to leverage predictive analytics to forecast student performance based on their interactions with the chatbot. The predictive analytics model will use below data sets:

Data Collection:

- Interaction Logs: Collect detailed logs of student interactions with the chatbot, including questions asked, resources accessed, and response times.
- Performance Metrics: Gather data on student performance in assignments, quizzes, and exams.
- Behavioral Data: Track engagement metrics such as login frequency, time spent on different types of content, and participation in discussions.

Predictive models:

We use regression models to predict grades or performance scores based on interaction data. The grades and performance will then be used by a neural networks model to categorize students into different performance levels (e.g., at risk, average, high performer). Finally, we applied time series analysis to monitor and predict changes in student performance over time.

Model Evaluation:

Cross-validation techniques are used to assess the accuracy and robustness of the predictive models. Precision and F1-Score are used to evaluate the models.

- **Personalized Learning Paths**

The objective of this feature is to create algorithms that adapt educational content and recommendations based on the student's progress and learning style.

Presentation of the algorithms:

- **Content Recommendation:** Develop recommendation algorithms that suggest tailored content based on the student's learning style and knowledge level.
- **Progress Tracking:** Implement systems to continuously monitor student progress and adjust learning paths dynamically.
- **User Feedback:** Collect feedback from students on the

usefulness and relevance of recommended content to refine the algorithms.

After configuration and testing, it's important to set up a graphical interface enabling users to interact with the system. This interface defines the access parameters for the Rasa chatbot.

After finalizing the creation of the chatbot in console mode, we created the graphical interface enabling us to interact more easily with the chatbot.

```
<body onload="checkCookie()">

  <div class="chat-container"></div>
  <div class="profile_div" id="profile_div">
    <img class="imgProfile" src="static/img/botAvatar.png">
  </div>
  <script src="Chatroome.js"/></script>
  <script type="text/javascript">
    botimg = document.querySelector(".profile_div");
    var show = true;
  botimg.addEventListener("click", function(){

    var chatroom = new window.Chatroom({
      host: "http://localhost:5005",
      title: "SNA ChatBot ",
      container: document.querySelector(".chat-container"),
      welcomeMessage: "Bienvenue sur le chatbot de SNA",
      speechRecognition: "en-FR",
      voiceLang: "en-FR"
    });
    chatroom.openChat();
    botimg.style.display = "none";

   if(show){
    divchat = document.querySelector(".chats");
    var node = document.createElement("img");
    node.src="https://i.postimg.cc/7hFwJtZZ/Logo-en-bleu.png";
    node.style.textAlign = "center";
    node.style.display="block";
    node.style.marginLeft="auto";
    node.style.marginRight="auto";
    node.style.width="80%";
    divchat.insertBefore(node, divchat.firstChild);
    show = false;
   }
```

Figure 4: Code of Chatbot graphical interface

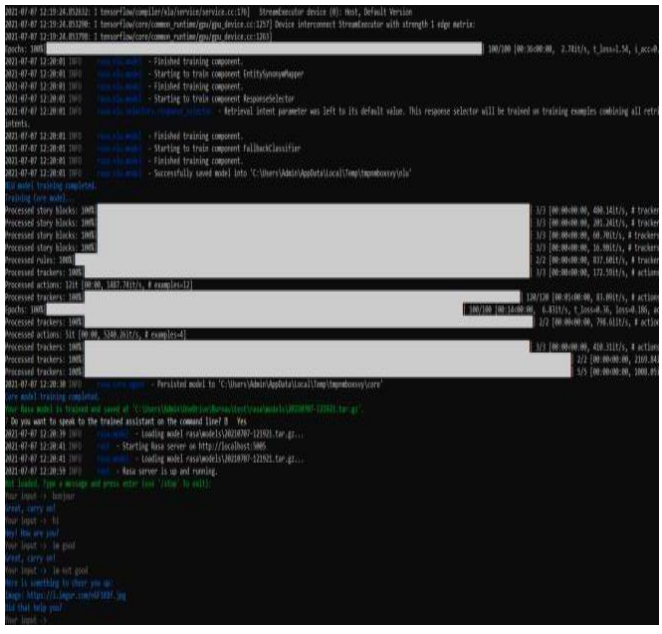

Figure 5: Model training

5.3. Steering and Continuous Improvement

Depending on the indicators set to measure the system's performance, it is important to measure the rate of understanding of the entities' performance, and to make continuous improvements by adding responses as the system is used.

5.4. Results of our studies

In this paper we have studied the impact of integrating chatbots on digital university platforms. The objective of our work was to demonstrate that the integration of chatbots into digital university platforms aims to improve the interaction between learners and educational content, while considering the specificities of distance learning. We designed and implemented a solution that allows us to validate our study.

The results of our studies show the following benefits:

First, the interactions between learners and educational content have increased significantly. This improvement is especially notable in areas such as forums activities and the facilitation of virtual classes, where the chatbot helps create a more engaging and supportive learning environment. Indeed, by providing real-time support and allowing automated responses to common questions, chatbots promote active discussions and encourages collaboration in the forums activities. The consequence of this is a reduction in dropout rates.

The other results were that we noticed the enhancement and diversification of digital content. By offering personalized content recommendations, providing interactive resources, chatbot adapts the learning experience to individual needs. This dynamic content support enhances the learning journey, making it more accessible for students.

Furthermore, the integration of the chatbot improves the assessment framework within the digital platform. By automating the formative quizzes and providing feedback, chatbots support learners in understanding and mastering core concepts, making assessments a more continuous and interactive part of the learning process.

6. Conclusion and Perspectives

To provide a foundation for understanding the integration of chatbots in digital learning environments, this section will cover the fundamental concepts and tools essential for developing and deploying chatbot solutions in educational contexts.

In this paper, we explored the integration of a chatbot into digital university platforms to enhance the interaction between learners and educational content. The chatbot, powered by Artificial Intelligence (AI), Machine Learning (ML), and built using the Rasa framework, was connected to the Moodle Learning Management System (LMS) to enable learners to self-train effectively, particularly in core IT modules. By leveraging natural language processing, this chatbot provides a seamless and intuitive way for students to access educational resources and engage with learning materials in a more dynamic and responsive manner.

As AI technology continues to evolve, our next step will be to extend the capabilities of this chatbot by integrating it with systems like ChatGPT. This will enable learners, including those outside of the Moodle platform, to ask questions and receive personalized support across various fields of study. By doing so, we aim to create a more comprehensive and accessible tool that can serve a

broader range of students, making the chatbot an invaluable resource for learners across different academic disciplines.

This work allowed us to explore how the integration of chatbots into digital university platforms can help reduce dropout rates, particularly in the most demanding courses or those where the failure rate is historically high. Indeed, considering the statistics of previous studies, the use of chatbots could impact student retention in programs, by comparing the rates before and after the integration of the chatbot.

In order to strengthen the results obtained, several avenues for improvement are planned:

Integration with advanced AI systems, such as ChatGPT, to allow an even more contextualized response to student questions on various subjects.

Improvement of the user interface to further facilitate access to educational content and modules.

Development of additional features for the continuous assessment of student performance via more sophisticated predictive models.

The integration of chatbots into digital universities transforms access to educational content and improves learner engagement. Through AI and adaptive systems, students benefit from a personalized, dynamic and enriching experience, which helps improve their academic success in digital environments.

Conflict of Interest

The authors declare no conflict of interest.

References

[1] K. Sylla, N. M. Ndiaye, S. Ouya and G. Mendy, "Towards the use of a contact center for the socialization and capacity reinforcement of learners of African digital universities," 2020 22nd International Conference on Advanced Communication Technology (ICACT), Phoenix Park, Korea (South), 2020, pp. 603-607, doi: 10.23919/ICACT48636.2020.9061548.

[2] HOLO, AMON KASSI, BI SEHI ANTOINE MIAN, and YADOHO NOEL COULIBALY. "L'encadrement des étudiants dans le dispositif formations ouvertes et à distance de l'Université Virtuelle de Côte d'Ivoire." Educational Journal of the University of Patras UNESCO

[3] B. Babou, K. Sylla, M. Y. Sow and S. Ouya, "Integration of a Chatbot to Facilitate Access to Educational Content in Digital Universities," 2024 26th International Conference on Advanced Communications Technology (ICACT), Pyeong Chang, Korea, Republic, 311-314, 2024, doi: 10.23919/ICACT60172.2024.10471975.

[4] Sylla, K., Nkwetchoua, G. M. M., & Bouchet, F., "How Does the Use of Open Digital Spaces Impact Students Success and Dropout in a Virtual University?". International Association for Development of the Information Society, 2022

[5] K. Gaglo, B. M. Degboe, G. M. Kossingou and S. Ouya, "Proposal of conversational chatbots for educational remediation in the context of covid-19," 2022 24th International Conference on Advanced Communication Technology (ICACT), PyeongChang Kwangwoon_Do, Korea, Republic, 354-358, 2022, doi: 10.23919/ICACT53585.2022.9728860.

[6] K. Souali, O. Rahmaoui, M. Ouzzif and I. El Haddioui, "Recommending Moodle Resources Using Chatbots," 2019 15th International Conference on Signal-Image Technology & Internet- Based Systems (SITIS), Sorrento, Italy, 677-680, 2019, doi: 10.1109/SITIS.2019.00110.

[7] N. Nenkov, G. Dimitrov, Y. Dyachenko and K. Koeva, "Artificial intelligence technologies for personnel learning management systems," 2016 IEEE 8th International Conference on Intelligent Systems (IS), Sofia, Bulgaria, 189-195, 2016, doi: 10.1109/IS.2016.7737420.

[8] T. Kita, C. Nagaoka, N. Hiraoka and T. Molnár, "Development of a Moodle UI Using LINE Chat for Casual Learning as a Part of a Learner Assistive LMS," 2020 IEEE International Conference on Teaching, Assessment, and Learning for Engineering (TALE), Takamatsu, Japan, 927-929, 2020, doi: 10.1109/TALE48869.2020.9368321.

[9] W. Kaiss, K. Mansouri and F. Poirier, "Chatbot Design to Help Learners Self-Regulte Their Learning in Online Learning Environments," 2023 IEEE International Conference on Advanced Learning Technologies (ICALT), Orem, UT, USA, 236-238, 2023, doi: 10.1109/ICALT58122.2023.00075.

[10] S. Kesarwani, Titiksha and S. Juneja, "Student Chatbot System: A Review on Educational Chatbot," 2023 7th International Conference on Trends in Electronics and Informatics (ICOEI), Tirunelveli, India, 1578-1583, 2023, doi: 10.1109/ICOEI56765.2023.10125876.

[11] B. Rawat, A. S. Bist, U. Rahardja, Q. Aini and Y. P. Ayu Sanjaya, "Recent Deep Learning Based NLP Techniques for Chatbot Development: An Exhaustive Survey," 2022 10th International Conference on Cyber and IT Service Management (CITSM), Yogyakarta, Indonesia, 1-4, 2022, doi: 10.1109/CITSM56380.2022.9935858.

[12] J. J. Sophia and T. P. Jacob, "EDUBOT-A Chatbot For Education in Covid-19 Pandemic and VQAbot Comparison," 2021 Second International Conference on Electronics and Sustainable Communication Systems (ICESC), Coimbatore, India, 1707- 1714, 2021, doi: 10.1109/ICESC51422.2021.9532611.

[13] S. Ondáš, M. Pleva and D. Hládek, "How chatbots can be involved in the education process," 2019 17th International Conference on Emerging eLearning Technologies and Applications (ICETA), Starý Smokovec, Slovakia, 575-580, 2019, doi: 10.1109/ICETA48886.2019.9040095.

[14] Rasa, « Rasa : IA conversationnelle open source », https://rasa.com/, 20/09/2024 [Online].

[15] Dialogflow, « Dialogflow », https://cloud.google.com/dialogflow, 2024 [Online].

[16] R. Singh, M. Paste, N. Shinde, H. Patel and N. Mishra, "Chatbot using TensorFlow for small Businesses," 2018 Second International Conference on Inventive Communication and Computational Technologies (ICICCT), Coimbatore, India, 1614-1619, 2018

[17] IBM, « IBM Watson », https://www.ibm.com/watson, 23/09/2024) [Online].

[18] A. Abdellatif, K. Badran, D. E. Costa and E. Shihab, "A Comparison of Natural Language Understanding Platforms for Chatbots in Software Engineering," in IEEE Transactions on Software Engineering, **48**(8), 3087-3102, 2022, doi: 10.1109/TSE.2021.3078384.

[19] H. K. K., A. K. Palakurthi, V. Putnala and A. Kumar K., "Smart College Chatbot using ML and Python," 2020 International Conference on System, Computation, Automation and Networking (ICSCAN), Pondicherry, India, , 1-5, 2020, doi: 10.1109/ICSCAN49426.2020.9262426.

[20] M. Ganesan, D. C., H. B., K. A.S. and L. B., "A Survey on Chatbots Using Artificial Intelligence," 2020 International Conference on System, Computation, Automation and Networking (ICSCAN), Pondicherry, India, 1-5, 2020

[21] R. Agrawal, S. Kumar, S. Kumar, N. Goyal and S. Sinha, "WASABI Contextual BOT," 2022 IEEE 4th International Conference on Cybernetics, Cognition and Machine Learning Applications (ICCCMLA), Goa, India, , 481-485, 2022.

[22] M. G. C. P, A. Srivastava, S. Chakraborty, A. Ghosh and H. Raj, "Development of Information Technology Telecom Chatbot: An Artificial Intelligence and Machine Learning Approach," 2021 2nd International Conference on Intelligent Engineering and Management (ICIEM), London, United Kingdom, 216-221, 2021, doi: 10.1109/ICIEM51511.2021.9445354.

[23] Ramineni, K., Harshith Reddy, K., Sai Thrikoteshwara Chary, L., Nikhil, L., Akanksha, P., "Designing an Intelligent Chatbot with Deep Learning: Leveraging FNN Algorithm for Conversational Agents to Improve the Chatbot Performance. In: Tripathi, A.K., Anand, D., Nagar, A.K. (eds)" Proceedings of World Conference on Artificial Intelligence: Advances and Applications. WCAIAA 2024. Algorithms for Intelligent Systems. Springer,

Singapore, 2024.

[24] S. N. M. S. Pi and M. A. Majid, "Components of Smart Chatbot Academic Model for a University Website," 2020 Emerging Technology in Computing, Communication and Electronics (ETCCE), Bangladesh, 1-6, 2020, doi: 10.1109/ETCCE51779.2020.9350903

[25] B. Abu Shawar and E. Atwell, “Chatbots: are they really useful?,” LDV-Forum Zeitschrift für Comput. und Sprachtechnologie, **22**(1), 29–49, 2007.

[26] M. Arya, “A brief history of Chatbots,” 2019. [Online]. Available: https://chatbotslife.com/a-brief-history-of-chatbots-d5a8689cf52f. [Accessed: 29-Nov-2019].

[27] B. Babou, K. Sylla, M. Y. Sow and S. Ouya, "Integration of a Chatbot to Facilitate Access to Educational Content in Digital Universities," 2024 26th International Conference on Advanced Communications Technology (ICACT), Pyeong Chang, Korea, Republic, 311-314, 2024, doi: 10.23919/ICACT60172.2024.10471975.

ASTES

Advances in Science, Technology and Engineering Systems Journal Vol. 10, No. 1, 20-36 (2025)

www.astesj.com

ASTESJ

ISSN: 2415-6698

Analytical Study on the Effect of Rotor Slot Skewing on the Parasitic Torques of the Squirrel Cage Induction Machine

Gábor Kovács*

Ganz Electric Works, 1095 Budapest, Hungary

ARTICLE INFO

Article history:
Received: 20 November, 2024
Revised: 05 January, 2025
Accepted: 06 January, 2025
Online: 24 January, 2025

Keywords:
Induction Motor
Squirrel Cage
Rotor Slot Skewing
Parasitic Torques
Space Harmonics

ABSTRACT

Skewing of the rotor slot of a squirrel-cage induction machine has been commonly used since the beginning. However, little guidance is given regarding the principle of the working effect of the method, but even in such rare cases, the explanation does not cover the true physical reality. Consequently no formula exists for calculation of the effect. In this study, the principle of the working effect of the rotor's skewing is derived in accordance with the true physics of the phenomenon, for both the synchronous and the asynchronous parasitic torque. The calculation regarding synchronous parasitic torque is based on comparing the stepped MMF curve of the straight rotor slot and the trapezoidal MMF curve of the skewed slot. New formulas are provided for both type of parasitic torques. Practical cases are investigated in details. Knowing the theory and the formula of slot skewing, the skew can now be applied on a targeted manner and in some cases, can completely eliminate the dangerous torque and noise components. Consequently, a theorem is formulated on when to skew according to the stator and when acc. to the rotor slot pitch; another theorem was found regarding residual synchronous parasitic torque after skewing. The investigation is then extended to include differential leakage attenuation calculations. With this in mind, from the point of view of rotor slot skew, the topic has been reviewed in its entirety.

1. Introduction

The skewing as a tool against harmful effects of stator slot harmonics is generally used by designer engineers in the industry therefore the topic is discussed in every book dealing with electrical machines. However, all such investigations, which use an analytical method, are aimed only at showing and calculating the effect on the leakage reactance of the machine. This is stated to be independent of whether the stator slot or the rotor slot is skewed. As the stator slot skew really reduces the magnitude of the slot harmonic of the stator MMF to a negligible level, it is concluded that it would also be the case if the rotor slot is skewed for manufacturing reasons.

Even today, intensive research is being conducted on the subject, which proves that researchers are not satisfied with the objective stated above and the generally accepted simple explanation shown below.

The results of the research show that skewing the rotor slot is more or less effective, indeed, but at the same time, the results of the researchers are sometimes in contradiction with each other see e.g. [1] vs. [2]. Many researchers primarily try to present their new calculation method and only use slot skewing as an example, with which they try to prove the correctness of their more advanced methods, and the goal is often not to study the slot skewing itself [3]-[7]. They do not deal with the actual physical working principle of the rotor slot skew, and there is sometimes confusion regarding the effect on the synchronous and/or asynchronous parasitic torque. [8], the experiment that tries to derive the question, correctly, from the rotor's MMF shape; however, the method itself is fundamentally different from ours.

The results from the skew itself and from the quadratic effect of the increase in the leakage reactance, reducing both the starting torque and parasitic torques in the same proportion, are not separated. Analytic approach of the subject is missing.

The goal of this paper is therefore to apply an analytical method, in order to fill the gap and facilitate better understanding.

In the following, first the true principle of working for the rotor slot skew will be presented: a clear distinction is made between the

*Corresponding Author: Gábor Kovács, Email: gabor.kovacs.ganz@gmail.com

https://dx.doi.org/10.25046/aj100104

effect on the synchronous and on the asynchronous parasitic torque, the difference in physics is clearly explained, then new formulas are derived, and calculations are performed. Recommendations are formulated as well.

Then the investigations are extended to the rest of the area of the effect of slot skew, that is, on attenuation of differential leakage. With this, the topic in its entirety is covered.

This paper strongly relies on our previous works [9]-[11]. The entire research is based on [12] as the very basic work of the electrical machine science history, some figures and calculations are copied from [13] and [14].

As a model, such a machine was assumed for which the basic formulas for determining the usual resulting space harmonics are valid [15]: infinite relative permeability, two-dimensional fields without considering boundary and end effects, the machine consist of two smooth coaxial cylinders made of magnetic material, the cylinders are separated by the air gap, the conductors of infinitely small cross-section are located in the air gap. Harmonics of other origin are not involved. Since the derivations as well as the conclusions drawn from the model are based on the fundamental laws of electrical engineering, they do not require validation. The essence of slot skew cannot be understood from FEM calculations, so there is no point in performing FEM calculations before analytical study. Still, as for validation the principle by measurements made by others see Section 9.

2. Symbols

R_1	stator ohmic resistance
X_{s1} - $X_{1\sigma}$	stator leakage without differential leakage reactance
X_m	magnetizing reactance
X_{s2}'	rotor leakage reactance
$X_{\sigma 2}'$	rotor differential leakage reactance
R_2'	rotor resistance reduced to stator
$X_{m\nu}=X_m \cdot 1/\nu^2 \cdot \xi\nu^2/\xi_1^2$	magnetizing reactance of harmonic ν
$X_{\sigma 2\nu}$	rotor differential leakage reactance of harmonic circuit ν
$R_{2\nu}=R_2 \cdot \xi_\nu^2/\xi_1^2$	rotor resistance of harmonic circuit ν
ξ_1, ξ_ν	winding factor of fundamental wave, harmonic wave
$\eta_{2\nu}^2$	Jordan's coupling factor
Δ	attenuation factor, decreasing factor
s, s_ν	slip of rotor to fundamental harmonic of stator; to harmonic ν of stator
ν, μ	designation of stator space harmonics and rotor space harmonics
ε	small positive number $\varepsilon \ll 1$.
a, b	designation of harmonics in interaction
g_1, g_2	different integers
e	integer
p	number of pole pairs
τ_p	pole pitch
θ, θ_m	MMF of one pole
Z_1 , Z_2	stator / rotor slot number
m, m_1, m_2	number of phases, stator, rotor
q_1, q_2'	relative slot numbers: stator/rotor slot number per pole per phase.

3. Critique of Generally Accepted Explanation of the Principle of Effect of Rotor Slot Skew

The effect of operation is usually explained by a figure like Figure 1. The figure is accompanied by the explanation that it is advisable to skew the rotor slots by one stator slot pitch. In this case, the inducing effect of the so-called stator slot harmonics on the rotor bars will be almost completely ineffective.

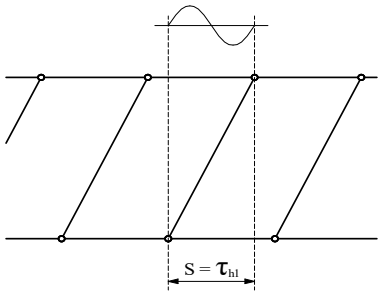

Figure 1: Sketch for explanation of principle of working of rotor bar skew, s – skew, τ_{h1} – stator slot pitch

Figure 1. shows an arrangement in which the bars of the rotor are skewed by just one stator slot pitch; since the $2mq_1$ (otherwise not occurring in reality) harmonic MMF of the stator along the length of the rotor bar completes one complete period, no voltage is induced in it. In other words, the voltage induced in the rotor bar and its phase position, while moving along the length of the bar, moves along a circle, which returns to the initial position upon reaching the end of the bar. The wavelengths of the neighboring harmonics, called $2mq_1 \pm 1$ slot harmonics, which occur in reality, are only slightly different from the previous one, so they only induce a negligible voltage, that is, their effect on the operation of the machine becomes negligible in this way. Instead of the relationship $\xi_{slot} = \xi_1$ so far, the *apparent* relationship $\xi_{slot} \ll \xi_1$ is created, the skew "disappears" the stator slot harmonic.

This explanation is incomplete and therefore misleading. Incomplete in the sense that it is (partially) true regarding asynchronous parasitic torque but it is completely false regarding synchronous parasitic torque. Still the method is generally applied (almost) exclusively against synchronous parasitic torques on an intuitive basis without really considering its true working principle.

Below, it is proven that *explanations and conclusions do not and cannot cover true and complete physical reality.*

The critique is based on Figure 2 which is discussed in every book dealing with asynchronous machines. Therefore it will be discussed here in detail.

The equivalent diagram indicates that an asynchronous machine consists of a series of small asynchronous machines in shaft connection [15]. Each circuit belongs to a ν harmonic of the stator MMF.

The stator harmonics in the diagram, on its "primary" side, appear with a known winding factor ξ_ν. The rotor affects this only to the extent that it *attenuates* some of them and not others. In accordance with practice, our diagram is drawn with the assumption that the stator and rotor slot numbers are not too far apart. In this case, harmonics of lower order than the first slot

harmonic are attenuated, those higher than that are not attenuated [9].

It is a basic law that if a ν^{th} harmonic does not generate current in the cage, it means not more than it does not form an asynchronous parasitic torque with it. In this case, however, that ν^{th} not-attenuated harmonic remains in its *original size* and is still suitable for the formation of a synchronous parasitic torque because no current in the cage by a ν^{th} harmonic means no attenuation of that harmonic.

All this contradict the generally accepted explanation.

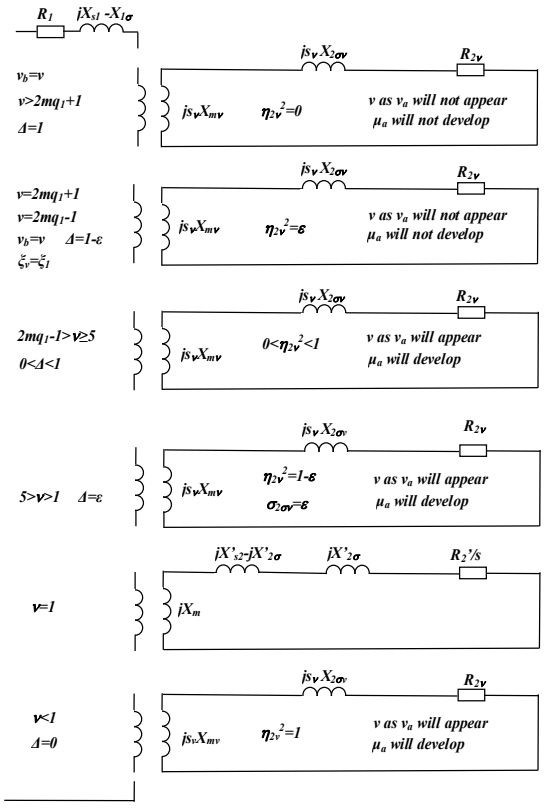

Figure 2: Equivalent circuit including the circuits for the higher harmonics [9]

In Figure 2., only the rotor differential leakage is included as a leakage in the harmonic equivalent circuits [12], [15]. Therefore, the value of the rotor differential leakage will determine how high current will flow in a small harmonic circuit. The differential leakage reactance is [12] (268)

$$X_{2\sigma\nu} = X_{m\nu} \cdot \sigma_{2\sigma\nu} \tag{1}$$

where

$$\sigma_{2\sigma\nu} = \frac{1}{\eta_{2\nu}^2} - 1$$

is the differential leakage factor of the rotor. The denominator in it is the so-called Jordan's coupling factor. Its definition ([12] 268b):

$$\eta_{2\nu_a} = \frac{\sin(\nu \frac{p\pi}{Z_2})}{\nu \frac{p\pi}{Z_2}} \tag{2}$$

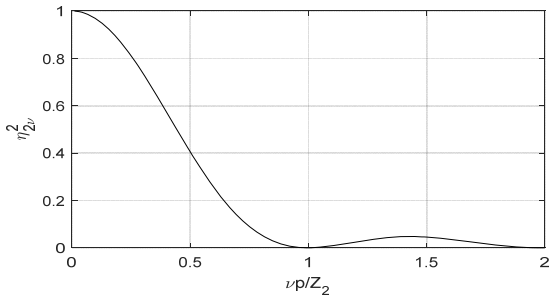

Figure 3: Plotting the value of $\eta_{2\nu}^2$ as a function of $\nu p/Z_2$ ([12] p.154. Figure 107.)

Equation (2) is plotted on Figure 3. It shows how much the rotor responds to a stator harmonic. A zero or very low value indicates that the rotor does not respond to that harmonic. Then the differential leakage factor will be very high or even infinite ([15] Figure 17. p. 44).

For a better illustration, this figure has been modified by us in [9], while the range $\nu p/Z_2>1$ was replaced by zero.

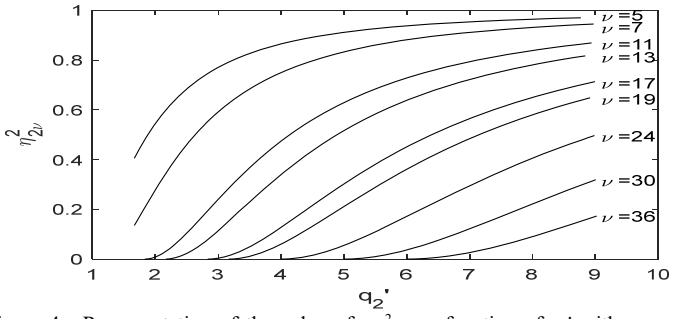

Figure 4: Representation of the value of $\eta_{2\nu}^2$ as a function of q_2' with ν as a parameter. Higher odd harmonics are replaced mathematically by adjacent (actually with 3-phase not existing) even harmonics only for better transparency

The application of the figure will be demonstrated on an example: if e.g. $q_1=3$, then the stator harmonics belonging to it are $\nu=17$ and $\nu=19$.

If then $q_2'\leq 3$, the rotor does not respond to these harmonics (and the harmonics higher than these) *no matter skewed or not skewed.*

If, on the other hand, $q_2'>3$, since $\eta_{2\nu}^2$ is no longer a very small value therefore $\sigma_{2\sigma\nu}$ is no longer an (infinitely) large value the rotor then also responds to the stator slot harmonics and thus a significant asynchronous parasitic torque is generated. This is the point when the slot skewing shall be introduced by the designer, so that the slot harmonic can only induce negligible voltage in the bar.

However, this phenomenon has nothing to do with the generation of synchronous parasitic torque, as it has a different physical basis.

In fact, the rotor skewing was introduced first – in accordance with the true physics – just for suppressing the asynchronous parasitic torques ([12] p. 181, p. 187.) in the case of $Z_2>Z_1$; the explanation added was clearly directed for that purpose: the

$Z_2<1.25 \cdot Z_1$ law was recommended just to prevent high asynchronous parasitic torque with straight bar otherwise slot skewing shall be applied. The solution was later applied (almost exclusively) against synchronous parasitic torques as well on an intuitive basis.

All books on the subject, including [12], explain the phenomenon based on a representation like Figure 1. It is clear that each such figure represents an arrangement where $Z_2<Z_1$. In this case, however, *no asynchronous parasitic torque is created therefore no need to suppress any such torque*. The representation is very close to the situation in which $\tau_{h1}=\tau_{h2}$ (i.e. $Z_2=Z_1$), when the rotor *by definition* does not respond to the slot harmonic of the stator *no matter skewed or not skewed*. *This manner of representation* drew the attention of the author to the fact that the generally accepted explanation *cannot be correct*.

Now the true and complete theory of the whole phenomenon will be presented in a logical sequence of topics for evidencing and better understanding. First, the physics of stator skew and then that of synchronous torque itself will be discussed, dispelling misconceptions; these lay the foundation for the derivation of the formulas. Then we turn to the rotor skew, studying practical cases as well. These help to find and formulate new theorems. Finally accompanying phenomena of the topic will be examined.

4. Skewing of Stator Slots

The slot skew is – acc. to traditional derivation - usually modeled as if the number of slots on an arc equal to the pitch of a slot was infinite. Figure 5. ([13] Figure 113.) was originally developed for the winding distribution factor.

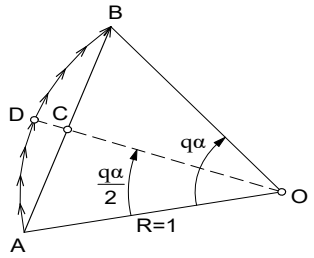

Figure 5: Calculation of the distribution winding factor for an infinite number of stator slots ([13] Figure 113.)

An infinite number of slots entails that the phase position of the voltage induced by the rotating main field in the winding-side sections that are infinitely close to each other moves along a circular arc. The qα range for the m=3 phase is π/3.

Thus, for a skew belonging to one slot pitch: $\alpha/2 = \pi/3 \cdot 1/2q_1 = \pi/6q_1$.

The skew factor acc. to this model (chord per arc)

$$\xi_{skew} = \frac{\sin(\alpha/2)}{\alpha/2} = \frac{\sin(\pi/6q_1)}{\pi/6q_1} \tag{3}$$

The skew factor for the fundamental harmonic is approximately 0.995, that is, the reduction of the main field with skewing by one stator slot pitch is not detectable small.

However, let us substitute the value of the first slot harmonic:

$$\xi_{skewvslot} = \frac{\sin(\nu_{slot} \cdot \pi/6q_1)}{\nu_{slot} \cdot \pi/6q_1} = \frac{\sin((2mq_1+1)\frac{\pi}{6q_1})}{(2mq_1+1)\frac{\pi}{6q_1}} = \ldots = \tag{4}$$

$$= \frac{\sin(\pi/6q_1)}{\pi(1+1/6q_1)} \approx \frac{\sin(\pi/6q_1)}{\pi}$$

The numerator of the fraction is the same as that of the fundamental harmonic; however, its denominator is ~$6q_1$ times higher that means more than one order of magnitude larger. The value of $\xi_{skew\ vslot}$ for $q_1=2$ is approximately 7%, skewing the stator slot is really effective, it "disappears" the slot harmonic of the stator. The skewing of the pole of the synchronous machine can be modeled in the same manner.

A very vivid picture is obtained if the same phenomenon is approached differently.

Let us investigate the MMF curve of one phase of a 3-phase stator winding first for $q_1=1$ acc. to Figure 6. The curve non-skewed is represented by the solid line, that trapezoidal MMF curve created as a result of the stator slot skewing is represented by the dashed line.

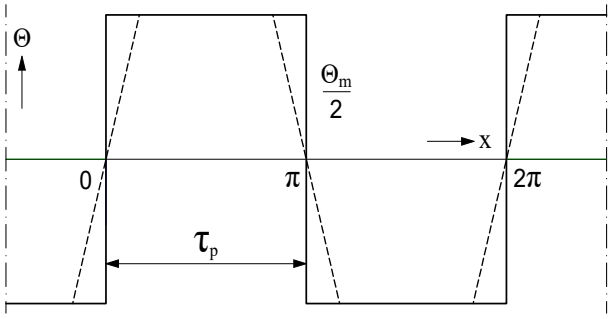

Figure 6: MMF curve of one phase of a three-phase winding, $q_1=1$.

Let us consider the harmonic content of both arrangements.

Fourier series of MMF created by two coil sides lying in non-skewed slots in a pole pitch distance as a function of location along the circumference see Figure 7. (solid line in Figure 6.)

$$\Theta(x) = \frac{4}{\pi}\frac{\Theta_m}{2}\left(\sin x + \frac{1}{3}\sin 3x + \ldots + \frac{1}{\nu_{slot}}\sin \nu_{slot} x + \ldots\right) \tag{5}$$

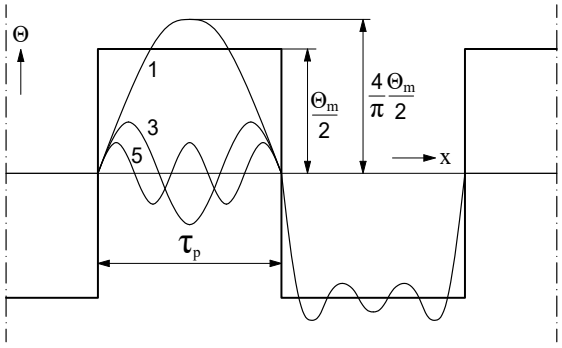

Figure 7: Harmonics of square MMF curve [13] Figure 151.

Let us consider Figure 8. It is originally elaborated for infinite number of stator slots [13]. It is not difficult to notice that the slot skewing by one stator slot pitch and the infinite number of stator slots result in the identical MMF curve.

The Fourier series of MMF created by two coil sides lying in skewed slots in a pole pitch distance as a function of location along the circumference (dashed line in Figure 6.) ([13] (99)

$$\Theta(x)=\frac{4}{\pi}\frac{\Theta_m}{2\beta}(\sin x\sin\beta+\frac{1}{3^3}\sin 3x\sin 3\beta+...+\frac{1}{\nu_{slot}^2}\sin\nu_{slot}x\sin\nu_{slot}\beta+...) \quad (6)$$

For one phase of a three-phase winding, $\beta=\pi/3\cdot 1/2=\pi/6$, generally $\beta=\pi/2m_1$ see (21) later.

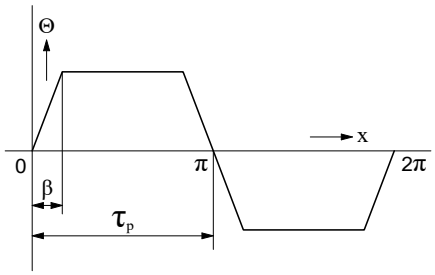

Figure 8: Trapezoidal MMF curve of infinite slot number (q=∞) ([13] Figure 152.)

Proportioning the harmonics formed according to (6) and (5), all harmonics including the fundamental harmonic decrease due to skewing by the factor Δ_{stator} as follows:

$$\Delta_{stator}=1/\beta\cdot 1/\nu\cdot \sin(\nu\beta)=\sin(\nu\beta)/(\nu\beta) \quad (7)$$

Substituting $\beta=\pi/6$ for three-phase the formula for stator slot skewing by exactly one stator slot pitch is:

$$\Delta_{stator}=\frac{\sin\nu\beta}{\nu\beta}=\frac{\sin(\nu\cdot\frac{\pi}{6})}{\nu\frac{\pi}{6}}=\frac{1}{\nu}\frac{3}{\pi} \quad (8)$$

for ν=1, 5, 7, etc.

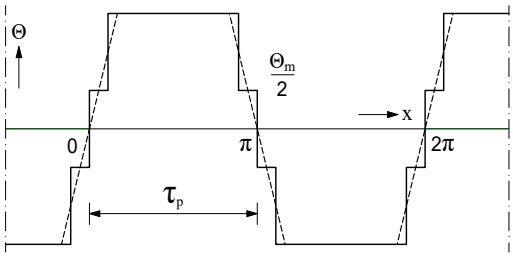

Figure 9: MMF curve of one phase of a three-phase winding, $q_1=3$, full pitch winding

Now the practical cases $q_1>1$ are examined, with q_1 integer, with full pitch winding, see Figure 9.

As it can be seen, the skewed line of one complete phase is the same, it is *independent* of the relative slot number q_1, but the measure of skew created by one coil in two slots is only one-third ($1/q_1$ times) of the previous one.

The formula of Fourier analysis of the solid line of Figure 9. is:

$$\Theta(x)=\frac{4}{\pi}\frac{\Theta_m}{2}(\xi_1\sin x+\frac{1}{3}\xi_3\sin 3x+\frac{1}{5}\xi_5\sin 5x+...+\frac{1}{\nu_{slot}}\xi_{\nu_{slot}}\sin\nu_{slot}x+...) \quad (9)$$

where ξ_ν contains only the distribution factor. The ratio according to (7) has changed, since now the ratio of (6) and (9) shall be formed. The *basic* formula for stator MMF harmonic reduction factor due to slot skewing by exactly one stator slot pitch is:

$$\Delta_{stator}=\frac{1}{\xi_\nu}\frac{\sin\nu\beta}{\nu\beta}=\frac{1}{\xi_\nu}\frac{\sin\nu\cdot\pi/6}{\nu\cdot\pi/6}=\frac{1}{\xi_\nu}\frac{1}{\nu}\frac{3}{\pi} \quad (10)$$

again for ν=1, 5, 7, ...

Substituting for the ratio of the slot harmonics of the skewed and non-skewed slots:

$$\Delta_{stator}=\frac{1}{\xi_{slot}}\frac{\sin\nu_{slot}\beta}{\nu_{slot}\beta}=\frac{1}{\xi_1}\frac{\sin((2mq_1+1)\frac{\pi}{6})}{(2mq_1+1)\frac{\pi}{6}}=\frac{1}{\xi_1}\frac{\sin((2mq_1+1)\frac{\pi}{6})\frac{1}{q_1}}{(2mq_1+1)\frac{\pi}{6}\frac{1}{q_1}} \quad (11)$$

Contrary to expectation, (3) and (11) are not identical, not only because of $\xi_{\nu slot}=\xi_1$ appeared in the formula. The reason for this can be found in Figure 9. The effect of skewing of each slot adds up, the phenomenon works *cumulatively*. This fact is not taken into account by the traditional approach; although the difference is small, theoretically it is not right to apply (3) for the stator skew.

Table 1 summarizes the Δ_{stator} MMF harmonic reduction factors calculated acc. to (10).

Table 1: Reduction Factor of Stator Harmonics by Skewing the Stator by one Stator Slot Pitch, for $q_1=1$, $q_1=2$ and $q_1=3$, full pitch winding

harmonic	ξ_ν	ξ_ν	reduction factor Δ		
ν	$q_1=2$	$q_1=3$	$q_1=1$	$q_1=2$	$q_1=3$
5	0,259	0,217	0,191	0,738	0,878
7	-0,259	-0,178	-0,136	0,527	0,769
11	-0,966	-0,178	-0,087	0,090	0,489
13	-0,966	0,217	0,073	-0,076	0,338
17	-0,259	0,960	0,056	-0,217	0,059
19	0,259	0,960	-0,050	-0,194	-0,052
23	0,966	0,217	-0,042	-0,043	-0,191
25	0,966	-0,178	0,038	0,040	-0,215

It is clear from the table that the respective slot harmonics are effectively reduced, but the non-slotharmonics are reduced only slightly/moderately. This means that slot skewing of the stator removes only the synchronous parasitic torques caused by slot harmonics; the torques produced by non-slot harmonics will be only moderately reduced. The non-slot harmonics are already small due to $\xi_{\nu\text{-non-slot}}<<\xi_1$; those are only slightly reduced further by skewing.

Next would be the examination of chorded windings. These do not create an MMF curve according to Figure 9, but only a similar one, since the height of the "steps" will no longer be identical. Therefore (6) will not be valid; a closed formula cannot be provided. Because several versions of chording are possible, this would result in very extensive and not easily comprehensible tables, so we dispense with this examination for the moment.

If it is not skewed with exactly one stator slot pitch, then the MMF consists of stepped and trapezoidal sections, therefore a closed formula cannot be provided either. Since this way of skew does not happen in practice, we do not deal with it.

5. Synchronous Parasitic Torque

The synchronous parasitic torque is calculated by the circumferential integral of the product of the peripheral current layer $a_{\nu b}$ created by the stator current harmonic order ν_b and the induction $b_{\mu a}$ created by the rotor current harmonic order μ_a [12].

$$M \approx \int_0^{2p\tau} a_{\nu_b} b_{\mu_a} dx \tag{12}$$

The symbol ≈ means here not more than the synchronous torque M is proportional to the integral. The integral differs from zero only, that means, a synchronous parasitic torque is generated only if $\nu_b = \pm\mu_a$. Regarding definitions of harmonics, reference is made to the Appendix.

The induction wave $b_{\mu a}$ is generated by the harmonic of the fundamental harmonic current MMF of the *rotor*. This harmonic current is *not part of the equivalent circuit diagram* because it induces fields with frequencies other than that of the net (much higher than that of the net) [12]; therefore, it does not appear in the stator voltage equations. It depends solely on the fundamental harmonic current of the *rotor* because it is *its* harmonic; in particular, it does not depend on the stator current layer $a_{\nu b}$. If it were to depend, it would be an asynchronous phenomenon, and would thus be part of the equivalent circuit diagram.

The synchronous parasitic torque *cannot* therefore be explained on the basis of Figure 2. For this reason, the approach regarding synchronous parasitic torques that makes the effect of operation of the slot skew dependent whether or not the stator (slot) harmonic induces into the rotor cage loop is *incorrect*. The definition of the synchronous parasitic torque is clearly stated in [15]: "if there are harmonics of the same order in the spectra of the MMF harmonics of the stator and rotor, and this harmonic of the rotor is produced by another harmonic of the stator, $\nu_b \neq \nu_a$, (see Appendix) that is, they are *independent* (*supplement* by the author), then they form a synchronous torque. If it is produced by the same stator harmonic, that is, if $\nu_b = \nu_a$, that is, $b_{\mu a}$ *depends* on $a_{\nu b}$ (*supplement* by the author), then they form an asynchronous torque." We therefore propose the introduction of a *modified* theorem, which has a stronger expressive power in terms of physical message.

The rotor harmonic induction $b_{\mu a}$ decreases as a result of rotor slot skew acc. to (7), the product formed by *unchanged* $a_{\nu b}$ decreases in the same ratio.

This is the true explanation of the principle of effect of rotor slot skew on the synchronous parasitic torque.

It is especially legitimate to speak here of the unchanged current layer wave $a_{\nu b}$ because, as we shall see in Chapter 9., when the rotor slot is skewed, an asynchronous parasitic torque will not occur, therefore no attenuation of the harmonics ν_b occurs.

Once again, the harmonic $a_{\nu b}$ of the stator current layer changes only if asynchronous parasitic torque is created *through* it; therefore, attenuation also occurs simultaneously. Therefore, the two phenomena, skewing and attenuation, must be treated separately.

Now the original equation [12] (310) p. 191., will be quoted in full which by definition is referred to the skewing of the rotor

$$m_{\mu_a \nu_b} = \frac{p\tau l_i}{\pi} \chi_{2\mu_a} \int_0^{2p\tau} a_{\nu_b} b_{\mu_a} dx_1 \tag{13}$$

where

- $m_{\mu a \nu b}$ synchronous torque created by the interaction of harmonics $a_{\nu b}$ and $b_{\mu a}$
- 2p number of poles
- τ pole pitch; $p\tau/\pi$ is the radius of the rotor
- l_i ideal iron core length
- $\chi_{2\mu a}$ the slot skew factor relating to the harmonic number μ_a of the rotor, its definition for an arbitrary harmonic ([12] (206) p.123, (268) p. 154)

$$\chi_{2\nu} = \frac{\sin(\nu \frac{s}{\tau_{h2}} \frac{p\pi}{Z_2})}{\nu \frac{s}{\tau_{h2}} \frac{p\pi}{Z_2}} \tag{14}$$

x_1 is the perimeter location variable of the integration

After formal transformation of (13)

$$m_{\mu_a \nu_b} = \frac{p\tau l_i}{\pi} \chi_{2\mu_a} \int_0^{2p\tau} a_{\nu_b} b_{\mu_a} dx_1 = \frac{p\tau l_i}{\pi} \int_0^{2p\tau} a_{\mu_b} \left(\chi_{2\mu_a} b_{\mu_a}\right) dx_1 \tag{15}$$

Converted in this way, the formula exactly corresponds to the true principle of working effect given above.

This means that [12] showed precisely the theory of effect of rotor skew on the synchronous parasitic torque even at that early time. However, Richter *did not add* any word of an explanation to the formula. It can be assumed that the formula, but especially its physical content, has *therefore* completely escaped the attention of researchers since then, so they have been forced to attempt to calculate the phenomenon using very sophisticated apparatus.

6. Skewing of Rotor Slots

Because $q_2=1$ per definition (see below) for a squirrel cage rotor the harmonics created by the straight bars are given by (5), and those created by the skewed bars are given by (6), the ratio of them is given by (7).

The rotor cage is a multiphase arrangement. The investigation is now conducted with the easiest arrangement, where $Z_2/2p$=integer. In this case, there is another bar of opposite phase at a distance of a pole pitch. With example of $q_1=q_2'=2$, the MMF of the rotor is as if it were an $m_2=q_1m_1=6$-phase, with identical $q_2=1$ winding system arrangement. In this section, q_2 represents the number of slots connected in series, producing MMF in phase. The slot numbers are expressed now:

$$Z_1 = 2pm_1q_1 \tag{16a}$$

$$Z_2 = 2pm_2q_2 \tag{16b}$$

where $q_2 \equiv 1$, which means that there are no cage bars connected in series, no MMF in phase are created. Further rearrangement by applying the usual definition of q_2'

$$Z_2 = 2pm_2 = 2pm_1q_2' \tag{17}$$

then

$$m_2 = m_1q_2' \tag{17a}$$

To date, the most important question is what β should be substituted if the Figure 8. is applied to rotor skew.

In Figures 10a–10d are therefore plotted the MMF curves of one phase of both the stator and rotor for q_1 = 1, 2, and 3 non-skewed and as if both side were skewed by one stator slot pitch at the same time; several rotors were drawn for each stator in the same figure to demonstrate all possibilities. The rotor slot number q_2'=2 1/3 is shown with both one stator slot pitch skew and one rotor slot pitch skew. In the rotor curves, the MMF curve of some adjacent bar pairs, that is, some rotor phases adjacent to the one under consideration, are also indicated. The scale of the MMF in the figures is not the same, allowing easier demonstration.

One stator slot pitch means

$$\tau_{h1} = \frac{2\pi}{2m_1q_1} = \frac{\pi}{m_1q_1} \quad \text{electrical degree} \tag{18}$$

β is half of this:

$$\beta = \frac{\pi}{2m_1q_1} \quad \text{electrical degree} \tag{19}$$

Consequently, regardless of the rotor slot number, if the rotor is skewed by one stator slot pitch β must be substituted according to (19). As shown in Figure 10, the same phenomenon was observed geometrically.

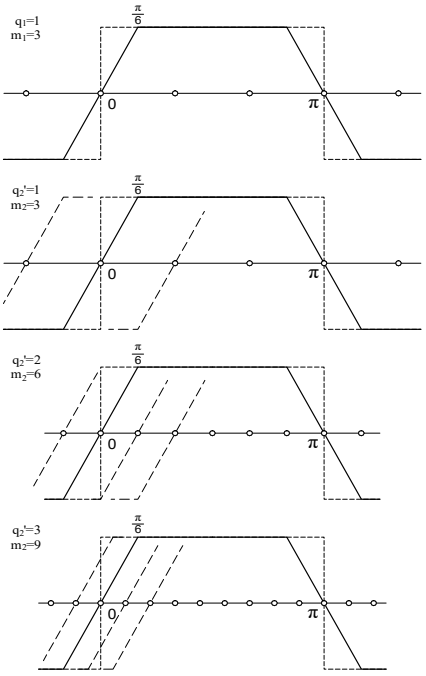

Figure 10 a: q_1=1 q_2'=1, 2, 3

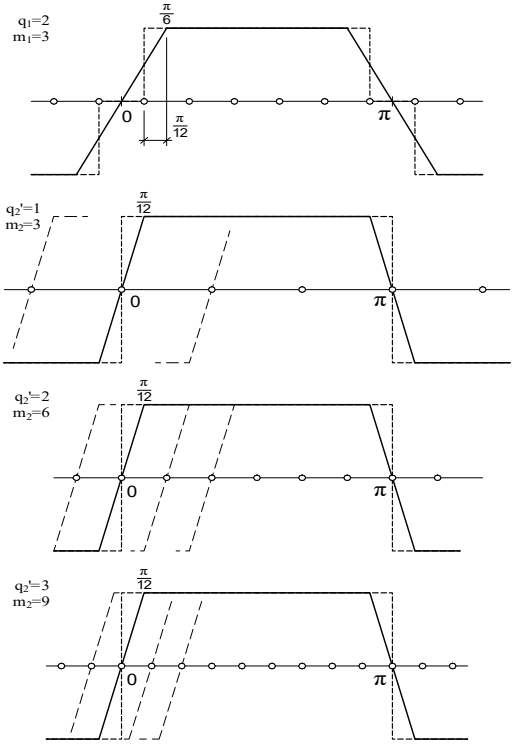

Figure 10 b: q_1=2 q_2'=1, 2, 3

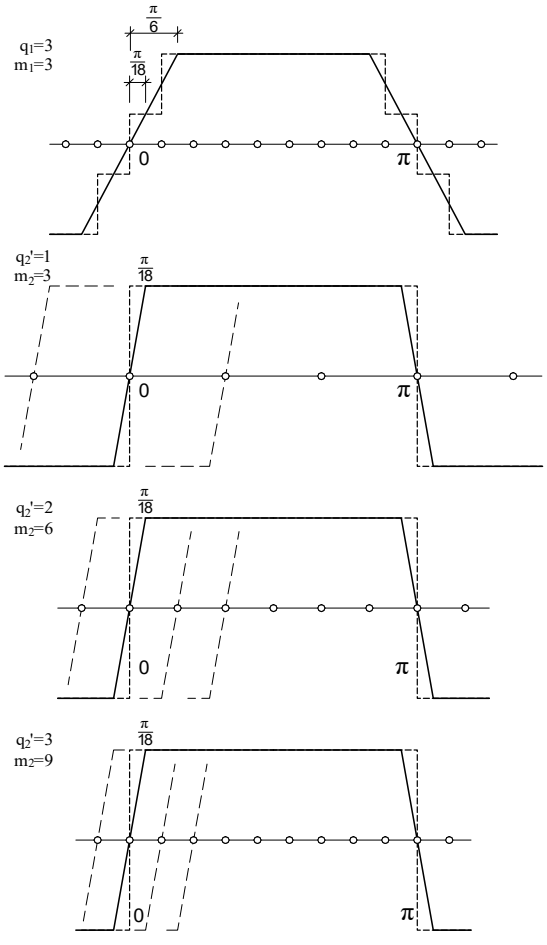

Figure 10 c: q_1=3 q_2'=1, 2, 3

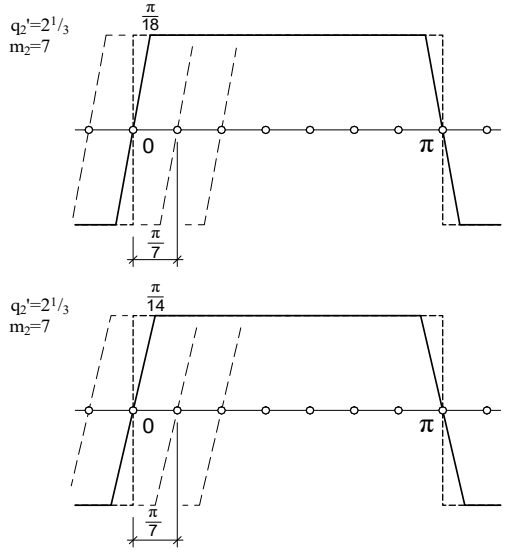

Figure 10 d : q_1=3 q_2'=2 1/3

Figure 10. MMF of one phase of skewed stator and skewed rotor put together in one figure

If the rotor is skewed by one rotor slot pitch

$$\beta = \frac{\tau_{h2}}{2} = \frac{\pi}{2m_1 q_2'} = \frac{\pi}{2m_2} \tag{20}$$

corresponding the remark to (6) before.

If the stator is skewed by one stator slot pitch

$$\beta = q_1 \frac{\tau_{h1}}{2} = \ldots = \frac{\pi}{2m_1} \tag{21}$$

electric degrees. Physically, this occurs because q_1 on the stator also means that the phase of the excitation current in the slot belonging to q_1 slots is identical.

It can be seen that the same rotor slot number installed in a different stator produces a different MMF curve if the rotor is skewed by the actual stator slot pitch.

Table 2: Reduction Factor of Harmonics Produced by the Rotor by Skewing the Rotor by one Stator Slot Pitch

q_1	1	2	3
β	π/6	π/12	π/18
harmonic	reduction factor		
ν	Δ	Δ	Δ
5	0,191	0,738	0,878
7	-0,136	0,527	0,769
11	-0,087	0,090	0,489
13	0,073	-0,076	0,338
17	0,056	-0,217	0,059
19	-0,050	-0,194	-0,052
23	-0,042	-0,043	-0,191
25	0,038	0,040	-0,215

A Fourier analysis of the rotor MMF curves acc. to (24) is given in Table 2. The table provides a very important result. At the arrangement q_1=2, as shown in Figure 10b, β=π/12 acc. to (19). Analyzing the MMF curve of the rotor, only the rotor harmonics of μ= 11-13 and their integer multiples are significantly reduced; the rest of the harmonics are reduced only moderately. In Figure 10c, where acc. to (19) β=π/18, only the rotor harmonics μ=17-19 and their integer multiples are significantly reduced; the rest of the harmonics are only moderately reduced.

Formula (7) is therefore only for a slot harmonic

$$\Delta_{rotor} = \ldots \frac{1}{\beta}(\ldots + \frac{1}{\nu_{slot}} \sin(\nu_{slot}\beta) + \ldots) \tag{22}$$

Substituted

$$\Delta_{rotor} = \frac{\sin \nu_{slot}\beta}{\nu_{slot}\beta} = \frac{\sin((2mq_1 \pm 1)\cdot \frac{\pi}{6q_1})}{(2mq_1 \pm 1)\cdot \frac{\pi}{6q_1}} \approx \frac{\mp \sin(\frac{\pi}{6q_1})}{\pi} \tag{23}$$

being identical with (4) because the effect of rotor slot skewing is not cumulative.

In general, if ν is an arbitrary harmonic of the stator, the *basic* formula for the rotor skewing

$$\Delta_{rotor} = \frac{\sin \nu\beta}{\nu\beta} = \frac{\sin(\nu \cdot \frac{\pi}{6q_1})}{\nu \cdot \frac{\pi}{6q_1}} \tag{24}$$

The sin function in the numerator of the formula gives the phenomenon a specific periodicity in this way as it can be seen on Table 2.: the synchronous parasitic torques produced by non-stator slot harmonics will decrease less.

Regarding Table 1. and Table 2. it is surprising that the value of the Δ reduction factors are identical although the formulas are different. Therefore the phenomenon deserves further examination.

6.1 Remaining synchronous parasitic torque with slot skew by one stator slot pitch

Let's examine the resulting, *remaining* synchronous parasitic torque $M_{residual}$ for both stator skew and rotor skew.

The formula for the calculation of the synchronous torque, which was first derived by us [10] (4):

$$\frac{M_{synchronous}}{M_{breakdown}} = \frac{X_m}{X_s} \cdot 2\sum \frac{\xi_{1\nu_a}\xi_{1\nu_b}}{\mu_a} \eta_{2\nu_a}^2 \frac{1}{\xi_1^2} \tag{25}$$

where

$$\eta_{2\nu} = \frac{\sin \nu \frac{p\pi}{Z_2}}{\nu \frac{p\pi}{Z_2}} = \frac{\sin \nu \frac{\pi}{2mq_2'}}{\nu \frac{\pi}{2mq_2'}}$$

M torque

X_m, X_s reactance, magnetizing, leakage

ξ_{1va} , ξ_{1vb} , ξ_1	winding factor of harmonics, of fundamental harmonic
η_{2v}	Jordan's coupling factor
ν_a ,ν_b , μ_a	space harmonic order numbers stator, rotor
m	number of phases
Z_2	rotor slot number
2p	pole number
q_2'	relative rotor slot number

Now, a simplification and approximation $\xi_{1va}\cdot\eta_{2v}^2/\xi_1^2\approx1$ is applied, since only the quantities produced by the fundamental harmonic are considered for the moment: ν_a =1. Factors not important at the moment are eliminated in this way. Thus the formula applied:

$$\frac{M_{synchronous}}{M_{breakdown}} = 2\frac{X_m}{X_s}\frac{\xi_{1\nu_b}}{\mu_a} = 2\frac{X_m}{X_s}\frac{\xi_{1\nu_b}}{\nu_b} \tag{26}$$

ν_b = μ_a is as condition of occurring synchronous parasitic torque.

The resulting, residual synchronous parasitic torque in case of *stator* slot skew from (10)

$$\frac{M_{residual}}{M_{breakdwn}} = \frac{M_{synchronous}}{M_{breakdown}}\Delta_{stator} = 2\frac{X_m}{X_s}\frac{\xi_{1\nu_b}}{\nu_b}\frac{1}{\xi_{1\nu_b}}\frac{1}{\nu_b}\frac{3}{\pi} = 2\frac{X_m}{X_s}\frac{1}{\nu_b^2}\frac{3}{\pi} \tag{27}$$

The surprising result is that regardless of q_1, regardless whether ξ_{1vb} was a slot-harmonic or not while skewing, the residual synchronous parasitic torque is the same; it depends only from the harmonic order number creating that torque.

The resulting residual synchronous parasitic torque in case of *rotor* slot skew from (24)

$$\frac{M_{residual}}{M_{breakdwn}} = \frac{M_{synchronous}}{M_{breakdown}}\Delta_{rotor} = 2\frac{X_m}{X_s}\frac{\xi_{1\nu_b}}{\nu_b}\frac{\sin(\nu_b\pi/6q_1)}{\nu_b\pi/6q_1} \tag{28}$$

Substitute ξ_{1vb}

$$\xi_{1\nu_b} = \frac{\sin(\nu_b\pi/6)}{q_1\sin(\nu_b\pi/6q_1)} \tag{29}$$

$$\frac{M_{residual}}{M_{breakdown}} = \frac{M_{synchronous}}{M_{breakdown}}\Delta_{rotor} = 2\frac{X_m}{X_s}\frac{1}{\nu_b}\frac{\sin(\nu_b\pi/6)}{q_1\sin(\nu_b\pi/6q_1)}\frac{\sin(\nu_b\pi/6q_1)}{\nu_b\pi/6q_1} =$$

$$= 2\frac{X_m}{X_s}\frac{1}{\nu_b}\frac{\sin(\nu_b\pi/6)}{\nu_b\pi/6} \tag{30}$$

It is not difficult to notice that the last term of (30) is identical to (10). Finally

$$\frac{M_{residual}}{M_{breakdown}} = 2\frac{X_m}{X_s}\frac{1}{\nu_b^2}\frac{3}{\pi} \tag{31}$$

Both (27) and (31) result in the outcome being independent of q_1 and q_2' and whether ξ_{1vb} was a slot-harmonic or not while skewing; the result depends only from the harmonic order number creating that torque. Furthermore, (27) and (31) give the same result, although the formulas of the reduction factors for the stator and rotor skewing are different. It has now been proven with formula that the skewing by one stator slot pitch, whether it is performed on the stator or the rotor, gives the same result, the two skews are equivalent. Formulating as theorem:

Skewing by one stator slot pitch results in the same residual synchronous parasitic torque with q_1 = integer, full pitch stator winding regardless whether the skew is performed on the stator or the rotor, the two skews are equivalent.

The value of the remaining, residual synchronous parasitic torque is always the same, it is independent of the (relative) number of slots of both on the stator and on the rotor, as well as independent of the winding factor of the stator harmonic participating in the generation of that torque (thus whether it is slot harmonic or not). It depends only from the order number of harmonics participating in the generation of the synchronous parasitic torque. However, since that harmonic order number depends solely on the rotor slot number per pole, not on the combination of the stator and rotor slot numbers, the whole phenomenon depends solely on the rotor slot number at the end.

Note that the above formulation does not mean that the stator and rotor skews are not equivalent for the rest of stator windings that means for those other than integer q_1 full pitch winding; it merely means that the present derivation proves it only for this particular case.

It shall be remarked that when calculating the values with slot skew the modification of the leakage reactance (see Section 9. later) is not considered at the moment.

6.2. Application of the rotor slot skew in practice

Looking at the effect of skewing, that is, at the number of rotor slots which is worth or even necessary to skew, let us examine whether it is possible to set up a "rule of thumb".

As an illustration, consider [11] Table VI, which deals with a wide range of number of slots in four poles; data are taken from there.

For such slot numbers and torque-order numbers, where only the slot harmonics of the stator appear, a significant reduction occurs. These are rotor slot numbers that create synchronous parasitic torque only in standstill: q_1=q_2', q_2'=integer, and the so-called half-slot numbers, for which q_2'=q_2+1/2 (where q_2 is a simple positive integer); in general, where the denominator is neither equal to the phase number of the stator nor its integer multiple [11]. For these, skewing yields a significant result; however, the initial synchronous parasitic torque is by far the highest just for these slot numbers. These will be investigated in the next section.

Now, corresponding to practice, which practice in not really understandable for the author, the q_2'=q+1/3 (so-called third slot) dangerous rotor slot numbers will be investigated; they are dangerous because the synchronous parasitic torque created by the lowest order harmonic occurs in the motor range [11].

Consider slot number Z_2=28 as an example. Acc. to [11] the critical harmonic is ν=13 .

At slots 24/28 [11], ν=13 is just the stator slot harmonic, which the skewing has significantly reduced, but the question is whether this is sufficient. By calculation (β=π/12):

$$\text{to } \mu_a = -13 \quad \frac{\sin 13\pi/12}{13\pi/12} \approx \frac{0.26}{\pi} = 0.08$$

Residual synchronous parasitic torque [11]:

$$2.27 \cdot 0.08 = 0.18\ M_{break}.$$

Further a significant torque is generated at standstill by substituting e=±6 by ν_b = -83 - 85: 0.7 M_{break} which will be reduced by skewing to ≈(1/4)/7π= 0.008 M_{break} , to practically zero, thanks to that harmonic being very high.

At the inexplicably popular 36/28 slot number, although the torque in the motor range is created by the stator non-slot-harmonic, it is still dangerous but the effect of the skewing is limited. The effect of skew on the torques created by the lowest harmonics (β=π/18):

$$\mu_a = -13 \qquad \frac{\sin 13\pi/18}{13\pi/18} = 0.33 \qquad \text{is moderate.}$$

Without skewing [11] M_{synchr}/M_{break} = 0.51
With skewing: 0.51·0.33 = 0.17 M_{break}

$$\mu_a = 29 \qquad \frac{\sin 29\pi/18}{29\pi/18} = 0.185$$

$$\mu_a = -55 \ \frac{\sin 55\pi/18}{55\pi/18} = 0.018 \qquad \mu_a = 71 \ \frac{\sin 71/18}{71\pi/18} = 0.014$$

The following comments can be made about the calculation:

- in this example only (against the general rule), significant standstill torque is not created

- it is questionable whether the reduction in the parasitic torque occurring in the motoric range of the smallest order number is sufficient

- there is enough to deal with order numbers up to twice the number of slots per pole pair of the stator

- it can be seen from the formula that if the denominator in the sin function would be 14 instead of 18, both remaining low order synchronous torques would disappear. By calculation (β=π/14):

$$\frac{\sin 13\pi/14}{13\pi/14} \approx \frac{0.225}{\pi} = 0.072 \ .$$

Residual synchronous parasitic torque:

M_{synchr}/M_{break}= 0.51·0.072=0.036 ; it is an effective skewing.

It is not difficult to notice that this is just skewing by one *rotor* slot pitch, as shown in Figure 10d. This is not surprising because both low order harmonics originate from the rotor slot number.

The 48/28 slot number, which is of theoretical interest only, is also better to skew by one rotor slot pitch.

Returning back to 24/28 machine, the reduction factor with stator slot skew (β=π/12) or with rotor slot skew (β=π/14) is almost the same. In case of β=π/13=π/$\nu_{b\text{-critical}}$, however, the synchronous torque drops to mathematical zero. If Möller had skewed at this slot number not according to the stator slot pitch, but according to the critical harmonic, he would have obtained a mathematical zero torque. The resulting noise component would also be mathematically zero. Such consideration has relevance only in case of synchronous torque in rotation. In case of synchronous torque in standstill, it is skewed always against *two* harmonics ν=2mq_1±1 expediently by 2mq_1.

This arrangement is a good example of how the skew can be used in a really targeted manner. It indicates that *the stator slot harmonic and/or the skewing by one stator slot pitch does not play such an exclusive role* as is usually attributed to it.

Table 3. shows the effect of skewing the rotor by one rotor slot pitch acc. to (24). It is clear that such skewing effectively reduces just the rotor slot harmonics.

Table 3: Reduction Factors of Harmonics Produced by the Rotor by Skewing the Rotor by one Rotor Slot Pitch

q_2'	2 1/3	2 2/3	3 1/3	3 2/3
β	π/14	π/16	π/20	π/22
harmonic	reduction factor			
ν	Δ	Δ	Δ	Δ
5	0,803	0,847	0,900	0,917
7	0,637	0,714	0,810	0,842
11	0,253	0,385	0,572	0,637
13	0,076	0,218	0,436	0,517
17	-0,163	-0,058	0,170	0,270
19	-0,211	-0,149	0,052	0,153
23	-0,175	-0,217	-0,126	-0,043
25	-0,111	-0,200	-0,180	-0,116
29	0,034	-0,098	-0,217	-0,203
31	0,090	-0,032	-0,203	-0,217

Based on this, the following theorem can be established:

- *if the dangerous synchronous parasitic torque is created by ν_b that is a stator slot harmonic, then skewing by one stator slot pitch must be applied, if ν_b is not a stator slot harmonic (but obviously a rotor slot harmonic) then skewing by one rotor slot pitch must be done.*

- *further: if the synchronous parasitic torque is generated in standstill, it is created always by stator slot harmonics, therefore skewing with a stator slot pitch must be used. If the synchronous torque is generated in rotation, it shall be proceeded according to the provisions of the previous paragraph. In this case, however, it is possible to skew neither acc. to stator slot pitch nor acc. to rotor slot pitch but according to the critical harmonic to be suppressed and then the resulting torque is mathematically zero.*

Analysis like in [11] Table VI. is therefore indispensable.

It should be noted that the result for the slot harmonic is *sensitive to the accuracy of skew* compared to the theoretical one, corresponding to the variation of the sin function near π. For example, if the critical harmonic is ν=13 and the theoretical skew is β=π/12, then a slight difference in the actual skew might lead to a change in a ratio of up to 1:2. Calculation for the rotor slot skew

$$\frac{\sin 13\pi/11}{13\pi/11} = 0.15 \qquad \frac{\sin 13\pi/12}{13\pi/12} = 0.08 \qquad \frac{\sin 13\pi/13}{13\pi/13} = 0$$

With the mathematical proof, the differential $d\Delta_{rotor}/d\beta$ of (24) must be formed. Omitting the details of the mathematical analysis, the differential near $\nu\beta\approx\pi$ is $\approx 1/\beta=2m_1q_2'/\pi$. In the example: the appr. value is: $1/\beta = 3.82$; the exact value of the differential is: 3.67; it is very high. The sensitivity increases linearly with q_2'.

The investigated sensitivity has significance only in the case of the synchronous torque in rotation, where it is skewed against a single harmonic. In the case of synchronous torque in standstill, it is skewed by $2mq_1$ against two harmonics, $\nu=2mq_1+1$ and $\nu=2mq_1-1$, so a slight inaccuracy in the skewing is irrelevant.

7. Summation of Synchronous Parasitic Torques Occurring in Standstill

This chapter is a further development and partially *fundamental* modification of Chapter E 2 of [11].

Let us take the slot layout 36/36 and 24/24 as example; they are also frequently investigated by researchers.

The need to sum synchronous parasitic torques in standstill arises only for those rotor slot numbers that produce synchronous parasitic torque only in standstill; however, in this case, summation is always necessary. The rotor slot number is expressed in the usual way: $q_2'=q_2+p/r$, where q_2 is a positive integer, p and r are positive integers, and $p\leq r$. If r is not equal to the stator phase number or an integer multiple thereof, the need for summation always arises [11].

In such a case it is a matter of summing *spatial* torque components, which are expressed vectorially:

$$M = e^{j\delta} + \frac{1}{2}e^{j2\delta} + \frac{1}{3}e^{j3\delta} + \frac{1}{4}e^{j4\delta} + \frac{1}{5}e^{j5\delta} + \frac{1}{6}e^{j6\delta} + \ldots \quad (32a)$$

On trigonometric way:

$$M = \sin\delta + \frac{1}{2}\sin 2\delta + \frac{1}{3}\sin 3\delta + \frac{1}{4}\sin 4\delta + \frac{1}{5}\sin 5\delta + \frac{1}{6}\sin 6\delta \ldots \quad (32b)$$

δ is the angular position of the rotor related to one rotor slot pitch.

We are looking for the maximum of this.

This infinite series is the Fourier-solution of the function

$$f(x) = \frac{\pi - x}{2} \text{ , } 0<x<2\pi \text{ , } f(0)=0 \quad (33)$$

Here x stands for δ.

The maximum of the infinite series is $\pi/2$ times the first, largest torque component and occurs at x=0. However, the maximum of the finite series can be higher, as shown in Figure 11.

This series acc. to (32a) and (32b) are typical of the 36/36, 24/48 and 24/18 slot arrangements.

It can be seen from (32a) and (32b) that the magnitude of the higher order spatial harmonics decreases only "slowly," the higher orders cannot be neglected in any way; therefore, their exact summation is of fundamental importance. At the same time, we also saw in [10] that one should not go to infinite summation.

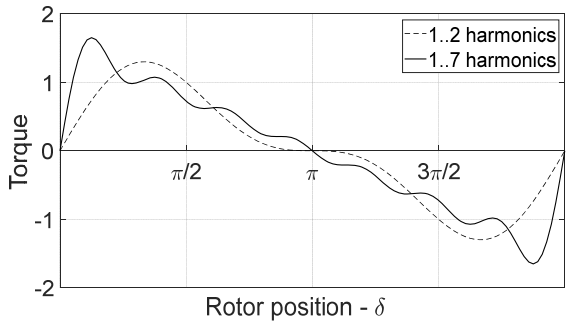

Figure 11: Synchronous parasitic torque occurring at standstill as a function of the angular position of the rotor for 36/36 slots

We performed our calculations for Figure 11. and Figure 12 for the harmonic order up to $\nu_b \leq 150$ [11]. Correspondingly, the first seven torque components for the 36/36 slot number and the first ten torque components for the 24/24 slot number must be included in the calculation.

A representation of the line with the first seven torque components is shown in Figure 11.

The value of the maximum torque is 1,67 times the value of the first torque component, which occurs at $\delta=0.34\approx\pi/9$.

In the other case, the sign of the components alternates, that of the even components is negative, this is typical of 24/24, 48/48, 24/30 and other slot numbers.

The series is:

$$M = \sin\delta - \frac{1}{2}\sin 2\delta + \frac{1}{3}\sin 3\delta - \frac{1}{4}\sin 4\delta + \frac{1}{5}\sin 5\delta - \frac{1}{6}\sin 6\delta \ldots \quad (34)$$

This infinite series is the Fourier-solution of the function

$$f(x)=x/2 \qquad -\pi< x <\pi \text{ , } f(\pi)=0 \quad (35)$$

The maximum of the infinite series is again $\pi/2$ times the first, the largest torque and occurs at $x=\pi$.

A representation of the line with the first ten torque components is shown in Figure 12.

The value of the maximum torque is 1,71 times the value of the first torque component and occurs at $\delta=2.86\approx 8/9\pi$.

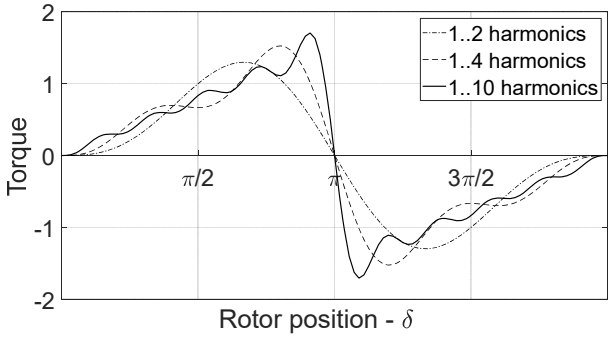

Figure 12: Synchronous parasitic torque occurring at standstill as a function of the angular position of the rotor for 24/24 slots

The effect of skew is calculated by multiplying each torque component as a function of the angular position of the rotor by the

corresponding skew reduction factor Δ, and then summing them up. Because the skew affects each component differently, the final result cannot be included in a formula, but a manual summation would be required. It is certain here that the summation of not 7 or 10 waves, but rather only 2-3 waves may become necessary; the number 2 wave will be stronger reduced, and that of number 3 will be much stronger; therefore, not much error will be made if the summation is actually dispensed with for a skewed machine. The decrease of the first, highest torque component:

$$\text{for } q_1=q_2'=2 \quad \frac{\sin 11\pi/12}{11\pi/12} \approx \frac{1/4}{\pi} = 0.08$$

$$\text{for } q_1=q_2'=3 \quad \frac{\sin 17\pi/18}{17\pi/18} \approx \frac{1/6}{\pi} = 0.053$$

$$\text{for } q_1=q_2'=4 \quad \frac{\sin 23\pi/24}{23\pi/24} \approx \frac{1/8}{\pi} = 0.04$$

The synchronous parasitic torque remaining after skewing [11]

for $q_1=q_2'=2$ $4.92 \cdot 0{,}08 = 0.4$ M_{break}
for $q_1=q_2'=3$ $3.31 \cdot 0.053 = 0.175$ M_{break}
for $q_1=q_2'=4$ $1.3 \cdot 0.04 = 0.05$ M_{break}

It should be noted here that the so-called “half slot” numbers ($q_2'=q_2 \pm 1/2$) quite rightly escape the attention of designers. With slot skew, however, for example, at 24/30 slot number, the remaining synchronous parasitic torque in standstill is [11]: $\approx 0.99 \cdot (1/4)/(5\pi) = 0.016$ M_{break} practically zero. While a straight rotor slot is out of question, skewing makes this slot number usable without problems if skewed by one stator slot pitch. In addition, for 36/30 and 48/30 slot numbers, too. We therefore encourage designers to use this arrangement.

8. Calculation of the Change of the Leakage Reactance of the Machine

In addition to the previous phenomena, another change takes place in the machine, as the reactance of the machine also change, in a well-known way. From this point of view, the change in leakage reactance has a greater effect, although minor changes in the fundamental magnetization reactance can also be experienced. Let us calculate the effect of this change for the machine typically characterized by $X_m=3$, $X_s= 0.2$ ($I_{starting}=5 \cdot I_{rated}$), and $X_m/X_s = 15$, used in all our studies so far.

The winding factor of the skew of the rotor with one stator slot pitch is obtained from (4) for $q_1 =q_2'= 3$ [14]

$$\xi_{skew} = 1-0.41 \cdot (1/3q_1)^2 = 0.995 \quad (36)$$

the leakage coefficient of the skew

$$\sigma_{skew} = 2 (1- \xi_{skew}) = 0.0102 \quad (37)$$

excess leakage reactance

$$X_s = X_m \cdot \sigma_{skew} = 0.0306 \quad (38)$$

the rate of change of the leakage reactance:

$$x_{s\Delta}=0.2 / 0.23 = 0.87 \quad (39)$$

The machine's data changed as a result of skewing:

$X_m = 2.97$ $X_s = 0.23$ $X_m / X_s = 12.91$

The ratio of reactance instead of 15 for the skewed machine is 12.91, the ratio of change

$$x_\Delta = 12.91/15 = 0.86 \quad (40)$$

The synchronous parasitic torque relative to the actual breakdown torque decreased in proportion to x_Δ. Note that the calculations in Sections 4. and 6. do not contain this factor at the moment. The breakdown torque of the machine also decreased, in proportion to $x_{s\Delta}$, this is the "price to be paid" or “trade-off” for the advantage of skewing what designer need to consider. The absolute value of the synchronous parasitic torque decreases in proportion to the product of $x_{s\Delta} \cdot x_\Delta$.

However, this value is deliberately not calculated now. The reduction of the synchronous parasitic torque and the breakdown torque of the machine in the same proportion cannot be considered as a useful consequence of skewing; on the contrary, it specifically limits the extent of skewing.

9. The Effect of Skewing on the Asynchronous Parasitic Torques

The relevant part of the measurement series carried out by Möller [16] citied already by us before is repeated here on Figure 13. One rotor skewed by one stator slot pitch was also manufactured and measured for one of the 19 rotors examined by Möller.

A comparison of the measurements 24/28 slots with straight and skewed rotor slots shows the expected reduction in the synchronous parasitic torque.

However, another important phenomenon has also emerged. When measuring the straight-slot rotor ($Z_2>Z_1$ in this case), significant asynchronous torques were experienced, namely, by the low-order 5th and 7th harmonics and the 11th and 13th harmonics being stator slot harmonics. However, asynchronous parasitic torques practically disappear in the skewed machine. Therefore subject measurement represents strong evidence for us regarding the complete explanation; it validates the theory provided by us.

In the case of a skewed bar, the voltage and its phase position induced in the rotor bar, while moving along the bar, describe a complete circle, which, in the case of the 12th harmonic, reaches the end of the bar covering just 360° and returns to the initial position. The 11th harmonic only travels 330°, so its original value is reduced to 1/11 of the chord/circumference arc ratio, that is, its inducing effect practically disappears. Additionally, to 1/13 of the 13th harmonic. This phenomenon has also reduced the inducing effect of the 7th and 5th harmonics, ≈2/7 and ≈2/5 in the chord/arc proportion. It is of basic importance that the disappearance of the asynchronous torque also means that an attenuation effect on the concerned harmonics does not occur. Therefore, the 13th harmonic of the stator, remaining in magnitude, was still able to create a high synchronous parasitic torque. It was the 13th harmonic of the *rotor*, however, which was decreased by skewing and caused a reduction in the synchronous parasitic torque at the end. *This is the complete physic, the complete effect of the rotor skewing.*

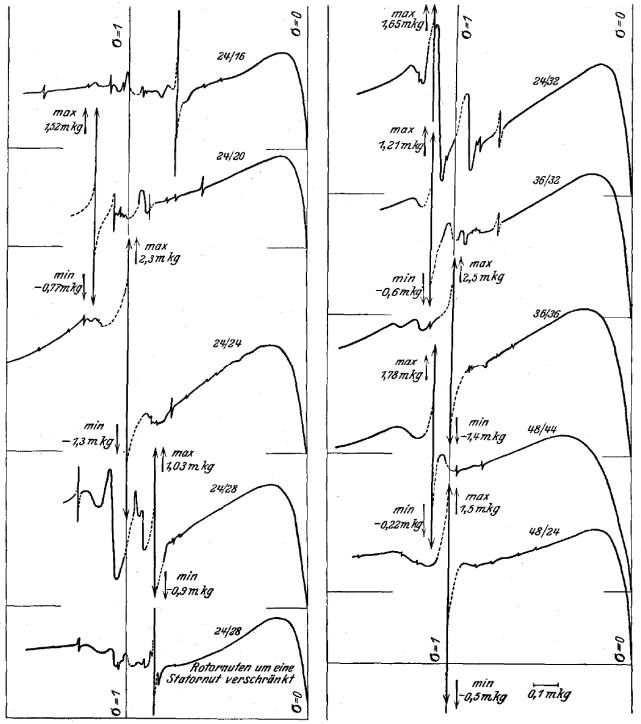

Figure 13: Highest synchronous torques, the measured values are given in mkg see Möller [16] Figure 8.

The rotor slot skewing, in accordance with the true physical background, did not eliminate the synchronous parasitic torque but eliminated the asynchronous parasitic torque; the synchronous parasitic torque was only reduced.

Now, a formula for calculating the exact value will be derived. To do this, the changes in the elements of an arbitrary harmonic circuit, as shown in Figure 2 is examined.

Definition of the skew factor of the rotor slot acc. to (14) ([12] (206) and (268a)) again

$$\chi_{2\nu} = \frac{\sin(\nu \frac{s}{\tau_{h2}} \frac{p\pi}{Z_2})}{\nu \frac{s}{\tau_{h2}} \frac{p\pi}{Z_2}} \tag{41}$$

Substitute the β value corresponding to the skew of a rotor with one rotor slot pitch in (7): $s/\tau_{h2}=1$, $\beta=\pi/2mq_2'=\pi/(Z_2/p)$. We obtained the unsurprising result that formula (41) based on physical considerations and formula (7) obtained from Fourier analysis are identical.

Note that if $s=\tau_{h2}$, i.e. we skew with exactly one rotor slot pitch, then (41) is the same as the definition of $\eta_{2\nu}$ acc. to (2), i.e. $\chi_{2\nu}$ is equal to $\eta_{2\nu}$. This does not originate from their physical content, but later, in the evaluation of (51), we make use of this identity.

The derivation will follow the way, used first by us, in [9], by inserting $\chi_{2\nu}$ into the assigned formulas.

The main field reactance of the fundamental harmonic changes linearly with the skew factor $X_{m\chi}=X_m \cdot \chi_{2,\nu=1}$. The $X_{m\nu}$ reactance, which means the "main field" reactance for the harmonic circuit, is

$$X_{m\nu\chi} = X_{m\nu} \cdot \chi_{2\nu} \tag{42}$$

accordingly.

The complete definition of the differential leakage coefficient ([12] (268))

$$\sigma_{2\sigma\nu\chi} = \frac{1}{\chi_{2\nu}^2 \eta_{2\nu}^2} - 1 \tag{43}$$

The differential leakage

$$X_{s\sigma 2} = (\frac{1}{\chi_{2\nu}^2 \eta_{2\nu}^2} - 1) X_{m\nu} \chi_{2\nu} \tag{44}$$

The total reactance of the harmonic circuit

$$X_{m\nu}\chi_{2\nu} + (\frac{1}{\chi_{2\nu}^2 \eta_{2\nu}^2} - 1) X_{m\nu}\chi_{2\nu} = \ldots = \frac{X_{m\nu}}{\chi_{2\nu}\eta_{2\nu}^2} \tag{45}$$

differs from the original value in the proportion $1/\chi_{2\nu}$. “Main field” reactance decreased, leakage reactance increased.

Again, in harmonic circuits, only the differential leakage reactance is included as the leakage reactance; the rest of reactance are negligible [12], [15]. To calculate the harmonic breakdown slip, the change in resistance must also be taken into account, since the resistance reduction factor of the unchanged rotor resistance changes in the ratio $1/\chi^2$ ([12] (170) p. 100). The harmonic breakdown slip

$$s_{b\nu\chi} = \frac{R_{2\nu}/\chi_{2\nu}^2}{(X_{2m\nu} + X_{2\sigma\nu})/\chi_{2\nu}} = \frac{R_2}{X_m} \nu^2 \eta_{2\nu}^2 \frac{1}{\chi_{2\nu}} = \frac{s_{b\nu}}{\chi_{2\nu}} \tag{46}$$

$s_{b\nu}$ changes, the scale of slip too.

Acc. to voltage equation supplemented by $\chi_{2\nu}$ accordingly:

$$I_{2\nu} = -j \frac{s_\nu X_{2m\nu}\chi_{2\nu}}{R_{2\nu}/\chi_{2\nu}^2 + j s_\nu (X_{2m\nu} + X_{2\sigma\nu})/\chi_{2\nu}} I_1 \tag{47}$$

The endpoint of $I_{2\nu}$ describes a circle as a function of s_ν, as shown in Figure 14. but the scale is different due to $\chi_{2\nu}$.

Arranged and substituted

$$I_{2\nu} = -j \frac{s_\nu \chi_{2\nu} \cdot \eta_{2\nu}^2}{s_{b\nu\chi} + j s_\nu} I_1 = \ldots = (-\frac{s_\nu^2 \chi_{2\nu} \cdot \eta_{2\nu}^2}{s_{b\nu\chi}^2 + s_\nu^2} - j \frac{s_\nu s_{b\nu\chi} \chi_{2\nu} \cdot \eta_{2\nu}^2}{s_{b\nu\chi}^2 + s_\nu^2}) I_1 \tag{48}$$

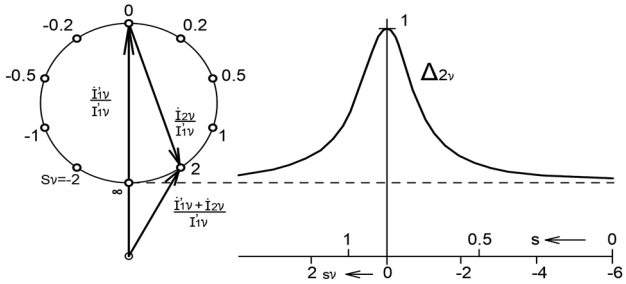

Figure 14: Vector diagram of the currents of the harmonic circuit ν=7 and the attenuation factor $\Delta_{2\nu}$ belonging to this circuit (=to this harmonic) (see [12] Richter Vol. IV p. 150, Figure 106)

The imaginary component creates the torque. Substituting $s_{b\nu\chi}$ acc. to (46) then $s_\nu = s_{b\nu\chi}$ yields

$$I_{2\nu} = \ldots - j\frac{\chi_{2\nu}\cdot\eta_{2\nu}^2}{2} I_1 \tag{49}$$

changed in proportion $\chi_{2\nu}$.

The maximum power

$$P_{\max\chi} = 3\cdot U_{1\nu}\cdot I_{2\nu} = 3\cdot I_1 jX_{m\nu}\chi_{2\nu}(-j\frac{\chi_{2\nu}\eta_{2\nu}^2}{2})I_1 = P_{\max}\chi_{2\nu}^2 \tag{50}$$

changed by the square of $\chi_{2\nu}$.

The change the asynchronous breakdown torque is therefore

$$\frac{M_{b\nu\chi}}{M_b} = \frac{X_m}{X_s}\frac{\xi_\nu^2}{\xi_1^2}\frac{\eta_{2\nu}^2}{\nu}\chi_{2\nu}^2 = M_{b\nu}\chi_{2\nu}^2 \tag{51}$$

The formula correctly shows the effect of the factors ξ_ν^2, ξ_1^2, $\eta_{2\nu}^2$ and $\chi_{2\nu}^2$ on the harmonic torque of ν, in accordance with the physical picture. The effect, including the quadratic effect of slot skew, is consistent with [12] (293) p. 180.

The result would have been accurate (slightly smaller) if $(I_1+I_2)\cdot jX_{m\nu}$, the absolute value of the resulting current, was substituted instead of $I_1\cdot jX_{m\nu}$ in (50). Then, it would have been taken into account that some attenuation already occurs on slip $s_{b\nu}$, instead of no attenuation on slip $s_\nu=0$.

The rate of reduction is also illustrated by Figure 4 although it was developed for $\eta_{2\nu}^2$. If skewed by one rotor slot pitch then $\chi_{2\nu}^2=\eta_{2\nu}^2$ and the ratio in Figure 4. corresponds to $\chi_{2\nu}^2$; if skewed by one stator slot pitch, then approximately by that amount.

Skewing of the rotor slot effectively reduces the asynchronous parasitic torque, as it was invented just for this purpose. The comment on Figure 13 is now also confirmed by the formulas. From the comparison of (15) and (51) comes out that the slot skew affects the synchronous parasitic torque and the asynchronous parasitic torque in different manner: it reduces the former linearly, the latter by its square: corresponding to the difference in their physics. Another difference is that (in the case of $Z_2>Z_1$) the critical harmonics in both cases do not necessarily coincide because they are independent from each other.

Skewing the rotor slot significantly reduces the response of the rotor to all stator harmonics in this way except fundamental harmonic. Therefore, in skewed machines, there is another reason to calculate the rotor harmonics created only by the fundamental harmonic stator MMF when calculating the synchronous parasitic torque and radial magnetic force waves. However, they must be taken into account in their original value in the role of ν_b because the harmonic attenuation of all stator harmonics is naturally greatly reduced and practically eliminated.

10. Effect of Rotor Slot Skewing on the Attenuation of Stator Differential Leakage

Attenuation is related to the asynchronous parasitic torque; therefore, they must be treated together as it was done in [9].

It is observed in the previous chapter that the harmonic current has decreased as a result of skewing, so the stator differential leakage will be attenuated to a lesser extent. Complete attenuation factor [12] (269)

$$\Delta_\nu = 1 - \chi_{2\nu}^2\eta_{2\nu}^2 \tag{52}$$

came closer to 1.

In this way, the differential leakage is attenuated by

$$\sum_{\nu\neq1}^{2mq_1+1}\chi_{2\nu}^2\eta_{2\nu}^2\frac{1}{\nu^2}\frac{\xi_\nu^2}{\xi_1^2}X_m \tag{53}$$

This implies that this value will be smaller. Therefore, the elements of differential leakage affected by attenuation must be calculated according to

$$\sum_{\nu\neq1}^{2mq_1+1}\frac{1-\chi_{2\nu}^2\eta_{2\nu}^2}{\nu^2}\frac{\xi_\nu^2}{\xi_1^2}X_m \tag{54}$$

After rearranging, we arrive at the definition of the attenuation factor, acc. to Richter [12]:

$$\Delta = 1 - \frac{1}{\sigma_1}\sum_{\nu\neq1}^{2mq_1+1}\chi_{2\nu}^2\eta_{2\nu}^2\frac{1}{\nu^2}\frac{\xi_\nu^2}{\xi_1^2} \tag{55}$$

where as definition

$$\sigma_1 = \sum_{\nu\neq1}^{\infty}\frac{1}{\nu^2}\frac{\xi_\nu^2}{\xi_1^2}$$

In [9], we calculated the attenuation factors for the often-used slot numbers, taking also chording into account; the latter was missing in the literature until then. Now, we also consider the effect of skew, for different chording, in Figure 15. The characteristic curves calculated in [9] are repeated, and then the new curves are added next to them to facilitate the comparison.

As expected, the figures show that the attenuation values came very close to 1, especially when $q_2'<q_1$. In these cases, a value of $\Delta=1$ can be assumed, which means that there is no attenuation, the original, unchanged value of the stator differential leakage must be considered. If $q_2'>q_1$, the characteristic curve provides precise guidance on the attenuation to be considered. If $q_1\geq4$, slot skewing has practically no influence.

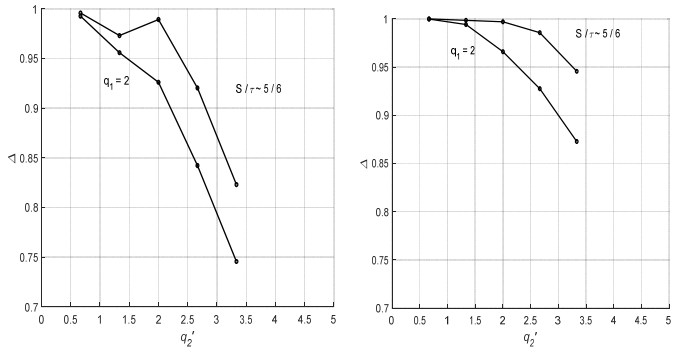

Figure 15a: Characteristic of Δ attenuation factors acc. to Richter ([12], p. 155. Figure 108) modified by the Author, for $q_1=2$, with no chording and with a chording of S/τ~5/6 , with no skewing, with skewing by one rotor slot pitch

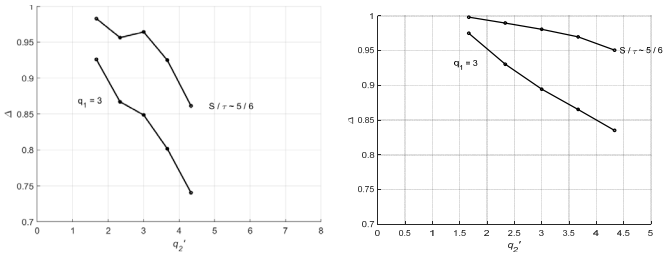

Figure 15 b: Characteristic of Δ attenuation factors acc. to Richter ([12], p. 155. Figure 108) modified by the Author, for q_1=3, with no chording and with a chording of S/τ~5/6 , with no skewing, with skewing by one rotor slot pitch

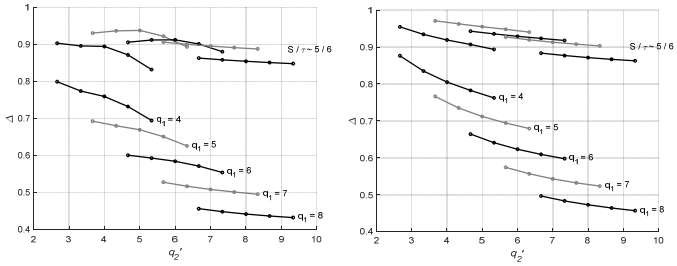

Figure15.c: Characteristic of Δ attenuation factors acc. to Richter ([12], p. 155. Figure 108) modified by the Author, for q_1=4-8, with no chording and with a chording of S/τ~5/6 , with no skewing, with skewing by one rotor slot pitch

11. High Voltage Stator Winding with Open Slots

The formula for the MMF harmonics generated by the stator winding and their winding factor is valid for the theoretical machine with no slots on the stator and rotor, with the conductors of infinitely small width so the slot opening was not taken into account. However, the high-voltage winding is placed in open slots according to standard technology. The circumferential change of the MMF along the slot opening is not stepwise anymore as it is shown in Figure 16.

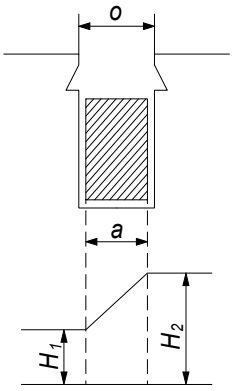

Figure 16: Sketch for the MMF of a conductor with a finite width along the slot opening ([15] Figure 19, p. 46)

Similar conditions also develop in the case of strong saturation of the tooth head.

The width of the slot depends on the design of the machine, within which the width of the copper wire depends on the voltage level and the resulting insulation thickness. From the point of view of the present investigation, it is considered a good general approximation if the width of the conductor is taken as 1/3 of the stator slot pitch. Figure 17 shows the resulting MMF curve for q_1=2 and q_1=3.

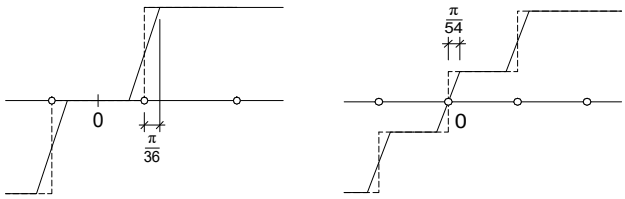

Figure 17: Image of MMF of one phase for q_1=2 and q_1=3

The figure is identical to the MMF generated in the case of a stator slot skew of 1/3 stator slot pitch; therefore, a high-voltage stator in itself is equivalent to a stator slot skew of this magnitude.

About the phenomenon, Jordan proved how it reduces the differential leakage; the result is described in [15]. Differential leakage is a general, cumulative quantity. Here, however, we cannot be satisfied with the general evaluation, since the effect on the synchronous torques and on the noise components must be precisely determined one by one. Therefore, the considerations of Chapter 4. must be applied, which requires the analysis of Figure 17.

Figure 17, on the other hand, does not correspond to Figure 9, therefore (11) is not valid. The arrangement can only be examined with a full Fourier analysis. Based on the figure, it is expected that the arrangement corresponding to such a small amount of skew will not have a perceivable influence on the behavior of the machine; however, this will only be partially true. The investigation provides the following result see Table 4.

Table 4: Stator Harmonics in High-Voltage Motors

q_1	2	3
harmonic ν	magnitude of harmonic	
5-7	0,24	0,19
11-13	0,80	0,18
17-19	0,17	0,80
23-25	0,42	0,15
29-31	≈0	≈0
35-37	≈0	0,40
41-43	≈0	≈0
47-49	0,20	≈0
53-55	≈0	≈0
59-61	0,2	≈0
65-67	≈0	≈0
71-73	≈0	0,2

Evaluation of it is as follows:

- in order to evaluate the results, the calculated values shall be compared with the winding factor for the respective harmonic. The reason for this is that the values are not reducing factors, but residual values. It can be seen that there is no perceptible change up to the 2nd slot harmonic, which is then reduced by half. The higher harmonics are significantly reduced even by such a small skewing. Still, the design engineer does the right thing if he ignores the effect of open slots in the vast majority of cases.

- it was already shown in [11] III. F that harmonics of higher order, depending on the size of the air gap, do not play a role from the point of view of subject examination. Table 4 shows further that for machines with open stator slots, even the harmonics with

order number higher than 2nd slot harmonic have no role except slot harmonics, but they also appear only strongly reduced. This means that in high voltage motors much less harmonics shall be considered as in low voltage ones.

- based on [11] Table VI. 4 pole, however, it can be seen that there might still be one or two slot numbers that could be used in high-voltage machines, such as the Z_1/Z_2=24/32 slot number; it is a so called "of 2/3q" rotor slot number, the dangerous highest torque occurs in brake range, the second high torque in motoric range is acceptable, the high stillstand torque is caused by high order harmonics, therefore, it is fairly reduced by open stator slot

- at this point the variation in magnetic conductivity of the airgap cannot remain out of consideration; [10] provides detailed guidance in the matter.

12. Summary

In this study, the effect of the skew of the rotor slot on the parasitic torques of a squirrel-cage induction motor was examined through analytical method. It was established that the generally accepted physical explanation for this phenomenon is incomplete and therefore misleading it does not cover the complete physical truth.

Here, the complete physic was studied; a clear distinction was made between the physics of the effect of skewing on synchronous and asynchronous parasitic torques. Further, a clear distinction was made between the physics of stator slot skew and rotor slot skew. The explanation of rotor slot skew regarding synchronous parasitic torque is: the skewing reduces the harmonics of the fundamental harmonic current of the rotor, thereby reducing the synchronous parasitic torque. A modified theorem defining the creation of synchronous parasitic torques is proposed. The calculation was based on comparing the stepped MMF curve of the straight rotor slot and the trapezoidal MMF curve of the skewed slot. By setting the harmonic content of the two curves in proportion, a new formula was provided.

A new basic theorem was formulated: the magnitude of the residual synchronous parasitic torque due to skewing by one stator slot pitch is always the same, being independent from the magnitude before skewing, from the slot number combination and from the winding factor of the stator harmonic creating the torque; it is independent from whether the skew is performed on the stator or on the rotor; it depends only from the order number of the actual harmonic: all of these are proven by formula.

The degree of skewing on the rotor is not determined a priori, as it was thought until now, but can be applied on a targeted manner with regard to the dangerous harmonic torque; another theorem was formulated on when to skew according to the stator and when acc. to the rotor slot pitch or with other pitch. Further, the theorem was supplemented in case of synchronous parasitic torque in rotation: the skewing may be done acc. to critical harmonic in order to achieve mathematical zero result. With this theorem, the explanation of the effect exclusively by the stator slot harmonic as well as preforming the skewing exclusively by one stator slot pitch is exceeded.

It was proved in [10] at the first time that the synchronous parasitic torque and radial magnetic force can be transferred to each other; that is, the results can also be used in noise reduction. It is a task for further research to investigate the distinct effect of skew on the noise because the topic is generally not researched in sufficient depth.

A new formula is provided for the calculation of effect on the asynchronous parasitic torque, too. The slot skew affects the synchronous parasitic torque and the asynchronous parasitic torque in different manner: the skew factor reduces the former linearly, the latter stronger, by its square.

The effect of the skewing on the stator differential leakage was thoroughly calculated for a wide range corresponding to practice. The differential leakage is (much) less attenuated in a skewed slot machine.

Based on its physics also the open stator slot of a high-voltage machine belongs to this topic, there are one or two slot numbers that might become usable in high-voltage machines although being forbidden for low voltage ones.

The above summarized results should indicate the direction to be followed for further research in the case of using more advanced methods by including neglected aspects and then performing measurements.

The contribution of this study is that analytical approach was chosen namely Fourier analysis of the MMF of the skewed machine instead of other methods giving photo-like results only. The paper revealed the basic laws of skewing, this way of analysis made it possible to discover key theorems.

The conclusion is that the design engineer should not apply rotor slot skewing always on the same way but purposefully, on a targeted manner; with torque in rotation, he can completely eliminate (mathematical zero) the critical torque and noise component. Reduction of breakdown torque, however, as "price to be paid" for the advantages need to be considered as it has been done so far.

With present study, the entire scope of the topic is covered.

13. Appendix

13.1 MMF harmonics

The basic formulas for the order number of space harmonics:

$$\nu_a = 6g_1 + 1 \quad (56a)$$

$$\mu_a = e\cdot Z_2/p + \nu_a = e\cdot 2mq_2' + \nu_a \quad (56b)$$

$$\nu_b = 6g_2 + 1 \quad (57)$$

The rotor harmonics generated by the fundamental harmonic:

$$\nu_a = 1 \qquad \mu_a = e\cdot Z_2/p + 1 = e\cdot 2mq_2' + 1 \quad (58)$$

The harmonics of the stator MMF called here ν_b are considered now for q_1 =2, together with the response of the rotor

ν_b= -5 $0<\eta_{2,-5}^2<1$

ν_b= 7 $0<\eta_{2,7}^2< 1$

ν_b= -11 $\eta_{2,-11}^2 \approx 0$

ν_b= 13 $\eta_{2,13}^2 \approx 0$

The magnitude of these harmonic fields is attenuated due to response of the rotor by the Δ_ν rotor attenuation factor [12] (269) p. 154:

$\nu_b=$	-5	ξ_5	$\xi_5 \cdot \Delta_5 = \xi_5 \cdot (1- \eta_{2,-5}^2)$
$\nu_b=$	7	ξ_7	$\xi_7 \cdot \Delta_7 = \xi_7 \cdot (1- \eta_{2,7}^2)$
$\nu_b=$	-11	$\xi_{11} = \xi_1$	$\xi_{11} \cdot \Delta_{11} = \xi_{11} \cdot (1- \eta_{2,-11}^2)$ $(= \xi_1)$
$\nu_b=$	13	$\xi_{13} = \xi_1$	$\xi_{13} \cdot \Delta_{13} = \xi_{13} \cdot (1- \eta_{2,13}^2)$ $(= \xi_1)$

The apparent winding factor of the slot harmonics remains the same, as it generates a very small current in the rotor to attenuate it.

The stator harmonics (56a) and (57), which are both numerically and physically *identical*, are called ν_a or ν_b according to their roles.

13.2 Synchronous parasitic torques in standstill

The synchronous parasitic torque generated in standstill is created by the difference between the torques generated by two *adjacent* harmonics. However, they add up if the two torques have different signs. For this, it is necessary that the winding factors of the two (adjacent) harmonics have the same sign: this condition is only fulfilled in the case of slot harmonics. In other words, a significant torque in standstill is generated only with the contribution of the (stator) slot harmonic; otherwise that torque is practically zero. The torque is therefore significant for two reasons: because both of them are created by slot harmonics and then they are summed up. Only slot skew with a stator slot pitch protects against these; but since it should protect against two different torques at the same time, the resulting torque cannot be mathematically zero (see end of Chapter 7).

Acknowledgment: The author gratefully acknowledges the contributions of István Laczkó, Chief Engineer of the United Electric Machine Factory, EVIG, Budapest, Hungary, for his valuable comments.

Conflicts of Interest: "The author declares no conflicts of interest."

References

[1] Lang Wang, Xiaohua Bao, Chong Di, Yang Zhou, Qinfen Lu, "Analysis of synchronous parasitic torque in dual skew cage rotor induction motors with equivalent slot number", IET Electr. Power Appl., 11(**8**), 1357-1365, 2017 DOI: 10.1049/iet-epa.2016.0565 www.ietdl.org

[2] G. Joksimović, A. Kajević, S. Mujović, T. Dlabač, V. Ambrožič, A. Tessarolo, "Rotor bars skewing impact on electromagnetic pulsations in cage induction motor", Proc. IcETRAN, 292-296, 2019.

[3] C. Guérin, R. Ruiz, Y. Le Floch, P. Lombard, M. Vilcot, J.P. Ducreux, A. Abakar, L. Sadi-haddad, "Two Techniques for Modeling an Induction Motor with Skewed Slots with a TimeStepping 2D-3D Finite Element Method", IEEE International Conference on Electric Machines and Drives, 2005. DOI: 10.1109/IEMDC.2005.195845

[4] B. Asad, T. Vaimann, A. Belahcen, A. Kallaste, A. Rassolkin, H. van Khang, P. S. Ghahfarokhi, M. U. Naseer, M. Iqbal, "The Modeling and Investigation of Slot Skews and Supply Imbalance on the Development of Principal Slotting Harmonics in Squirrel Cage Induction Machine, DOI 10.1109/ACCESS.2021.3134331

[5] Carbonieri, M.; Bianchi, N. "A Complete and Fast Analysis Procedure for Three-Phase Induction Motors Using Finite Element, Considering Skewing and Iron Losses". Appl. Sci. 2021, 11, 2428. DOI:10.1109/IEMDC.2019.8785364

[6] R. Pile, E. Devillers, Z. Zahar, J. Besnerais, "Fast Calculation of Electromagnetic Vibrations Induced by Longitudinally Varying Excitations in Skewed Electrical Machine", ICEM 2022, Valencia, Spain, DOI: 10.1109/ICEM51905.2022.9910809

[7] K. Gyftakis, J. Kappatou, "A new technique for the skewing consideration in the 2-D FEM un-skewed induction motor time-dependant electromagnetic characteristics" 2016 19th International Conference on Electrical Machines and Systems (ICEMS), 2016.

[8] G. Joksimovic, M. Durovic, A. Obradovic: "Skew and linear rise of MMF across slot modeling – winding function approach", IEEE Transactions on Energy Conversion, 14(**3**), September 1999 DOI: 10.1109/60.790876

[9] G. Kovács: "Harmonics in the Squirrel Cage Induction Motor; Analytic Calculation; Part I.: Differential Leakage, Attenuation and Asynchronous Parasitic Torques". CES (China Electrotechnical Society) Transactions on Electrical Machines and Systems, 7(**3**), 320-329, 2023, DOI 10.30941/CESTEMS.2023.00034

[10] G. Kovács: "Harmonics in the Squirrel Cage Induction Motor; Analytic Calculation; Part II.: Synchronous Parasitic Torques, Radial Magnetic Forces". CES (China Electrotechnical Society) Transactions on Electrical Machines and Systems, 7(**4**), 404-421, 2023, DOI 10.30941/CESTEMS.2023.00035

[11] G. Kovács, "Harmonics in the Squirrel Cage Induction Motor; Analytic Calculation; Part III.: Influence on the Torque-Speed Characteristic", CES (China Electrotechnical Society) Transactions on Electrical Machines and Systems, 8(1), 86 - 102, March 2024, DOI: 10.30941/CESTEMS.2024.00006

[12] Richter, R.: Elektrische Machinen, Vierter Band, Die Induktionsmaschine, Springer Verlag 1936., 1950.

[13] Liska J.: Villamos gépek III. Szinkron gépek. (in Hungarian) Tankönyvkiadó, Budapest, 1966

[14] Liska J.: Villamos gépek IV. Aszinkron gépek. (in Hungarian) Tankönyvkiadó, Budapest, 1960

[15] Heller, B., Hamata, V.: „Harmonic Field Effects in Induction Machines" ELSEVIER Scientific Publishing Company Amsterdam, Oxford, New York 1977

[16] Möller, H.: „Über die Drehmomente beim Anlauf von Drehstrommotoren mit Käfigankern". Archiv für Elektrotechnik 1930. p. 400-424. https://katalog.slub-dresden.de/en/id/0-1161496939

ASTES

Advances in Science, Technology and Engineering Systems Journal
Vol. 10, No. 1, 37-47 (2025)
www.astesj.com
Special Issue on Innovation in Computing, Engineering Science & Technology

ASTES Journal
ISSN: 2415-6698

Hardware and Secure Implementation of Enhanced ZUC Steam Cipher Based on Chaotic Dynamic S-Box

Mahdi Madani*[,1], El-Bay Bourennane[1], Safwan El Assad[2]

[1]*Laboratoire ImViA (EA 7535) , Université Bourgogne Europe, 21000 Dijon, France*

[2]*IETR , University of Nantes/Polytech Nantes, France*

ARTICLE INFO

Article history:
Received: 14 October, 2024
Revised: 05 January, 2025
Accepted: 06 January, 2025
Online: 04 February, 2025

Keywords:
Dynamic S-box
FPGA design
Hardware metrics
ZUC stream cipher
Mobile security
Cryptography
Cryptanalysis

ABSTRACT

Despite the development of the Internet and wired networks such as fiber optics, mobile networks remain the most used thanks to the mobility they offer to the user. However, data protection in these networks is more complex because of the radio channels they use for transmission. Hence, there is a need to find more sophisticated data protection means to face any attack. But, this is not an easy task, especially with the emergence of AI-based attacks. In this context, we proposed in this work a solution that can significantly improve data protection in a new-generation mobile network. Therefore, the main objective of this study is to improve and implement an enhanced version of the standard ZUC algorithm designed by the Data Assurance and Communication Security Research Center of the Chinese Academy of Sciences and standardized by the 3GPP (3rd Generation Partnership Project) organization to ensure the LTE (Long Term Evolution of radio networks) security. The proposed design is principally based on replacing the static S-boxes of the original algorithm (S_0 and S_1) with a chaos-based dynamic S-boxes thus allowing to generate a different key-stream for any change on the secret key and with the best randomness and robustness properties. The two new dynamic S-boxes are initialized with 256 initialization values each (x"00"), then filled in parallel using two chaotic maps that use the ZUC algorithm registers, the CK (Cipher Key), and the IV (Initial Vector) to form two different initial values for each chaotic map. To reach the hardware performance, we implemented the system on a Xilinx XC7Z020 PYNQ-Z2 FPGA platform. The designed architecture occupies low logic resources (1135 Slice LUTs, 762 Slice Registers, and 8 DSP48E1) on the used FPGA device and can reach a throughput of 2515.84 Mbps with a running frequency of 78.62 Mhz by consuming only 0.188 W. To evaluate the resistance of the proposed cryptosystem, we used many security tests (keystream distribution, keystream randomness, key sensitivity, plaintext sensitivity, keyspace, and NIST statistical tests). The experimental results and comparison with other S-boxes based algorithms prove on one hand that using the dynamic S-box technique has enforced considerable data protection against cryptanalysis attacks, and on another that the hardware metrics (used logic resources, achieved throughput, and efficiency) are suitable for real-time applications such as mobile security transmission.

1. Introduction

Despite the development of high throughput Internet based fiber optics, mobile and connected objects networks remain the most used thanks to the mobility and ease they offer to the user. The main component they use is the smartphone which facilitates access to most of our daily services such as video calls, social network messaging, e-payment, smart-home, smart-city, etc.

However, data protection in these networks is more complex due to the physically unprotected radio channels they use for communications.

Hence, it is necessary to find more sophisticated means of data protection to deal with any attacker trying to illegally access data by going directly to the storage location (mainly servers or cloud) or by capturing encrypted data and trying to decrypt it by cracking the encryption algorithm used or looking for the secret key.

Therefore, protecting personal and sensitive information (naturally circulates on the physically unprotected radio transmission

*Corresponding Author: Mahdi Madani, Laboratoire ImViA, Université Bourgogne Europe, 21000 Dijon, France & Mahdi.Madani@u-bourgogne.fr

channel) is not an easy task, especially with the emergence of AI-based (Artificial Intelligence) attacks. This is why a cryptographic algorithm with the best robustness and resistance against computer attacks is needed to success this task. Since many decades, different cryptosystems have been designed as: block ciphers: DES (Data Encryption Standard), AES (Advanced Encryption Standard), KASUMI; stream ciphers: RC4 (Rivest Cipher 4), SNOW-3G, ZUC; hashing functions: DSA (Digital Signature Algorithm), Secure Hash Algorithms SHA-0, SHA-1, SHA-2, SHA-3; chaotic systems: Lorenz, Chen, logistic map, skew tent map, and other methods.

In this study, we evaluate the security performance of the ZUC stream cipher which is designed by the Data Assurance and Communication Security Research Center of the Chinese Academy of Sciences and standardized by the 3GPP (3rd Generation Partnership Project) organization to ensure the LTE (Long Term Evolution of radio networks) security. ZUC algorithm forms also the kernel of the confidentiality (128-EEA3) and integrity (128-EIA3) functions used in the LTE networks security [1, 2]. In addition, we propose an enhanced version that can significantly improve data protection in a new-generation of mobile network.

We started by analyzing the internal architecture of the original ZUC algorithm is based on three main layers, LFSR (Linear Feedback Shift Register), the BR (Bit Reorganization), and the NLF (Non Linear Function) [3]. The state of the art has proven that the ZUC architecture has certain weaknesses that require immediate improvements [4, 5, 6, 7, 8].

To remedy the identified problems, we improved the non linearity part of the standard algorithm by replacing its two static S-boxes (S_0 and S_1) with a chaos-based dynamic S-boxes [9, 10, 11, 12]. The new version allows the generation of different key-streams for any change on the secret key with the best randomness and robustness properties that increase the complexity of cryptanalysis attacks.

This paper is principally based on extending our work initially presented at the ICEET23 conference and improving the performance of the implemented architecture. Therefore, we can summarize the two main contributions of this extended version on: Firstly, we used a chaotic map to generate dynamically the internal two S-boxes (S_0 and S_1) of the ZUC algorithm. The experimental analysis show the respect of the generated S-boxes to the non-linearity recommendations. Secondly, we designed an optimized FPGA implementation with the best hardware metrics. A comparative study with the literature is given to confirm our results on the two listed steps. The proposed architecture consists of using two parallel chaotic maps to generate two dynamic S-boxes SD_0 and SD_1. They are dynamic because the chaotic maps are initialized using control parameters derived from the combination of the CK, the IV, and the internal registers (S_{15}, S_{14}, S_5, and S_7) of the LFSR layer. This technique ensures that any change (one bit is enough) in these three parameters will result in a different S-boxes. Many examples of generated S-boxes are examined using known theoretical tests for similar analysis, and the results are conclusive, unlike the original work which failed some tests.

To reach the hardware implementation, the proposed architecture is coded using a VHSIC Hardware Description Language (VHDL) and implemented on Field-Programmable Gate Array (FPGA) technology [13, 14] to explore its offered parallel calculations capabilities and the low power consumption.

The implementation on a Xilinx XC7Z020 PYNQ-Z2 FPGA hardware platform achieves a throughput of 767.52Mbps at an operating frequency of 94.34 Mhz. The robustness of the proposed architecture is evaluated using the keystream performance: analyzing the uniformity (histogram, chi square), randomness, key sensitivity, plaintext sensitivity, examining the key space complexity, and investigating the NIST (National Institute of Standards and Technology) statistical tests [15].

The experimental results prove on one hand that using the dynamic S-boxes technique has enforced considerable data protection against cryptanalysis attacks, and on another that the hardware metrics (used logic resources, achieved throughput, and efficiency) are suitable for real-time applications such as mobile security transmission.

The reminder of this paper is organized as follows. Section 2 summarize the internal architecture and the processing steps of the regular ZUC stream cipher in its two operating modes. Section 3 describes the proposed architecture including the chaos-based dynamic S-boxes designed to enhance the security and enforce the resistance of the standard algorithm face to attacks. Section 4 presents the FPGA implementation results in terms of the occupied hardware metrics (logic resources, FFs, BRAMs) and the achieved timing metrics (throughput, frequency, efficiency). It also shows the behavioral simulation results under Vivado tools to prove the best functionality of our design. Section 5 investigates cryptanalytic analysis and stream cipher performance allowing to prove the robustness of the proposed scheme. Finally, section 6 summarizes the whole article and gives directions for our perspectives in the future.

2. Original ZUC stream cipher overview

As we already discussed, ZUC algorithm is a word-oriented stream cipher designed by the Data Assurance and Communication Security Research Center of the Chinese Academy of Sciences and standardized by the 3GPP organization to ensure the LTE and 5G (the fifth generation of cellular network technology) security. In this section, we present briefly its internal architecture, its processing steps in the two operating modes, and some attacks from the literature that subjected the standardized version.

ZUC is a word-oriented algorithm that generates a 32-bits word key-stream under the control of a 128-bits CK and 128-bits IV [3, 16, 17]. Its internal architecture is formed by three main interacting layers corresponding to the LFSR, the BR, and the NLF layers, respectively. The LFSR layer is formed by 16 stages of 31-bits registers ($S_0, S_1, \ldots, S_{15}$). The BR layer is composed of 4 stages of 32-bits registers (X_0, X_1, X_2, X_3) filled from the LFSR layer ($S_{15}, S_{14}, S_{11}, S_9, S_7, S_5, S_2, S_0$). The NLF layer is made up of 2 S-boxes (S_O, S_1) and 2 intermediate 32-bits registers (R_1, R_2) sequentially updated based on the output of the BR layer.

The ZUC stream cipher runs in two operating modes to generate a valid output, initialization and key-stream, as described below.

- Initialization mode: consist of loading the control parameters (CK and IV) to initiate the internal states of the LFSR registers according to the following Formula.

$$\begin{cases} S_0 = CK(127:120)||1000100110101111||IV(127:120) \\ S_1 = CK(119:112)||0100110101111100||IV(119:112) \\ S_2 = CK(111:104)||1100010011010111||IV(111:104) \\ S_3 = CK(103:96)||0010011010111110||IV(103:96) \\ S_4 = CK(95:88)||1010111100010011||IV(95:88) \\ S_5 = CK(87:80)||0110101111000100||IV(87:80) \\ S_6 = CK(79:72)||1110001001101011||IV(79:72) \\ S_7 = CK(71:64)||0001001101011111||IV(71:64) \\ S_8 = CK(63:56)||1001101011110000||IV(63:56) \\ S_9 = CK(55:48)||0101111000100111||IV(55:48) \\ S_{10} = CK(47:40)||1101011110001001||IV(47:40) \\ S_{11} = CK(39:32)||0011010111100011||IV(39:32) \\ S_{12} = CK(31:24)||1011110001001101||IV(31:24) \\ S_{13} = CK(23:16)||0111100010011011||IV(23:16) \\ S_{14} = CK(15:8)||1111000100110101||IV(15:8) \\ S_{15} = CK(7:0)||1000111101011001||IV(7:0) \end{cases}$$

Then, combining the output of the NLF layer (W), a primitive polynomial over the Galois Gield $GF(2^{31}-1)$, and a modulo operations [3] to updates the register S_{15} according to Equation 1.

$$\begin{cases} u = W >> 1 \\ v = 2^{15}S_{15} + 2^{17}S_{13} + 2^{21}S_{10} + 2^{20}S_4 \\ \quad +(1+2^8)S_0 \ \ mod\ (2^{31}-1) \\ Fb = (v+u) \ \ mod\ (2^{31}-1) \end{cases} \quad (1)$$

In addition, the remainder registers are right shifted to update the LFSR layer, as follows.

$$\begin{cases} S_{15} = Fb \\ S_{14} = S_{15} \\ S_{13} = S_{14} \\ \cdots \\ S_0 = S_1 \end{cases}$$

This mode is executed for 32 clock cycles without generating output sequence Z, as illustrated in Figure 1.

- Key-stream mode: consist of using the outputs of the NLF (W) and the BR (X_3) layers to generate a 32-bits output key-stream word (Z) at each clock cycle according to Equation 2.

$$Z = W \oplus X_3 \quad (2)$$

The processing of this operating mode is illustrated in Figure 2.

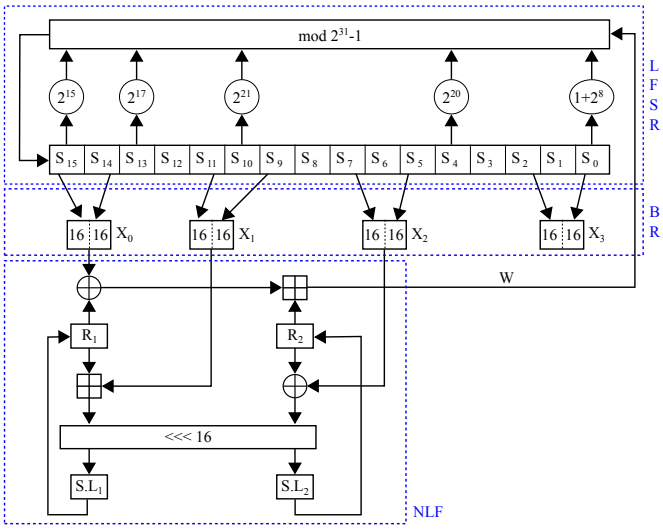

Figure 1: ZUC stream cipher initialization mode.

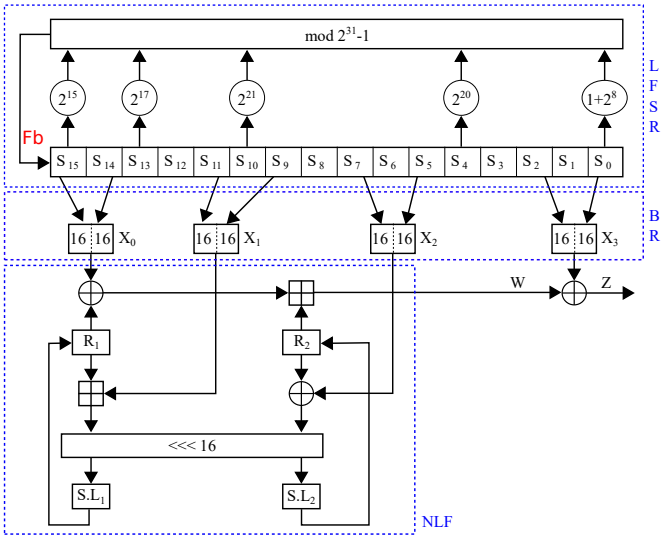

Figure 2: ZUC stream cipher key-stream mode.

Since its inception, the robustness of the ZUC stream cipher has been analyzed and the algorithm has suffered numerous attacks. In the literature several works have identified some drawbacks. Among them, we cite the alternative algebraic analysis [4], differential attacks[5], satisfiability solvers based analysis [6], and NIST statistical analysis [8, 7, 18, 19].

To overcome these weaknesses, we proposed a solution in this work based on enhancing the nonlinear part of the algorithm to resist cryptanalysis attacks. In the following sections, we will detail the technique used and give the results proving the improvement.

3. Proposed chaos-based architecture

In this section, we present the proposed architecture focused on improving security resistance against cryptographic attacks. The

adopted technique is based on the use of a chaos-based dynamic S-boxes by the NLF layer, unlike the original one using two static S-boxes S_0 and S_1.

3.1. Chaotic dynamic S-box implementation

S-boxes known as lookup tables are a non linear functions widely used by cryptographic algorithms. They are defined to ensure no repetition and to generate a non-linear output value [9, 10, 11]. However, if the CK used is cracked, the entire security of the algorithm will be compromised and the encrypted data will be exposed. To overcome this issue, we designed a dynamic chaotic S-box that ensures that even if the internal architecture of the algorithm and the CK are compromised, only modifying the CK will provide good data protection in the future. This will be guaranteed by the chaos map control parameters which change with every small modification in the CK and IV mobile client parameters ensuring a good confusion properties of the NLF layer and generating a random output key-stream.

Basically, ZUC stream cipher runs on two operating modes (initialization and key-stream modes) using two static S-boxes S_0 and S_1. However, the proposed design uses two chaos-based dynamic S-box.

We began initializing the internal LFSR, BR, and NLF layers, like the standard algorithm. The only difference is the replacement of the standard S-boxes (S_0 and S_1) by two new dynamic S-boxes (SD_0 and SD_1) of the same length (16×16) but with internal values initialized to zero at this step. In parallel, we set two logistic chaotic maps using different initial conditions extracted from the BR layer (driven from the control parameters CK and IV) according the Formulas 3 and 4.

$$DK_1 = X0(31\ downto\ 16) \parallel X2(15\ downto\ 0) \tag{3}$$

$$DK_2 = X0(15\ downto\ 0) \parallel X2(31\ downto\ 16) \tag{4}$$

Note that DK_0 and DK_1 form the dynamic keys of the chaotic system, $X0$ and $X2$ are registers from the BR layer, and $\parallel$ is the concatenation operator.

After initializing the chaotic system based on two Logistic maps (non-linear chaotic discrete function), it produces two 32-bits random sequences. The first sequence will be used to complete the dynamic S-box SD_0 and the second sequence to complete the S-box SD_1. The mathematical model of the discrete logistic map is defined by Equation 5.

$$X_{n+1} = \begin{cases} \dfrac{X_n \times (2^N - X_n)}{2^{N-2}} & if\ X_n \neq [3 \times 2^{N-2}, 2^N] \\ 2^N - 1 & if\ X_n = [3 \times 2^{N-2}, 2^N] \end{cases} \tag{5}$$

Where X_{n+1} is the new value calculated from the previous one X_n, N is the output size of the discrete logistic map (N=32-bit).

To fill one S-box, we run the chaotic system that generates 32-bit key-stream words at each clock cycle. We take 8-bits to fill one of the 256 available cells. To avoid repetition, we used a control vector of the same size ($16 \times 16 = 256$) based on a repetition flag set to zero. The principle consists of saving the value (x) on the S-box (at position [i, j], i, j = 0 to 15) and setting the corresponding flag to one (flag [x] = 1). This ensures that If the value is generated again during the filling process, it will be ignored. The block diagram of the algorithm is shown in Figure 3.

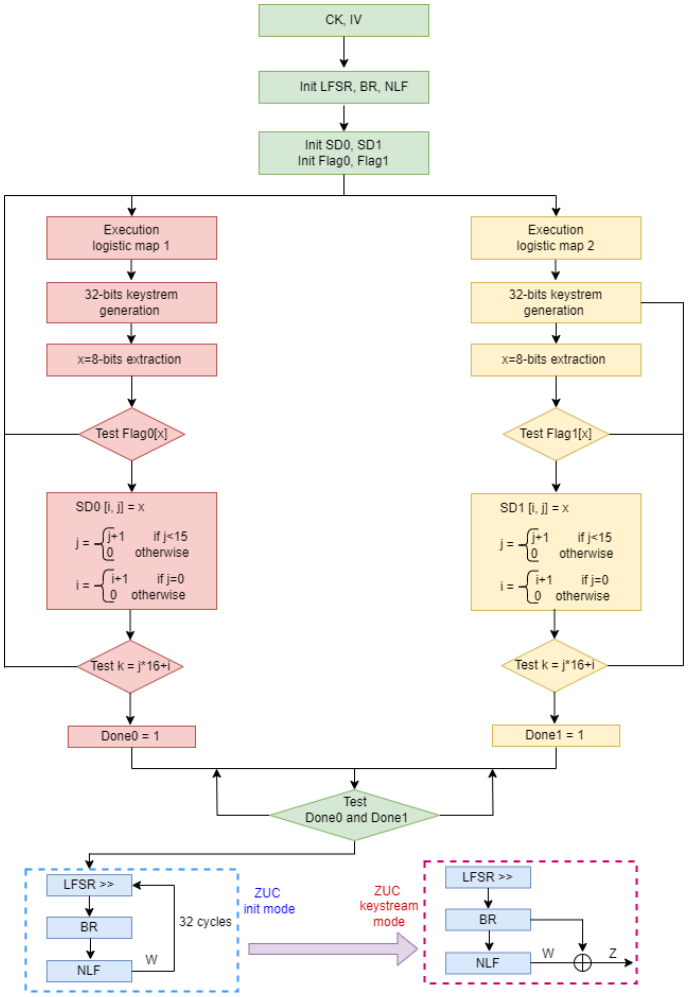

Figure 3: S-boxes generation procedure.

To complete the second S-box in parallel, we used the same principle. Initializing the chaotic maps with different keys ($DK_1 \neq DK_2$) guarantees the generation of two distinct S-boxes. This technique allows the completion of the two dynamic S-boxes without repetition by respecting the principle of creating lookup tables.

After completing both the S-boxes, the proposed ZUC stream cipher will be executed similarly to the original one, with 32 cycles running the initialization mode and then the key-stream mode for the remainder but using the proposed dynamic S-boxes, as explained above. For more clarity, we illustrate the architecture of the proposed design in Figure 4.

3.2. S-box analysis

The security of algorithms using on S-box is principally based on this non-linear component. Therefore, any weakness or problem in its construction will significantly affect the whole security of the algorithm and weaken its resistance to attacks such as linear and

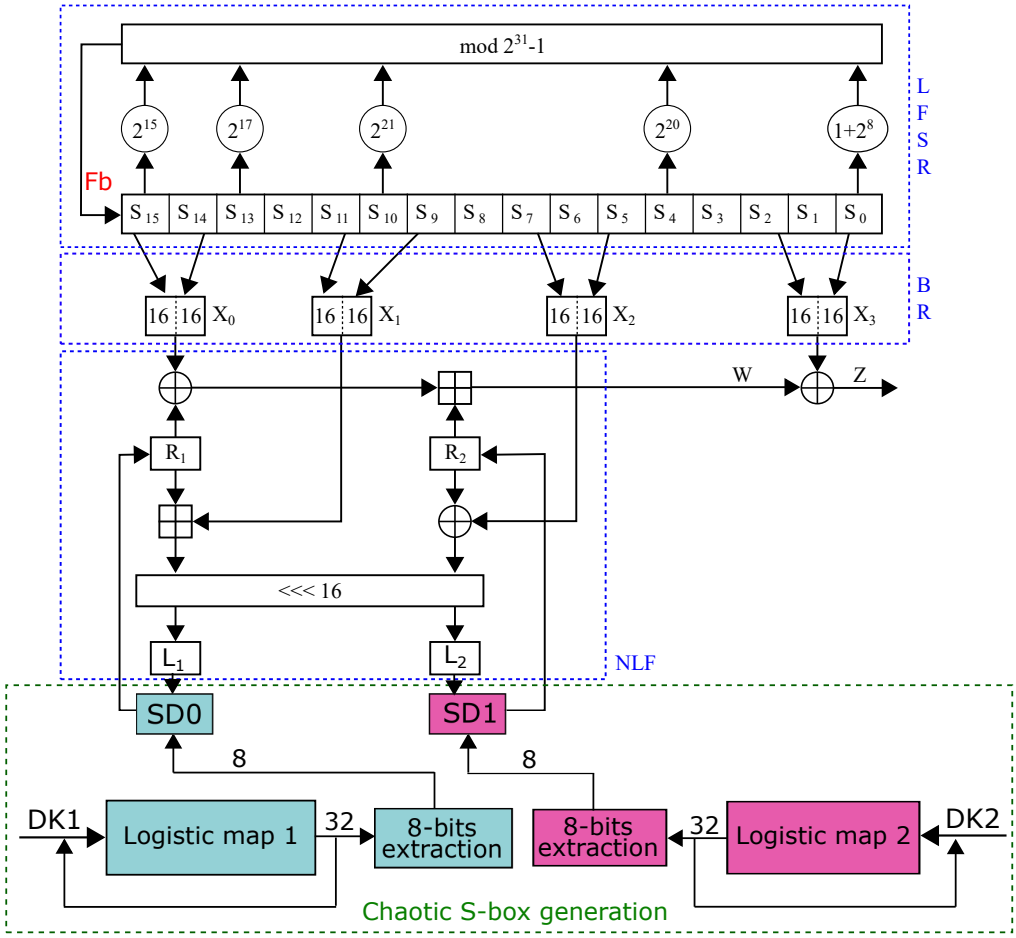

Figure 4: Proposed ZUC with dynamic S-boxes architecture.

differential cryptanalysis. For this, we evaluate the main performances of the proposed dynamic S-box to avoid any unpleasant surprises. To prove the expected high level S-box, we analyzed its satisfactory to the following criteria: bijection, strict avalanche criterion (SAC), non-linearity, output bits independence criterion (BIC), equiprobable input/output XOR distribution, differential approximation probability (DP), and maximum expected linear probability (LP).

To facilitate understanding the analysis, we present in Table 1 a example of a generated S-box using the proposed technique. So, the analysis study in this section will be based on this sample. In Table 2 we give a comparative study with the literature works based on the mentioned criteria.

3.2.1. Bijectivity and non-linearity

The bijective property of an $N \times N$ constructed S-box is respected if there is no repetition of its values in the interval $[0, 2^N - 1]$. Therefore, as we can see from Table 1, our S-box satisfy this criteria because all its values $[0, 255]$ are different.

According to the S-box non-linearity definition given by [23, 34], our S-box highly non-linear because the minimum non-linearity indicator of 100 when $n = 8$. It is better than all the results presented in Table 2.

3.2.2. SAC criterion

As defined by [35], the SAC criteria is satisfied if changing a single input bit will conduct to change a half of the output bits. To evaluate this parameter in our S-box we used the dependence matrix (see [23]). As we can see from Table 2, the mean (0.4976), value is closed to the optimal value (0.5) and the offset value (0.0156) is closed to zero confirming the satisfaction of the SAC criteria.

3.2.3. Output bits independence criterion

Similarly to SAC, the authors in [35] defined BIC indicating the pair-wise independent for a given vector and its corresponding avalanche (complementing 1 bit). Applying this test to our S-box, we obtained a minimum value of BIC non-linearity (100) and a maximum value of DP (7) ([23, 32]) indicating the satisfaction of the BIC criteria.

3.2.4. Equiprobable input/output XOR distribution

For the analyzed S-box, the high value from the maximum expected differential probability matrix is 12 indicating a few imbalance between the input and output XOR distribution on the S-box.

Table 1: A generated S-box using the proposed technique.

	0	1	2	3	4	5	6	7	8	9	A	B	C	D	E	F
0	57	97	54	116	40	213	98	165	231	50	7	73	37	47	46	216
1	19	136	238	83	71	207	84	95	48	86	100	225	151	162	255	240
2	112	24	27	128	67	227	94	169	13	79	138	203	201	233	214	142
3	150	107	117	120	102	194	206	32	145	247	215	5	224	96	23	141
4	51	16	146	186	241	236	1	110	68	44	121	108	133	235	55	64
5	184	223	125	183	26	153	137	56	171	119	135	88	167	33	242	17
6	70	82	15	191	62	244	45	114	105	25	91	219	161	217	18	3
7	188	124	232	66	199	87	36	198	239	34	185	52	60	9	182	22
8	89	139	21	11	101	77	190	63	179	200	144	29	75	58	10	69
9	28	38	156	178	148	158	218	130	211	209	74	14	123	115	189	80
A	249	93	140	61	35	134	131	4	49	174	76	143	250	42	204	92
B	85	163	221	254	234	196	175	237	129	181	164	39	173	222	170	251
C	65	157	126	245	106	78	210	172	147	31	6	127	230	160	180	30
D	220	195	109	2	253	176	104	53	226	205	192	111	248	118	193	8
E	243	177	20	229	122	90	41	168	99	149	81	59	113	154	228	208
F	252	197	212	152	159	0	155	43	187	12	246	72	202	103	166	132

Table 2: S-box evaluation results and comparison.

S-Box	Min. non-linearity	Mean SAC	SAC offset	BIC-SAC	Min. BIC non-linearity	Max. XOR	LP
Proposed SD	100	0.4976	0.0156	0.4997	100	12	0.0549
AES	112	0.5048	0.02637	0.5046	112	4	0.015625
Madani et al. [20]	-	0.4625	-	0.4969	51.1	-	-
Dridi et al. [21]	102	0.4948	-	0.4991	103.42	10	0.1094
Cavuşoğlu et al [22]	104	0.5039	0.03809	0.5058	98	10	0.0791
Dragan Lambić [23]	106	0.5034	0.02441	0.5014	100	10	0.070557
Alhadawi et al. [24]	106	0.4943	-	0.4982	104.35	10	0.1250
Lai et al. [25]	104	0.5014	-	0.5028	102.75	10	0.1250
Al Solami [26]	106	0.5017	-	0.5026	104	10	0.1094
Xuanping et al. [27]	-	0.4965	-	0.4965	109.36	-	-
Dragan Lambić [28]	108	-	0.02954	-	104	8	0.035156
Liu et al. [29]	104	-	0.03027	-	98	10	0.0625
Guesmi et al. [30]	104	-	0.0293	-	96	10	0.0625
Fatih et al. [31]	100	-	0.03125	-	100	10	0.070557
Guo Chen [32]	102	-	0.03174	-	100	10	0.088135
Lambić et al. [33]	106	-	0.03	-	100	10	0.079

3.2.5. LP property

The LP criteria, as defined in [23, 36, 37] detect any imbalance between the selected input and output bits using two masks a and b. The obtained result after analyzing our S-box is equal to 0.0549 satisfying the requirement ($LP < 0.079$) given in [33].

3.2.6. Discussion

As it is discussed in the previous paragraphs, and presented in Table 2, we can conclude that the proposed technique is suitable for the construction of strong random S-boxes while it satisfies the requirements and offers best results compared the literature similar works.

4. Hardware requirements of proposed architecture

To explore the material performance of the proposed architecture, we used the structural description on VHDL language for low level implementation. The Register-Transfer-Level (RTL) description has been realized on the Xilinx PYNQ-Z2 FPGA prototyping board after synthesis, place and route steps on the the Xilinx Vivado design suite tools (V.2022.1) [13]. To ensure the best functionality of our design, we performed simulation tests at the different levels of design flow, behavioral, post-synthesis functional, post-synthesis timing, post-implementation functional, and post-implementation timing. After the success of these simulations we generated the bit-file and we programmed the FPGA chip.

4.1. Utilization, timing, and power reports analysis

The main information given on the report-utilization generated by the Xilinx Synthesis Technology (XST) after place and route, the timing metrics, and power requirements are presented in Table 3. As we can see, the designed architecture occupies low logic resources on the used Xilinx PYNQ-Z2 xc7z020clg400-1 FPGA device. More precisely, it requires only 1135 (2.13%) Slice LUTs (743 LUT as Logic and 392 LUT as Distributed RAM), 762 (0.72 %) Slice Registers (Register as Flip Flop), and 8 (3.64 %) DSP48E1. The mean of these tree main parameters (2.16 %) show that the available resources are used efficiently. In terms of timing metrics, the design can reach running frequency of 78.62 Mhz according to Equation 6. Where T = 13 ns and WNS = 0.28 ns (Worst Negative Slack, defined in Vivado implementation report. It gives the worst slack of all the timing paths. It is negative if a timing violation is detected in any path and positive, like our study, if all the paths satisfies the timing requirement). Therefore, the 32-bits stream-cipher generation can reach a throughput of 2515.84 Mbps according to Equation 7. If we consider that the architecture will be executed uniformly on the used logic Slices, we define the efficiency parameter according to Equation 8.

$$Max\_Freq = \frac{1}{T - WNS}\ [MHz] \tag{6}$$

$$Throughput = N \times Max\_Freq\ [Mbps] \tag{7}$$

$$Efficiency = \frac{Throughput}{Slices}\ [Mbps/Slices] \tag{8}$$

The power report indicates a total On-Chip consumption of 0.188 W (43 % dynamic and 57 % static). Therefore, in addition to hardware and timing metrics, this low energy requirement of the architecture favorite its utilization on embedded electronic and real-time data protection applications, like smartphone and IoT (Internet of Think) objects or devices.

5. Security evaluation and discussion

To evaluate the security performance of the proposed dynamic S-box-based ZUC stream cipher, we investigated its resilience against cryptanalysis attacks using the most useful tests known for their effectiveness in validating cryptosystems such as NIST statistical tests, keystream uniformity, keystream randomness, entropy, confusion, and diffusion properties, key sensitivity, and key space.

All the simulations have been implemented in Python 3.7 on a standard computer Intel(R) Core(TM) i7-10710U CPU 1.10 GHz operating under Microsoft Windows 10, 64-bit, 16 GB RAM, and 1.6 GHz cpu-speed.

5.1. Uniformity and key-stream distribution analysis

To evaluate the uniformity of a key-stream generated by the proposed algorithm, we encrypted different images (Figures 5(a), 5(b), 5(c), 5(d), 5(e)) of size 512 × 512 pixels using 2097152 generated bits. Then, we expected the histogram distribution of both the plain and encrypted images in each case. As we can notice in Figure 6 (row 2), the encrypted images are uniformly distributed and spatially spread. Unlike plain images following a distribution concentrated on a defined area of pixels, but not on others (see Figure 5, row 2). Therefore, we conclude that the proposed dynamic S-boxes improves the randomness of the generated output key-stream and ciphered data.

5.2. Uniformity and Chi-Square analysis

To confirm statistically the uniformity accurately of the generated key-stream and cipher-text, we explored the Chi-Square value [38] using Equation 9.

$$\chi_{exp}{}^2 = \sum_{i=1}^{N_c-1} \frac{(O_i - E_i)^2}{E_i} \tag{9}$$

Where $N_c = 2^8 = 256$ is the number of levels, O_i is the calculated occurrence frequency of each gray level, $i \in [0, 255]$ in the histogram of the ciphered image, and E_i is the expected occurrence frequency of the uniform distribution, calculated by $E_i = nb/N_c$. The theoretical value for $\alpha = 0.05$ and $N_c = 256$ is $\chi^2_{th}(255, 0.05) = 293.24$.

The mean value of the experimental Chi-square χ^2_{exp} over 20 cipher images is equal to $\chi^2_{exp} = 263.73$. The obtained value is consistent with the expectations of the definition for this test which considers a uniform cipher-text if the experimental value of its Chi-square is less than the theoretical value, as our case ($\chi^2_{exp} = 263.73 < \chi^2_{th} = 293.24$). According to this analysis, we conclude that the uniformity is confirmed by both the histogram distribution and Chi-square value.

Table 3: FPGA implementation results of the proposed dynamic-Sboxes-based ZUC stream cipher.

	Parameters	Area Utilization	Area Utilization in %
Board	Family Device	Zynq-7000 7z020-clg400	
Hardware resources	Slice LUTs FFs DSP	374 1135 762 8	(2.81 %) (2.13 %) (0.72 %) (3.64 %)
Time metrics	WNS (ns) Maximum Frequency (MHz) Throughput (Mbps)	0.29 78.68 2515.84	
Efficiency	Efficiency (Mbps/Slices)	6.73	
Consumption	Power (Watts)	0.188	

(a) Lena. (b) Peppers. (c) Lake. (d) Couple. (e) Black.

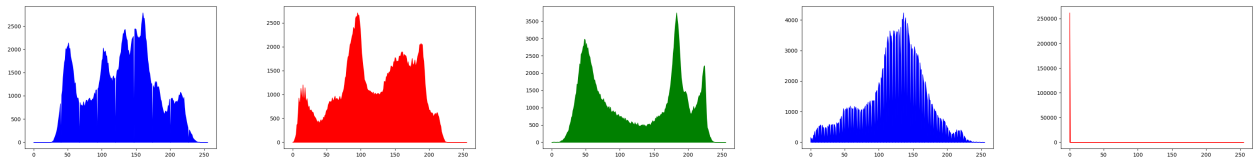

(f) Lena ditribution. (g) Peppers ditribution. (h) Lake ditribution. (i) Couple ditribution. (j) Black ditribution.

Figure 5: Plain images and their distributions.

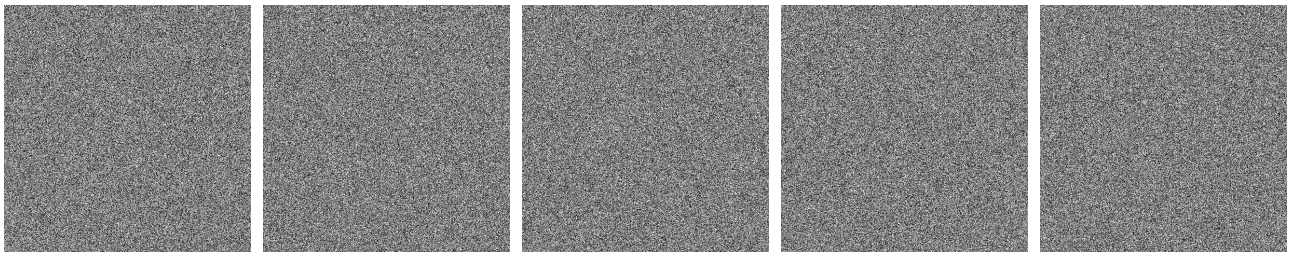

(a) Lena encrypted. (b) Peppers encrypted. (c) Lake encrypted. (d) Couple encrypted. (e) Black encrypted.

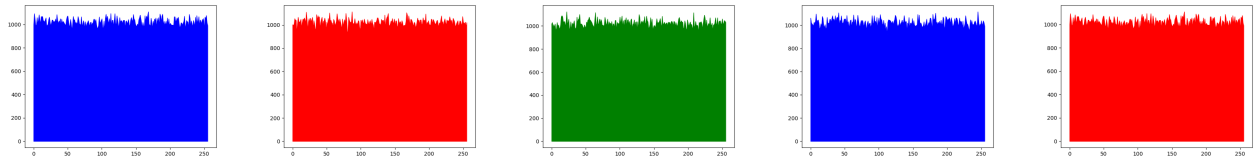

(f) Lena encrypted ditribution. (g) Peppers encrypted ditribution. (h) Lake encrypted ditribution. (i) Couple encrypted ditribution. (j) Black encrypted ditribution.

Figure 6: Encrypted images and their distributions.

5.3. Hamming distance and plain-text sensitivity analysis

To test, the sensitivity to any change on the plain-text, we calculate the average Hamming Distance (HD) between the plain-image (P) and the corresponding cipher-image (C), as given by Equation 10 over 20 different plain images.

$$HD(P,C) = \frac{1}{|N|}\sum_{k=1}^{N}(P[k] \oplus C[k]) \times 100\% \quad (10)$$

Where N is the size in bit of the plain and cipher images.

The obtained results presented in Figure 7 are very close to the optimal value 50%, as defined by the avalanche effect [39] indicating that the probability of bit changes between each ciphered-text and its corresponding plain-text is 50%.

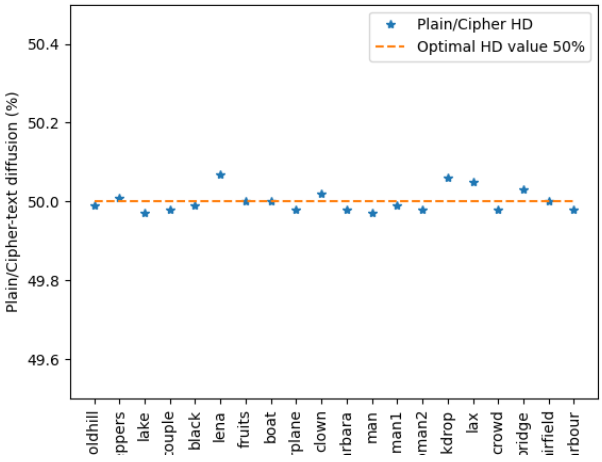

Figure 7: The plain-text sensitivity HD results.

5.4. Hamming distance and secret key sensitivity analysis

Similarly to the previous test, we evaluated the sensitivity to few change on the secret key. The test was performed by ciphering the same plain-image twice using two keys with only one bit of difference to obtain two ciphered-images C_1 and C_2. Then we calculate the HD between C_1 and C_2 using Equation 11 over 100 different secret keys.

$$HD(C_1,C_2) = \frac{1}{|N|}\sum_{k=1}^{N}(C_1[k] \oplus C_2[k]) \times 100\% \quad (11)$$

The obtained results presented in Figure 8 are also very close to the optimal value 50% indicating that a change of only one bit in the secret key leads to a thoroughly different key-stream. This proves the high sensitivity of the proposed ZUC stream to the secret key as defined by the avalanche effect [40] with respect to the confusion property given by Shannon's theory [41, 42]. This means that the complex statistical relationship between the secret key, the plain image, and the encrypted image makes it difficult to recover the secret key even with knowledge of multiple plain-encrypted image pairs.

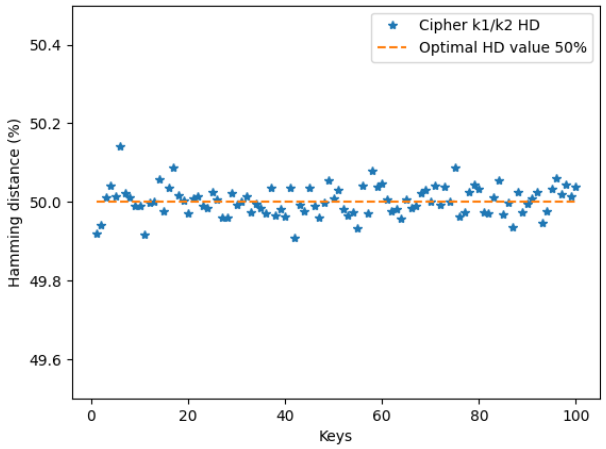

Figure 8: The key sensitivity HD results.

5.5. Key space analysis

The key space of the enhanced ZUC design is improved from 2^{128} to 2^{256} thanks to the use of two dynamic keys to run the chaotic maps and generate the new S-boxes (SD_0 and SD_1). The principle was the combination use of both 128-bits CK and IV to generate the keys KD_1 and KD_2. Therefore, any change in the value of CK or IV leads to the generation of a new S-boxes and a new key-stream, which makes brute-force attacks infeasible.

5.6. NIST statistical tests analysis

For a thorough analysis of the properties of the generated keystream, we used the NIST battery of statistical tests [8, 7, 15, 18, 19]. To explore the fifteenth test, we analyzed a set of 100 generated sequences given by the proposed algorithm. In all the experiments, we set the significance level to 0.01. From the obtained results shown in Table 4, we remark that the proposed ZUC design passes in success all the NIST tests, which prove the high robustness and the best statistical properties of our architecture allowing us to ensure a high-level protection of digital data (text, image, etc.).

5.7. Discussion

As we presented in the above subsections, all the applied experimental results prove the best performance and the enhancement of the generated key-stream. Starting by the uniformity proved by the histogram distribution and the Chi-square value. Then, the sensitivity to any changes in both the plain-text and the secret key proved with respect to the avalanche effect [40] and Shannon's theory [41]. After that, the randomness and the statistical properties proved by the NIST tests. And finally, the complexity of secret key cracking has been doubled by improving the key space from 2^{128} to 2^{256}. Additionally, the high level of the proposed dynamic S-box

Table 4: NIST test results.

Number of test	Type of test	P-Value	Result
1	Frequency (mono-bit) Test	0.437749	success
2	Frequency Test within a Block	0.407566	success
3	Runs Test	0.942123	success
4	Tests for the longest-Run-of-ones in a Block	0.349813	success
5	Binary Matrix Rank Test	0.730751	success
6	Discrete Fourier Transform (Spectral) Test	0.076546	success
7	Non-overlapping Template Matching Test	0.574824	success
8	Overlapping Template Matching Test	0.884123	success
9	Maurer's "Universal Statistical" Test	0.238481	success
10	Linear Complexity Test	0.523428	success
11	Serial Test	0.945384	success
12	Approximate Entropy Test	0.583708	success
13	Cumulative sums Test	0.811180	success
14	Random excursion Test	0.711607	success
15	Random excursion variant Test	0.551820	success

as proved by the main useful criteria (bijection, SAC, non-linearity, BIC, equiprobable input/output XOR distribution, differential approximation probability, maximum expected linear probability) and by the comparison with the literature similar works enforce the whole security of the cryptosystem based on this strong S-box. This means that we have strengthened the resistance of the ZUC stream cipher against cryptanalysis attacks such as brute force attacks, statistical attacks, linear attacks, and differential attacks.

Consequently, we conclude that the combination of the ZUC stream cipher with the proposed dynamic chaotic S-boxes layer increases the data protection for LTE and the new generation of mobile networks.

6. Conclusion

In this article, we have improved the internal architecture of the standardized ZUC stream cipher by combining the original design with a chaos-based generator responsible for generating two dynamic S-boxes (SD_0 and SD_1) in place of the basic static S-boxes (S_0 and S_1). Then, we performed its FPGA-based (Xilinx XC7Z020 ZYNQ platform) implementation using a VHDL description structural language to reach the high performance metrics in terms of material logic resources (Slice LUT, Slice FF, and DSP), and timing requirements (Maximum frequency, WNS, and Throughput). We have also presented the security robustness of the enhanced algorithm as any new proposed cryptosystem.

By analyzing the results obtained, we conclude that the proposed design is adapted to real-time data transmission while achieving a high throughput. In addition, it is suitable for embedded applications while occupying a low area and consuming low energy. Finally, it can ensure a secured transmission of digital data in mobile and IoT networks (it guarantees confidentiality and integrity protections) while resisting brute force, statistical, and differential attacks without modification to the standardized requirements.

In our future work, we will explore how to lighten the computations of the NLF layer while keeping the same level of security. We will also aim to improve the temporal performance to achieve an encryption throughput as close as possible to the order of Gbps.

Conflict of Interest The authors declare no conflict of interest.

Acknowledgment This work was supported by the Bourgogne Franche-Comte region as part of the ANER number 2024PRE00022 project entitled CIAPD.

References

[1] "Specification of the 3GPP Confidentiality and Integrity Algorithms EEA3 & EIA3; Document 1: EEA3 and EIA3 specifications," Technical specification (TS) TS 35.221 V12.0.0, 3GPP, 2014-09.

[2] "Digital cellular telecommunications system (Phase 2+); Universal Mobile Telecommunications System (UMTS); LTE; 3GPP System Architecture Evolution (SAE); Security Architecture," Technical Specification (TS) ETSI TS 133 401 V11.5.0, 3GPP, 2012-10.

[3] "Specification of the 3GPP Confidentiality and Integrity Algorithms EEA3 & EIA3; Document 2: ZUC specification," Technical specification (TS) TS 35.222 V12.0.0, 3GPP, 2014-09.

[4] M. J. AlMashrafi, "A different algebraic analysis of the ZUC stream cipher," in Proceedings of the 4th international conference on Security of Information and Networks (SIN), 139–153, ACM New York, NY, USA ©2011, Sydney, Australia, 2011, doi:10.1145/2070425.2070455.

[5] W. Hongjun, H. Tao, H. Phuong, W. Huaxiong, L. San, "Differential Attacks against Stream Cipher ZUC," in International Conference on the Theory and Application of Cryptology and Information Security, 262–277, ASIACRYPT 2012: Advances in Cryptology, 2012, doi:10.1007/978-3-642-34961-4 17.

[6] F. Lafitte, O. Markowitch, D. Van Heule, "SAT based analysis of LTE stream cipher ZUC," Journal of Information Security and Applications, **22**, 54–65, 2013, doi:10.1016/j.jisa.2014.09.004.

[7] M. Madani, I. Benkhaddra, C. Tanougast, S. Chitroub, L. Sieler, "Enhanced ZUC Stream Cipher Based on a Hyperchaotic Controller System," in The Euromicro Conference on Digital System Design DSD 2017, Work In Progress Session, Vienna, Austria, 30 August-1 September 2017.

[8] M. Madani, C. Tanougast, "Combined and Robust SNOW-ZUC Algorithm Based on Chaotic System," in The International Conference on Cyber Security and Protection of Digital Services (Cyber Security 2018), 1168–1173, IEEE, Glasgow, Scotland, UK, 2018.

[9] F. Özkaynak, "Construction of robust substitution boxes based on chaotic systems," Neural Computing and Applications, **31**, 3317–3326, 2019, doi:10.1007/s00521-017-3287-y.

[10] F. Artuğer, F. Özkaynak, "A method for generation of substitution box based on random selection," Egyptian Informatics Journal, **23**(1), 127–135, 2022, doi:10.1016/j.eij.2021.08.002.

[11] K. Mohamed, M. N. Mohammed Pauzi, F. H. Hj Mohd Ali, S. Ariffin, N. H. Nik Zulkipli, "Study of S-box properties in block cipher," in 2014 International Conference on Computer, Communications, and Control Technology (I4CT), 362–366, 2014, doi:10.1109/I4CT.2014.6914206.

[12] A. Msolli, I. Hagui, A. Helali, "Dynamic S-boxes generation for IoT security enhancement: A genetic algorithm approach," Ain Shams Engineering Journal, **15**(11), 103049, 2024, doi:10.1016/j.asej.2024.103049.

[13] "Zynq-7000 SoC Technical Reference Manual," Ug585 (v1.13), Xilinx, 2021.

[14] "PYNQ Z2 Reference Manual," v1. 1, PYNQ™, 2019.

[15] A. Rukhin, et al, "A Statistical Test Suite for the Random and Pseudorandom Number Generators for Cryptographic Applications," NIST Special Publication 800-22, 2001, Revised: April 2010, doi:http://csrc.nist.gov/rng/SP800-22b.pdf.

[16] "Cid C, Murphy S, Pipir F, Dodd M, ZUC algorithm evaluation repport," Technical report, 2010.

[17] "Knudson LR, Preneel B, Rijman V, Evaluation of ZUC," Technical report, 2010.

[18] M. Madani, I. Benkhaddra, C. Tanougast, S. Chitroub, L. Sieler, "FPGA Implementation of an enhanced SNOW-3G Stream Cipher based on a Hyper-chaotic System," in The 4th international conference on Control, Decision and Information Technologies (CoDIT'17), 1168–1173, IEEE, Barcelona, Spain, 2017.

[19] M. Madani, I. Benkhaddra, C. Tanougast, S. Chitroub, L. Sieler, "Digital Implementation of an Improved LTE Stream Cipher SNOW-3G based on Hyperchaotic PRNG," Security and Communication Networks, Hindawi with John Wiley & Sons, **2017**, 15 pages, 2017, doi:10.1155/2017/5746976.

[20] M. Madani, S. El Assad, C. Tanougast, M. J. Vella, E.-B. Bourennane, O. Deforges, "FPGA-Based Implementation of Enhanced ZUC Stream Cipher Based on Dynamic S-Box," in 2023 International Conference on Engineering and Emerging Technologies (ICEET), 1–6, 2023, doi:10.1109/ICEET60227.2023.10526075.

[21] F. Dridi, S. El Assad, W. El Hadj Youssef, M. Machhout, R. Lozi, "Design, Implementation, and Analysis of a Block Cipher Based on a Secure Chaotic Generator," Applied Sciences, **12**(19), 2022, doi:10.3390/app12199952.

[22] Ü. Cavusoğlu, A. Zengin, I. Pehlivan, S. Kacar, "A novel approach for strong S-Box generation algorithm design based on chaotic scaled Zhongtang system," Nonlinear Dynamics, **87**(2), 1081–1094, 2017, doi:10.1007/s11071-016-3099-0.

[23] D. Lambić, "A novel method of S-box design based on discrete chaotic map," Nonlinear Dynamics, **87**, 2017, doi:10.1007/s11071-016-3199-x.

[24] H. Alhadawi, M. Zolkipli, M. Ahmad, "A novel efficient substitution-box design based on firefly algorithm and discrete chaotic map," Neural Computing and Applications, **31**, 2019, doi:10.1007/s00521-018-3557-3.

[25] Q. Lai, A. Akgul, C. Li, G. Xu, Ü. Çavusoğlu, "A New Chaotic System with Multiple Attractors: Dynamic Analysis, Circuit Realization and S-Box Design," Entropy, **20**(1), 2018, doi:10.3390/e20010012.

[26] E. Al Solami, M. Ahmad, C. Volos, M. N. Doja, M. M. S. Beg, "A New Hyperchaotic System-Based Design for Efficient Bijective Substitution-Boxes," Entropy, **20**(7), 2018, doi:10.3390/e20070525.

[27] Z. Xuanping, Z. Zhongmeng, W. Jiayin, "Chaotic image encryption based on circular substitution box and key stream buffer," Signal Processing: Image Communication, **29**(8), 902–913, 2014, doi:10.1016/j.image.2014.06.012.

[28] L. Dragan, "A novel method of S-box design based on chaotic map and composition method," Chaos, Solitons & Fractals, **58**, 16–21, 2014, doi:10.1016/j.chaos.2013.11.001.

[29] G. Liu, W. Yang, W. Liu, Y. Dai, "Designing S-boxes based on 3-D four-wing autonomous chaotic system," Nonlinear Dynamics, **82**, 2015, doi:10.1007/s11071-015-2283-y.

[30] R. Guesmi, M. A. Ben Farah, A. Kachouri, M. Samet, "A novel design of Chaos based S-Boxes using genetic algorithm techniques," in 2014 IEEE/ACS 11th International Conference on Computer Systems and Applications (AICCSA), 678–684, 2014, doi:10.1109/AICCSA.2014.7073265.

[31] F. Özkaynak, A. B. Özer, "A method for designing strong S-Boxes based on chaotic Lorenz system," Physics Letters A, **374**(36), 3733–3738, 2010, doi:10.1016/j.physleta.2010.07.019.

[32] G. Chen, "A novel heuristic method for obtaining S-boxes," Chaos, Solitons & Fractals, **36**(4), 1028–1036, 2008, doi:10.1016/j.chaos.2006.08.003.

[33] M. Š. Dragan Lambić, Publications de l'Institut Mathématique, (113), 109–115.

[34] T. Cusick, P. Stănică, Cryptographic Boolean Functions and Applications: Second edition, 2017.

[35] A. F. Webster, S. E. Tavares, "On the Design of S-Boxes," in H. C. Williams, editor, Advances in Cryptology — CRYPTO '85 Proceedings, 523–534, Springer Berlin Heidelberg, Berlin, Heidelberg, 1986.

[36] L. Keliher, H. Meijer, "A New Substitution-Permutation Network Cipher Using Key-Dependent S-Boxes," in H. C. Williams, editor, SAC 97, 13–26, 1997.

[37] L. Keliher, "Refined Analysis of Bounds Related to Linear and Differential Cryptanalysis for the AES," volume 3373, 42–57, 2004, doi:10.1007/11506447_5.

[38] S. G. Meintains, Z. HLÁÁVKA, "Goodness-of-Fit Tests for Bivariate and Multivariate Skew-Normal Distribution," Scandinavian Journal of Statistics, **37**(4), 701–714, 2010, http://www.jstor.org/stable/41000416.

[39] D. Han, L. Min, G. Chen, "A Stream Encryption Scheme with Both Key and Plaintext Avalanche Effects for Designing Chaos-Based Pseudorandom Number Generator with Application to Image Encryption," International Journal of Bifurcation and Chaos, **26**(5).

[40] D. Han, L. Min, G. Chen, "A Stream Encryption Scheme with Both Key and Plaintext Avalanche Effects for Designing Chaos-Based Pseudorandom Number Generator with Application to Image Encryption," International Journal of Bifurcation and Chaos, **26**(5), 2016, doi:10.1142/S0218127416500917.

[41] C. Shannon, "Communication Theory of Secrecy Systems," Bell Systems Technical Journal, **28**, 656–715, 1949.

[42] Y. Wu, Y. Zhou, G. Saveriades, S. Agaian, J. Noonan, P. Natarajan, "Local Shannon entropy measure with statistical tests for image randomness," Inf. Sci, **222**, 323–342, 2013.

Advances in Science, Technology and Engineering Systems Journal Vol. 10, No. 1, 48-59 (2025)

www.astesj.com

ASTESJ

ISSN: 2415-6698

Text Line Segmentation on Myanmar Handwritten Document using Average Linkage Clustering Algorithm

Nilar Phyo Wai [1*], Nu War [2]

[1]*Image and Signal Processing Lab, University of Computer Studies, Mandalay, Mandalay, 05071, Myanmar*

[2]*Faculty of Computer Systems and Technologies, Myanmar Institute of Information Technology, Mandalay, 05071, Myanmar*

ARTICLE INFO

Article history:
Received: 06 January, 2025
Revised: 22 January, 2025
Accepted: 23 January, 2025
Online: 09 February, 2025

Keywords:
Myanmar Handwritten Document
Text Line Extraction
Text Line Segmentation
Connected Component Analysis
Average Linkage Clustering

ABSTRACT

Text line segmentation from document images is a significant challenge in the field of document image analysis. It involves extracting individual text lines from Myanmar handwritten document images to enable text recognition. This task becomes particularly challenging in Myanmar handwritten documents, especially those with irregular or cursive writing styles, due to variations in line spacing, and touching and overlapping characters in Myanmar handwritten documents. This paper proposes a text line extraction method based on an average linkage clustering algorithm for handwritten document images to address segmentation errors caused by characters with inconsistent spacing, different writing styles, and line overlaps due to ascenders and descenders. In this paper, Connected Components (CCs) are extracted by using Connected Component Analysis (CCA) and Anisotropic Gaussian multiscale technique. And then convex-hull computation based on the divide and conquer method is used to re-segment the irregular touching components. Then the text lines are extracted by the proposed system based on an average linkage clustering algorithm that consider both the smaller and larger within-cluster variance. The performance of the proposed method is evaluated using the Pixel and Line Intersection over Union (IU) values, which are found to be 93.27% of Pixel IU and 95.09% of Line IU on dataset I and 92.61% of Pixel IU and 89.90% of Line IU on dataset II, respectively. According to the experimental results based on the existing dataset and their own data set, the proposed system can give a better result than the Density-Based Spatial Clustering and Application with Noise (DBSCAN) clustering algorithm.

1. Introduction

Handwritten Text Recognition (HTR) is a crucial technology that converts handwritten content into digital text, typically for further processing such as information retrieval, classification, or translation. HTR continues to pose significant challenges and remains the focus on the research community's attention. Text line segmentation is a critical task for enhancing the performance of the handwriting recognition process. Despite advancements in text line segmentation methods for handwritten documents in various languages such as English, Chinese, Arabic, and Japanese, a significant need persists to segment text lines of handwritten documents written in the Myanmar language.

Myanmar has a lot of characters and is written in a left-to-right direction. Although it lacks uppercase and lowercase characters, it includes ascenders, descenders, and vowel diacritics. The challenges of Myanmar handwritten documents include cursive writing, diverse writing styles, diacritics, and overlapping and touching characters between text lines. Therefore, the development HTR of Myanmar handwritten document images for the Myanmar language has not been yet. The work presented in this paper extracts the text lines from handwritten document images by considering different styles in the language. Text line segmentation is generally seen as a preprocessing step for tasks

* Corresponding Author: Nilar Phyo Wai, University of Computer Studies, Mandalay, Mandalay, 05071, Myanmar, +959253150565, nilarphyowai@ucsm.edu.mm

https://dx.doi.org/10.25046/aj100106

such as document structure extraction, printed characters or handwritten recognition.

This research focuses on text line segmentation of handwritten documents for undergraduate students in Myanmar. The study works to achieve the segmentation of both long-length and short-length lines in handwritten documents and address the challenges of segmenting overlapping and touching lines.

The contributions of this research paper are summarized in the following:

- Creating a new dataset specific to Myanmar handwritten with detailed annotation and developing an average linkage clustering method tailored to Myanmar handwritten documents.
- Distinct blobs representing characters are obtained using Connected Component Analysis (CCA) and Gradient Magnitude, and then the convex hull refines the segmentation of the extracted connected characters.
- A proposed clustering algorithm extracts the detected components into text lines, handling overlapping and variable-length text lines.

The paper is organized as follows: section 2 describes the literature review of text line segmentation approaches. Section 3 explains the proposed method and then datasets are described in section 4. Section 5 demonstrates the experimental results and section 6 summarizes the research work.

2. Related Work

There are various techniques for text line segmentation in handwritten documents, including top-down and bottom-up approaches, scale-space representation and connected component analysis, and deep learning-based methods. This section discusses a representative of various text line segmentation trends in recent years.

Top-down approaches are analyze the entire document and partition it into smaller segments, such as text lines. In contrast, bottom-up methods begin by grouping smaller elements, such as characters or connected components, to construct text lines. Scale-space with Anisotropic Gaussian was used to obtain blob lines in handwritten images and extract text lines by analyzing connected characters on the detected blob lines. In deep learning techniques, neural networks extract relevant heterogeneous features.

In the paper [1], a text line and word segmentation system are presented using horizontal projection histogram (HPH) for unconstrained handwritten documents. The authors estimated the midpoint from the histogram and filled the gap between two consecutive lines. This algorithm is tested on two datasets which are Meitei Mayek handwritten and English languages. However, this approach varies segmentation accuracy that depends on constraints such as close and touching text line in handwritten documents. In [2], the authors utilized grid projection profiles to detect text areas in horizontal and vertical directions. Text areas in historical Tibetan images were extracted by applying specific rules to connected characters with corner points. The method focused on the straight text line of the Tibetan images.

In [3], the authors employed to construct graphs for the nearest neighbors based on pixel points, and then computed eigenvectors to normalized vectors of neighbors. Spectral clustering to group clusters as text lines based on the vectors. The authors [4] proposed that modified DBSCAN clustering was used to detect the baseline of Arabic handwritten documents using interest points which are obtained from the Extremely Randomized Trees (ERT) method.

The authors [5] proposed an innovative method for segmenting text lines in historical handwritten documents. The approach utilizes a scale-space representation with anisotropic Gaussian filters to identify blob lines. Subsequently, a component tree algorithm is employed to binarize the detected blobs. The final step involves extracting text lines through energy minimization using graph cuts. However, that needs to be the segmentation of multi-skewed text lines. In [6], an anisotropic Gaussian kernel was used to extract blob lines from a historical Manchu handwritten document, and broken blob lines were merged using morphological operations. Connected Component Analysis was performed to extract the text and segment the connected components based on overlapping set theory.

The authors [7] proposed a text lines extraction technique for handwritten images based on four aspects: horizontal and vertical projection, height of the text lines, size of the characters and curved nature of the alphabet. The authors consider the variation in character size caused by different handwriting styles. The problems of segmentation due to spaces of the character or overlapping text lines on account of the ascenders and descenders are reduced in the research work. To separate overlapping lines within the extracted segments, different thresholds are performed based on the average character height and width. The proposed method achieves 85.507% of the MatchScore value. This algorithm improves the performance of text line extraction and attains 99.39% of accuracy, 85.5% of detection rate and 91.92% of F-measure values. However, it is needed to consider touching and skew of text lines.

The authors developed a baseline detection algorithm using upper edges set and a text line segmentation method based on connected region analysis and baseline location [8]. The baselines were defined by expressions of two features, the number of upper edges and the duty ratio in the horizontal position. After that, the connected region with a height exceeding a specified threshold was identified as an adhesion region, which was then further truncated. Regions associated with the same baseline were then grouped to form a text line. The results indicated that segmentation accuracy was high, with strong resistance to distortion, and text line adhesion could be effectively managed. In this paper, distortion and line adhesion present significant but ongoing challenges, and future efforts could address these issues in two ways: learning-based segmentation methods and incorporating contextual semantics into text line segmentation.

In [9], author introduced VML-UTLS, an unsupervised convolutional network designed to learn proximity and similarity features within Arabic handwritten documents. This approach labels text lines at the pixel level by applying an energy minimization framework combined with detected blob lines.

The author proposed a method for predicting text line structure using Fully Convolutional Networks (FCNs). Their approach employed a line adjacency graph (LAG) to effectively segment components that intersect multiple text lines. While this model demonstrates robustness across various languages and can handle skewed text lines, it still needs to process complex natures involving touching components [10].

The Segmentation of text lines in heterogenous handwritten documents using deep learning techniques is robust and high-performance that requires large amounts of annotated label data which expensive and demands significant resources and time. The authors [11], presented text line extraction from historical documents using neural network techniques based on the Mask-RCNN network. This network is used to perform instance segmentation and to avoid misalignment between the region of interest and the extracted features. It was trained with the DRoSB dataset, French documents. To compare the performance of Mask-RCNN with U-Net networks, the cBAD 2017 database is used. The pixel and object level metrics are assessed for the performance evaluation. In hyperparameter turning, it is found that small scales and horizontal ratios gave better performance. In this paper, many experiments are conducted on Mask-RCNN, U-Net, and Doc-UFCN networks on different datasets. The results showed a better performance for Mask-RCNN that delivered with manageable computational demands, making it a practical choice for real-world text segmentation.

In [12], a neural network-based open-source Tesseract OCR engine is applied to recognize Myanmar handwritten characters. To convert binary images and reduce noises, Otsu's binarization algorithm and median filter method are used for pre-processing. The connected components labelling method is used for detecting text regions. Each connected component is bounded by a block of equal size. Despite some research on Myanmar character recognition, it remains in its early stages, with only limited literature available.

The text line segmentation system is presented for text line segmentation of challenging handwritten document images. The manuscript images contain narrow interline spaces with touching components, interpenetrating vowel signs and inconsistent font types and sizes. In addition, they contain curved, multi-skewed and multi-directed side note lines within a complex page layout. Therefore, bounding polygon labelling would be very difficult and time consuming. Instead of relying on line masks that connect the components on the same text line, these line masks are predicted using a Fully Convolutional Network (FCN). In the literature, FCN has been successfully used for text line segmentation of regular handwritten document images. This paper demonstrates that FCN is useful for challenging manuscript images as well. Using a new evaluation metric that is sensitive to over segmentation as well as under segmentation, testing results on a publicly available challenging handwritten dataset are comparable with the results of a previous work on the same dataset [13].

The authors [14] proposed an accurate text line segmentation in the presence of both cleanly written and struck-out text by addressing a crucial challenge in handwritten document processing. The approach effectively integrates stroke width estimation, noise filtering, morphological operations, and a DenseNet-based deep learning model to distinguish struck-out components from clean text. Additionally, spatial features and component directionality are utilized to form text lines progressively. The study's strength lies in its novel dataset, which specifically includes struck-out text, making it more representative of real-world scenarios. The experiments conducted on both the new dataset and standard benchmarks (ICDAR2013 and ICDAR2019 HDRC) demonstrate superior performance compared to existing methods. However, the approach's reliance on deep learning models may introduce computational overhead, which could be a limitation in resource-constrained environments. Furthermore, while the proposed methodology is effectiveness, its adaptability to various handwriting styles, languages, and extreme document degradation remains an area for further exploration.

Previous research works focus on different handwriting styles, overlapping text lines, multi-touching text lines, skewed text lines on handwritten document images. In this paper, an unsupervised clustering algorithm with average linkage is designed for text line segmentation in Myanmar handwritten document images, which contain cursive writing, overlapping and skewed text lines, and characters of varying scales. This approach enhances segmentation performance by effectively handling overlapping and skewed text lines. The proposed system obtains the higher performance on the segmentation of different line spacing, both short and long-length text lines, overlapping and skewed text lines.

3. Proposed Methodology

The steps of the proposed system are summarized as pre-processing, scale-space representation and gradient magnitude calculation, CCs extraction with CCA, text line extraction using a proposed algorithm, and then segments touching CCs. The design of the proposed system is shown in Figure 1.

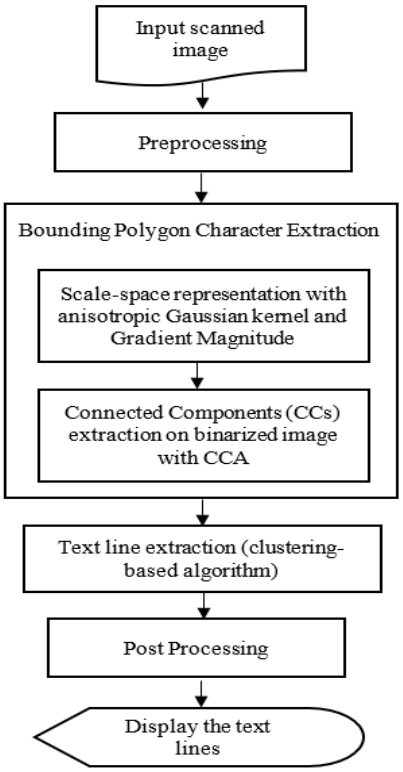

Figure 1: The design of the proposed system

3.1. Preprocessing

Pre-processing steps are essential for enhancing the performance of text line segmentation in scanned handwritten images of undergraduate students in Myanmar. The approach

incorporates several pre-processing techniques, including removing lines, red marks, noise, and binarization on and cropping the input handwritten image.

Firstly, the input scanned image is converted to the Hue, Saturation, and Value (HSV) color space is better isolate specific colors., saturation, and value (HSV) color thresholding, which isolates red hues within defined HSV ranges and then removes them with inpainting, which is filled the detected regions with surrounding pixel values to restore the original appearance of the input image. After red mark removal, morphological closing operations are applied using two line-shaped kernels: a horizontal kernel to remove underlines and a vertical kernel to remove margin lines. Next, median filtering addresses bleed-through, stains, and salt-and-pepper noise. The input scanned handwritten images of undergraduate Myanmar students are shown in Figures 2 and 3. The pre-processed images are described in Figures 4 and 5.

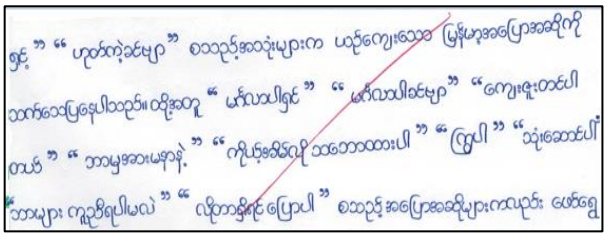

Figure 2: The scanned handwritten image of Dataset I

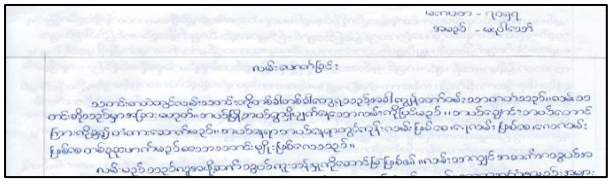

Figure 3: The scanned handwritten image of Dataset II

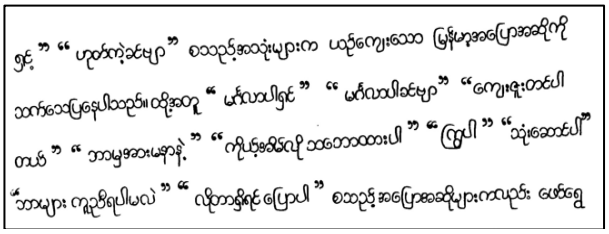

Figure 4: Preprocessed image of Dataset I

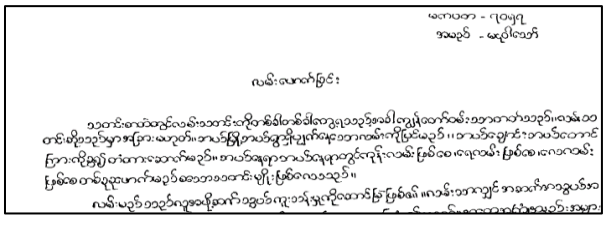

Figure 5: Preprocessed image of Dataset II

3.2. Scale-space Representation with Directional Gaussian Kernel

Scale-space representation is widely used multiscale technique for analyzing unknown image structures at various levels of detail. The scale-space representation of the image uses a directional Gaussian kernel with appropriate scale aims to obtain coarse and fine image structuring. It can also retain the significant features of the image. The choice of scale crucially influences the resulting scale-space representation. An anisotropic Gaussian kernel, as described in (1), is applied to the input handwritten image to produce the scale-space image..

$$G(x,y;\sigma) = \frac{1}{2\pi\sigma_x\sigma_y}\, e^{-\left(\frac{x^2}{2\sigma_x{}^2}+\frac{y^2}{2\sigma_y{}^2}\right)} \tag{1}$$

The image scaled in the horizontal direction by convolving it with a Gaussian kernel $G(x,y;\sigma_x)$ in (2).

$$I_x = G(x,y;\sigma_x) * I(x,y) \tag{2}$$

where σ_x represents a standard deviation along the x-axis. To scale the image vertically, it is convolved with a Gaussian kernel $G(x,y;\sigma_y)$, as specified by (3).

$$I_y = G(x,y;\sigma_y) * I(x,y) \tag{3}$$

where σ_y represents a standard deviation along the y-axis.

The concepts of gradient orientation and gradient magnitude is essential for extraction information from digital images, enabling various applications such as object recognition, image segmentation, and edge detection. The gradient magnitude is computed for the scale-space representation in (4), emphasizing regions of significant intensity changes are essential for identifying structural features in both directions.

$$I(x,y) = \sqrt{I_x{}^2 + I_y{}^2} \tag{4}$$

3.3. Coarse Segmentation

Connected Component Analysis (CCA) is a fundamental technique in image processing used to identify and label distinct regions within a binary image. It leverages gradient magnitude from scale-space images to accurately identify and group pixels of connected components (CCs), such as text characters, based on their intensity and boundary features. This approach ensures the effective extraction of components to overcome the challenges of faint characters, touching characters, or noisy backgrounds. Binarization of the gradient image uses the adaptive thresholding method to identify foregrounds (text) and backgrounds. In Figure 6, CCA is applied to the binarized image to detect and extract a group of connected pixels (x_{min}, y_{min}, x_{max} , x_{max}) into distinct CCs using 8-connectivity to ensure accuracy.

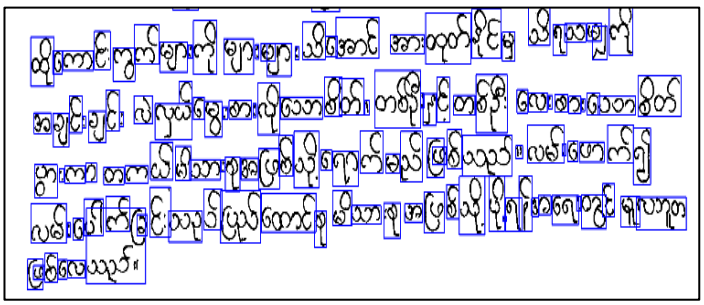

Figure 6: CCs extraction on the preprocessed image

3.*4 Fine Segmentation*

After extracting connected characters from distinct blobs in handwritten document images, some bounding boxes may be incorrect due to overlapping (almost touching) components, as illustrated in Figures 7 (a) and 8 (a).

3.4.1 Correction of CCs

The median value of CCs is calculated to combine (◌့, ◌်, and ◌း) and detect the irregular bounding box by the following equation.

M=median {all height of connected characters on the entire document}
H=height of each connected character

Two sets are defined to combine (◌့, ◌်, and ◌း) from the connected characters extraction.

The set of small CCs is defined as:

$$S = \{s_1, s_2, s_3 \ldots, s_a | \, \mathrm{H}\,(s_i) < \frac{M}{2}\} \quad (5)$$

where: a is number of small connected components

The set of large CCs is defined as larger than equal of M

$$L = \{l_1, l_2, l_3 \ldots, l_b | \, \mathrm{H}\,(l_i) \geq \mathrm{M}\} \quad (6)$$

where: b is the number of large connected components

Find the horizontal proximity and vertical proximity (between CCs from S set and L set between 10 and 20 to combine CCs as Figures 7(b).

(a) (b)

Figure 7: (a) Before and (b) After combination of some CCs

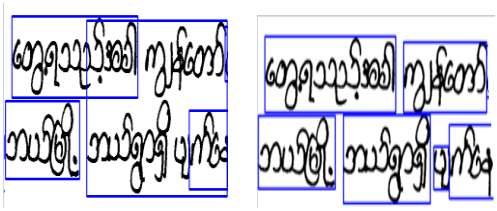

Figure 8: (a) Before and (b) After applying convex hull to segment the almost-touching CCs

And in this system, the irregular bounding boxes are considered by using the following three conditions

(i) Cursive writing case if (H> 2 M and M >=60)
(ii) Overlapping writing case if (H> 2.5 M and M <60)
(iii) Untouched Consonants Case (Ascenders & Descenders) if (H >3 M and M <50)

Connected Components (CCs) fit the above three conditions which must be considered irregular and continued.

To correct the bounding box each CCs from the irregular Connected Component list, the system extracts the boundaries of connected characters or the external contours (endpoints of horizontal, vertical, or diagonal segments). For finding the convex hull of a set of points in irregular list, the divide-and-conquer algorithms is used to compute the convex hull and works by recursively dividing the set of points into two halves, computing the convex hull for each half, and then merging the two hulls together [15]. The correct bounding boxes is shown in Figure 8 (b).

3.4.2 Finding Distance Threshold

After correction of bounding box, the system extract height of CC from the updated Connected Component list of each document as below:

$$\mathrm{H} = \{h_1, h_2, h_3, \ldots \ldots \ldots, h_n\}$$

threshold = Median (H)

The procedure of proposed text line extraction based on average linkage clustering method is described as following:

Proposed Algorithm

Result: Text line of hierarchical clustering records C_{new_k} where k is the number of text lines

Input: The bounding box of the connected component b_i, where i=1, 2, …. …, n; number of bounding boxes of handwritten document image

$$b_i = \{x_{i_{start}}, x_{i_{end}}, y_{i_{start}}, y_{i_{end}}\}$$

begin Initialize each cluster of handwritten document image and threshold

$$mc_i = \frac{(y_{i_{start}} + y_{i_{end}})}{2}, where: \; i = 1, 2, \ldots, n$$

C = {C₁, C₂, …, Cn} = {{ mc_1 },{ mc_2 }, …., { mc_n }}
where n is the number of clusters
Minimum distance: $d_{min} = \infty$
k=1

while length (C) > 1 **do**
for i=1 to (length (C) - 1) **do**
for j= (i+1) to length (C) **do**
Calculate distances using average linkage between C_i *and* C_j :

$$d = \frac{1}{|C_i| \times |C_j|} \sum_{mc_i \in C_i} \sum_{mc_j \in C_j} D(mc_i, mc_j)$$

if $d < d_{min}$ **then** $d_{min} = d$
if $d_{min} < threshold$ **then**
Record the cluster index for merging:
Merge_i= i, Merge_j=j
Merge cluster $C_{\mathrm{Merge_i}}$ and $C_{\mathrm{Merge_j}}$: $C_{new} = C_{\mathrm{Merge_i}} \cup C_{\mathrm{Merge_j}}$
Remove $C_{\mathrm{Merge_i}}$ and $C_{\mathrm{Merge_j}}$ from C.
Append C_{new} to C.
end
end
end
end
Record $\{V(b_i) | b_i \in C_{new_k}\}$: $C_{new_k} = C_{new}$
k=k+1
end

Final Merging for larger and smaller within-cluster variance (Very small handwritten style or high line skew):

find y_{min}, y_{max} *and* y_{mid} for C_{new_k} cluster

$y_{mid_m} = \frac{y_{min_m} + y_{max_m}}{2}$ where: m=1, 2, 3, ……, k

for i= 1 to k-1

j=i+1

$distance = \left| y_{mid_i} - y_{mid_j} \right|$

if $(distance \leq threshold)$ **then**

merge cluster $C_{\text{new\_i}}$ and $C_{\text{new\_j}}$

end

end

update C_{new_k}

end

The inputs of proposed algorithm are $x_{start}, x_{end}, y_{start,}, y_{end}$ coordinate points of the detected characters. The algorithm initializes the center point of the detected characters as its own cluster. In the matrix, the different values of all clusters are saved and then found the minimum values of distance are found. If the minimum values are smaller than the threshold, they will form as new cluster. To update the distance between clusters, average linkage is used. Then, minimum distance is found again in the clusters and forming clusters are combined with other clusters until the clusters are smaller than the threshold. In the combining merge clusters, the midpoint is calculated and merged if it is smaller than the threshold. Finally, the algorithm provides the clusters of text lines from handwritten document images.

The proposed algorithm employs an unsupervised hierarchical clustering approach with average linkage. This clustering method begins by treating each data point as its own cluster and iteratively merges the closest clusters within the range of the distance threshold. The hierarchical clustering is influenced by the choice of linkage criteria, with average linkage being a popular and effective method for clustering data points. Average linkage is the method that involves considering the distances between all pairs of points in the two clusters and averages all of these distances. It is applied to cluster similarity of spatial constraints on time series [16] and to determine elements in coal [17].

The proposed algorithm merges the extracted CCs as text lines using average distance linkage to efficiently extraction on text line of Myanmar and Malayalam handwritten document images [7] shown in Figures 9 and 10.

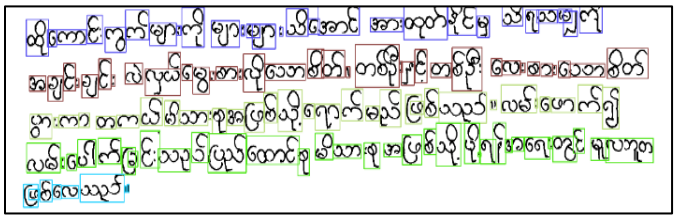

Figure 9: Text line extraction with the proposed algorithm

3.4. Post Processing

After text line extraction, the irregular bounding boxes, defined by the above three conditions, are segmented to improve the performance of text line segmentation based on the height of CCs of nearest clusters, as shown in Figure 11.

Each color represents a specific text line in the clustering results, providing a clear visual distinction for segmenting text lines in the handwritten document.

Figure 10: Text line extraction on the Malayalam handwritten document

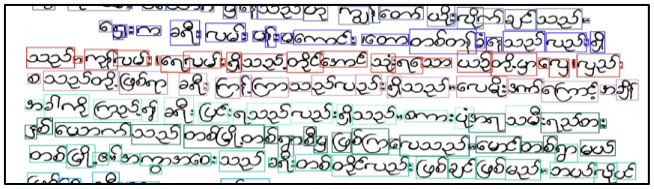

Figure 11: Text line segmentation on the Myanmar handwritten document

4. Myanmar Handwritten Document Images Dataset

4.1. Characteristics of Myanmar language

Myanmar language consists of 33 consonants, 12 vowels, 4 medials, 10 special characters, double-layered (Pali) characters, digits, and punctuation marks as shown in Figure 12. Some fundamental consonants in the Myanmar language can be standalone words. One must combine a consonant with one or more additional characters to create new words. It is written from left to right and read from top to bottom. Although it does not distinguish between uppercase and lowercase characters, it includes ascenders, descenders, and diacritics as shown in Figures 13 and 14.

4.2. Dataset

There is no benchmark dataset for segmenting text lines for Myanmar, even though many other languages have datasets of heterogeneous handwritten documents for document analysis. Therefore, in this work, Myanmar Handwritten documents are gathered by undergraduate students to create datasets. These documents were scanned at 300 dpi resolution. The text lines in the dataset are annotated using the Aletheia ground-truth tool [18] to obtain tight polygons of x and y coordinate points for each text line in PAGE-XML format. The Myanmar handwritten dataset contains Myanmar's alphabets, proverbs, prose, essays, numbers, adopted words, open and closed quotes, and some Pali words.

There are two formats of datasets: Dataset I) and Dataset II. The Dataset I includes simple handwritten documents and Dataset II contains challenging handwritten documents.

- Dataset I, contains 4161 text lines across 287 documents (images) covering various topics. The documents were written by 10 students from Myitkyina Education College. This

dataset includes the overlapping 50 lines and 39 skewed text lines.

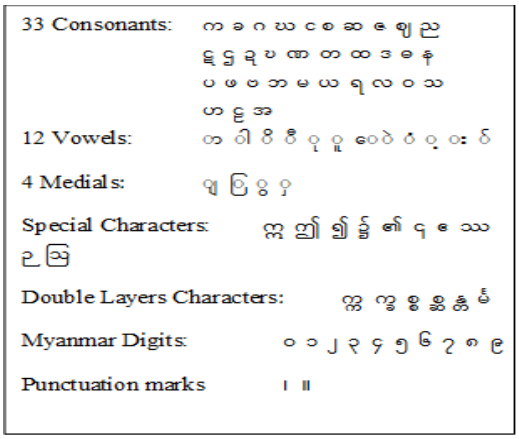

- Dataset II comprises 2664 text lines across 118 documents (images) on the same topics, written by 32 students from

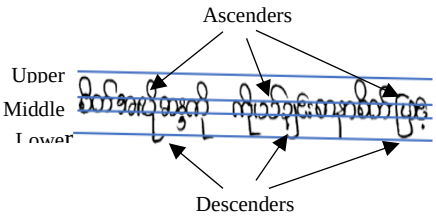

UCSM. This dataset includes 654 overlapping text lines, 79 skewed text lines, and 20 touching lines, and narrow line spacing which causes segmentation errors.

Figure 12: Myanmar Alphabets

Figure 14: Sample of Vowel diacritics on Myanmar Handwritten Word

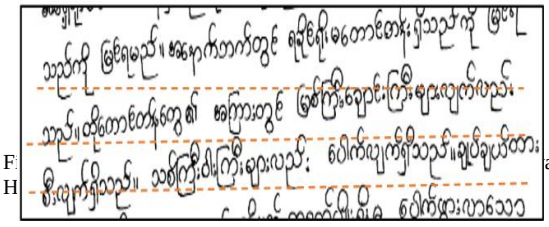

F anmar H

Figure 15: Inconsistent Spacing, Overlapping and Skewed Text Lines on Myanmar Handwritten Document

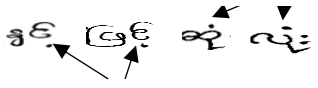

Vowel diacritic (outkamyint)

The characters, ascenders, descenders, and diacritics, narrow spacing are shown in Figures 13 and 14. These features introduce vertical complexity, making accurate segmenting of individual text lines more challenging, especially in Dataset II as shown in Figure 15.

The next section will discuss about evaluation metric and experimental details using the proposed approach. After that, the findings and discussion will be described.

5. Experiments

In this section, the performance of the proposed method and Density-Based Spatial Clustering and Application with Noise (DBSCAN) can be evaluated on the 405 documents for Myanmar Datasets and 293 Malayalam handwritten document images of LIPI-Database [7].

DBSCAN [19] groups data points are close to each other based on a density criterion, making it particularly effective for clustering irregularly shaped clusters and those with varying densities. The text line extraction of handwritten documents can adapt well to skewed or curved lines, commonly found in natural or cursive handwriting.

The DBSCAN algorithm clusters the center point of the y coordinate of each CC based on epsilon (ε) and minPts to extract text lines of the input image.

- Epsilon (ε): Half of the distance threshold for clustering (distance threshold is the median height of the connected characters of each handwritten document).
- minPts: this parameter requires at least two points to form a cluster.

The proposed method and DBSCAN function as unsupervised learning algorithms that do not require prior knowledge of the number of clusters.

5.1. Evaluation Metrics

Among many evaluation metrics for text line segmentation of handwritten documents, Pixel and Line Intersection over Union (IU) [20] are used to evaluate text line segmentation on the Myanmar handwritten datasets.

Pixel IU defines the accuracy of line detection at the pixel level in (7). In this case, TP represents the correctly detected pixels, FP refers to additional pixels erroneously identified, and FN indicates missed pixels.

$$Pixel\ IU\ = \frac{TP}{TP+FP+FN} \tag{7}$$

Line IU is a metric to evaluate how accurately individual lines have been detected in (8). Specifically, it measures the proportion of correctly identified lines. A threshold value of 0.75 is used to evaluate the experimental results.

$$Line\ IU = \frac{Intersection}{Union} \tag{8}$$

Intersection: Intersection is the number of correctly detected lines (true positives, TP).

Union: Union is the total number of lines in both the detected and ground truth sets, which include true positive (TP), false positive (FP) is extra text lines that were wrongly detected, and false negative (FN) indicates missed text lines. Precision, recall and F-measure are defined as follows:

$$\text{Precision} = \frac{TP}{TP+FP} \tag{9}$$

$$\text{Recall} = \frac{TP}{TP+FN} \tag{10}$$

$$\text{F-Measure} = \frac{2\times Precision\times Recall}{Precision+Recall} \tag{11}$$

5.2. Experimental Results

The distance threshold for each handwritten document is defined by the median height of the document's CCs. The threshold values are different based on individual handwriting styles, which impact on the performance of text line extraction with the clustering algorithms.

The following tables present the comparative analysis of different scale-space representation methods used for text line extraction: Gradient Magnitude with Anisotropic Gaussian, Laplacian of Anisotropic Gaussian, Laplacian of Gaussian (LoG), and Difference of Anisotropic Gaussian. The three methods are evaluated with two scales, (2,1) and (4,2), representing the sigma values applied in the x and y directions, respectively. LoG with automatic scale selection uses a minimum sigma of 1 and a maximum scale of 2.

Gradient Magnitude with Anisotropic Gaussian method on the clustering algorithms demonstrates good performance compared to other scale-space representation methods, particularly in challenging Myanmar handwritten document images, as shown in Tables 4 and 5. It also provides good result for Malayalam handwritten document images of LIPI Database in Table 6. Additionally, for simpler handwritten documents, the LoG yields more precise results than alternative approaches, as indicated in Tables 1 and 2. The difference of Anisotropic Gaussian is faster than other approaches in execution time in Tables 3 and 6. The execution time in Gradient Magnitude scale-space is faster than other methods in Table 9.

The proposed method uses average linkage to cluster the midpoints of CCs, so the method can perform on overlapping and inconsistent spacing text lines well. The proposed method on the Gradient Magnitude scale-space outperforms the results of text line segmentation with 95.09%, 89.90%, and 93.24% of Line IU on two datasets of Myanmar and LIPI database in Tables 2, 5, and 8 respectively. The results of DBSCAN are in 97.77%, 81.51%, and 87.68% for the evaluation of Line IU on those datasets in these three tables. Although DBSCAN has performed well in simple handwritten documents, the performance of challenging datasets is less efficient than the proposed clustering algorithm.

In Tables 1,4 and 7 are compared the Pixel IU of proposed method is compared with DBSCAN of Myanmar and Malayalam handwritten document images (LIPI) dataset. The results of Pixel IU of proposed method on the Gradient Magnitude scale-space are obtained 93.38%, 92.65% and 93.24% respectively. The DBSCAN method are found 96.01%, 89.63 % and 95.40% in Pixel IU in these three tables. The proposed method solves the problem overlapping text lines and variable length of text lines by using the integration of scale-space representation with average linkage clustering approach. The idea improves the segmentation results of different handwriting styles, varying line spacing and extracts different scales in handwriting.

The proposed method achieves higher recall by detecting more lines, however it introduces more false positives. Overall, text line segmentation of the proposed method is more effective, as indicated by its higher F-measure, balancing both precision and recall. The reliance of DBSCAN on fixed density threshold limits its ability to adapt to the variability of text line spacing and the presence of ascenders, descenders, and diacritics like Myanmar and Malayalam script. In comparison, the proposed method enables handling the varying structure of text lines, resulting in precision, recall, and F-measure values, particularly in complex datasets in Table 10. Experiments have been conducted on the HP Core i7 (12th-gen) system, using PyCharm Community 2020 and Python 3.9.

Table 1: Comparison results of Pixel IU on Myanmar Dataset I

Scale-Space Representation Methods	DBSCAN (%)	Proposed (%)
Laplacian of Anisotropic Gaussian (σ_x=2, σ_y=1)	74.50	66.07
Difference of Anisotropic Gaussian (σ_{x1}=4, σ_{y1}=2) (σ_{x2}=2, σ_{y2}=1)	85.26	78.70
Laplacian of Gaussian (LoG) $minimum_\sigma = 1$ and $maximum_\sigma$=2	**96.01**	**96.80**
Proposed Scale-Space Gradient Magnitude (σ_x=2, σ_y=1)	89.69	93.38
Proposed Scale-Space Gradient Magnitude (σ_x =4, σ_y=2)	90.06	93.27

Table 2: Comparison results of Line IU on Myanmar Dataset I

Scale-Space Representation Methods	DBSCAN (%)	Proposed (%)
Laplacian of Anisotropic Gaussian (σ_x=2, σ_y=1)	84.61	69.94
Difference of Anisotropic Gaussian (σ_{x1}=4, σ_{y1}=2) (σ_{x2}=2, σ_{y2}=1)	89.22	80.04
Laplacian of Gaussian (LoG) $minimum_\sigma$=1 and $maximum_\sigma$=2	**97.77**	**97.82**
Proposed Scale-Space Gradient Magnitude (σ_x=2, σ_y=1)	94.83	94.59
Proposed Scale-Space Gradient Magnitude (σ_x =4, σ_y=2)	93.31	95.09

Table 3: Comparison results of execution time in second on Myanmar Dataset I

Scale-Space Representation Methods	DBSCAN (sec)	Proposed (sec)
Laplacian of Anisotropic Gaussian (σ_x=2, σ_y=1)	684.15	5614.66
Difference of Anisotropic Gaussian ($\sigma_{x1} = 4, \sigma_{y1}$=2) ($\sigma_{x2}$=2, σ_{y2}=1)	396.93	**324.68**
Laplacian of Gaussian (LoG) $minimum_\sigma$=1 and $maximum_\sigma$=2	376.93	399.70
Proposed Scale-Space Gradient Magnitude (σ_x=2, σ_y=1)	362.50	369.49
Proposed Scale-Space Gradient Magnitude (σ_x =4, σ_y=2)	356.78	453.91

Table 4: Comparison results of Pixel IU on Myanmar Dataset II

Scale-Space Representation Methods	DBSCAN (%)	Proposed (%)
Laplacian of Anisotropic Gaussian (σ_x=2, σ_y=1)	76.55	62.09
Difference of Anisotropic Gaussian (σ_{x1}=4, σ_{y1}=2) (σ_{x2}=2, σ_{y2}=1)	86.59	73.96
Laplacian of Gaussian (LoG) $minimum_\sigma$=1 and $maximum_\sigma$=2	83.23	90.31
Proposed Scale-Space Gradient Magnitude (σ_x=2, σ_y=1)	89.26	**92.65**
Proposed Scale-Space Gradient Magnitude (σ_x =4, σ_y=2)	**89.63**	92.61

Table 5: Comparison results of Line IU on Myanmar Dataset II

Scale-Space Representation Methods	DBSCAN (%)	Proposed (%)
Laplacian of Anisotropic Gaussian (σ_x=2, σ_y=1)	68.33	55.16
Difference of Anisotropic Gaussian (σ_{x1}=4, σ_{y1}=2) (σ_{x2}=2, σ_{y2}=1)	77.63	67.34
Laplacian of Gaussian (LoG) $minimum_\sigma$=1 and $maximum_\sigma$=2	76.95	87.89
Proposed Scale-Space Gradient Magnitude (σ_x=2, σ_y=1)	81.00	89.60
Proposed Scale-Space Gradient Magnitude (σ_x =4, σ_y=2)	**81.51**	**89.90**

Table 6: Comparison results of execution time in second on Myanmar Dataset II

Scale-Space Representation Methods	DBSCAN (sec)	Proposed (sec)
Laplacian of Anisotropic Gaussian (σ_x=2, σ_y=1)	395.57	417.35
Difference of Anisotropic Gaussian (σ_{x1}=4, σ_{y1}=2)(σ_{x2}=2, σ_{y2} = 1)	**185.00**	187.06
Laplacian of Gaussian (LoG) $minimum_\sigma$=1 and $maximum_\sigma$=2	203.32	210.27
Proposed Scale-Space Gradient Magnitude (σ_x=2, σ_y=1)	200.54	211.08
Proposed Scale-Space Gradient Magnitude (σ_x =4, σ_y=2)	206.07	207.85

Table 7: Comparison results of Pixel IU on LIPI Database

Scale-Space Representation Methods	DBSCAN (%)	Proposed (%)
Laplacian of Anisotropic Gaussian (σ_x=2, σ_y=1)	89.73	70.87
Difference of Anisotropic Gaussian (σ_{x1}=4, σ_{y1}=2)(σ_{x2}=2, σ_{y2} = 1)	84.78	86.92
Laplacian of Gaussian (LoG) $minimum_\sigma$=1 and $maximum_\sigma$=2	94.21	**95.69**
Proposed Scale-Space Gradient Magnitude (σ_x=2, σ_y=1)	95.21	94.56
Proposed Scale-Space Gradient Magnitude (σ_x =4, σ_y=2)	**95.40**	94.85

Table 8: Comparison results of Line IU on LIPI Database

Scale-Space Representation Methods	DBSCAN (%)	Proposed (%)
Laplacian of Anisotropic Gaussian (σ_x=2, σ_y=1)	84.18	47.17
Difference of Anisotropic Gaussian (σ_{x1}=4, σ_{y1}=2)(σ_{x2}=2, σ_{y2} = 1)	92.29	74.02
Laplacian of Gaussian (LoG) $minimum_\sigma$=1 and $maximum_\sigma$=2	**92.85**	82.59
Proposed Scale-Space Gradient Magnitude (σ_x=2, σ_y=1)	87.28	92.67
Proposed Scale-Space Gradient Magnitude (σ_x =4, σ_y=2)	87.68	**93.24**

Table 9: Comparison results of execution time in second on LIPI Database

Scale-Space Representation Methods	DBSCAN (sec)	Proposed (sec)
Laplacian of Anisotropic Gaussian (σ_x=2, σ_y=1)	6013.87	913.82
Difference of Anisotropic Gaussian (σ_{x1}=4, σ_{y1}=2)(σ_{x2}=2, σ_{y2} = 1)	706.10	684.93
Laplacian of Gaussian (LoG) $minimum_\sigma$=1 and $maximum_\sigma$=2	342.31	285.64
Proposed Scale-Space Gradient Magnitude (σ_x=2, σ_y=1)	**261.03**	268.29
Proposed Scale-Space Gradient Magnitude (σ_x =4, σ_y=2)	1730.14	913.82

Table 10: Evaluation results of text line segmentation for proposed scale-space representation on Precision (P), Recall (R) and F-Measure (FM) on scale σ_x =4, σ_y=2

Dataset	Methods	No. of Text Lines	Correctly Text Lines	P (%)	R (%)	FM (%)
Myanmar Dataset I with 287 documents	DBSCAN	4161	4067	97.45	97.76	97.61
	Proposed Algorithm		4083	95.55	98.14	96.83
Myanmar Dataset II with 118 documents	DBSCAN	2664	2204	93.46	82.73	87.77
	Proposed Algorithm		2500	90.67	93.84	92.23
LIPI Database with 293 documents [7]	DBSCAN	5658	4937	91.52	92.95	92.23
	Proposed Algorithm		5285	97.97	93.40	95.63

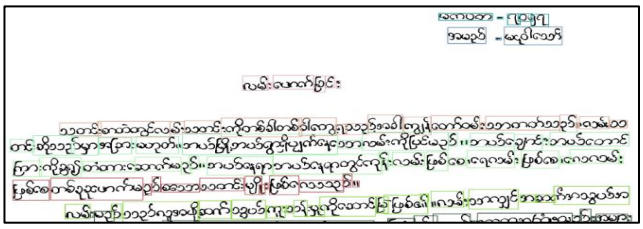

Figure 16: Text line segmentation of Gradient Magnitude with Anisotropic Gaussian on scale (2, 1)

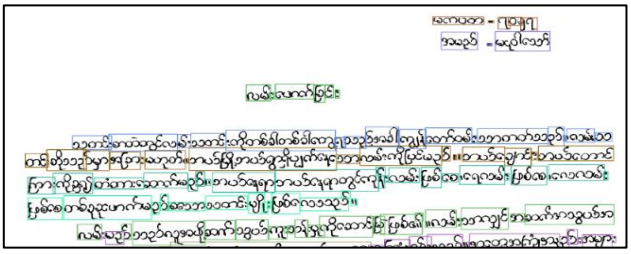

Figure 17: Text line segmentation of Gradient Magnitude with Anisotropic Gaussian on scale (4, 2)

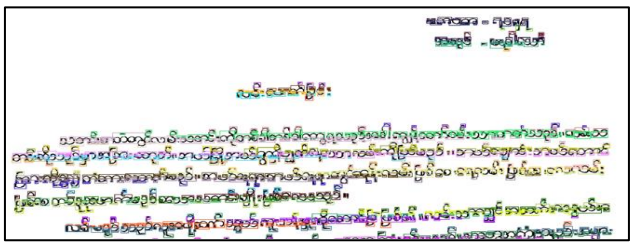

Figure 18: Text line segmentation of Laplacian of Anisotropic Gaussian on scale (2,1)

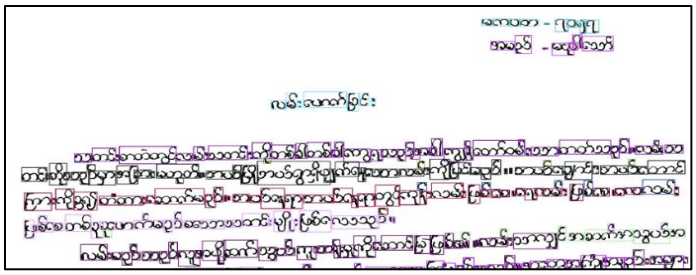

Figure 19: Text line segmentation of Difference of Gaussian with Anisotropic Gaussian on scales (4,2) and (2,1)

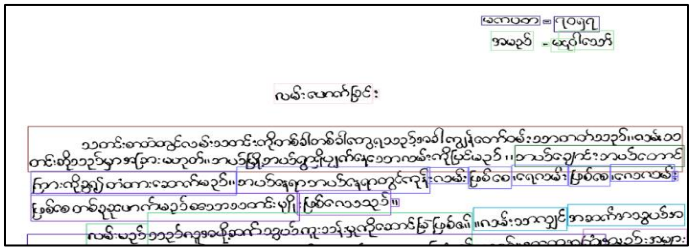

Figure 20: Text line segmentation of LoG with a minimum scale of 1 and maximum scale of 2

5.3. Finding and Discussion

Scale selection plays a crucial role in extracting connected components (CCs) of handwritten text using scale-space representation methods. The choice of scale significantly impacts the detection of CCs in handwritten document images. The selection of scale and the combination of certain characters significantly influence the determination of threshold value for clustering CCs as text lines.

Ascenders, descenders, open or closed quotes, and writing styles often present challenges in clustering text lines within handwritten document images.

Although Dataset I is relatively simple, the presence of open and closed quotes, along with a small writing style (SWS), causes segmentation errors. Oversegmentation of text lines typically occurs under two conditions: first, when ascenders and descenders are written separately with varying spacing; and second, when the small writing style (SWS) introduces inconsistencies oversegmentation. The cursive wrting style (CSW) and touching characters cause undersegmentation. The proposed method solves overlapping lines, but there is still work to be done for highly skewed lines and mutiple touching lines. In the future, it will be necessary to address the challenges related to highly skewed text lines. multiple touching characters. The text line segmentation of different scale-space representation methods with the proposed algorithm are demonstrated in Figures 16, 17, 18, 19 and 20.

The proposed method is designed for Myanmar and, due to the nature of its features, can be successfully applied to languages of a similar nature. However, it does not work well for other languages. The accuracy of text line extraction algorithms on the Malayalam handwritten document image database, LIPI, is presented in Table 11. It achieves a higher accuracy of 97.97%, compared to 58.19%, 26.7%, and 87.7% for the A* Path Planning algorithm [21], the piecewise painting algorithm [22], and the

horizontal and vertical projection method, respectively, on the LIPI database. The proposed algorithm is also effective in extracting overlapping and short text lines from Malayalam handwritten document images in the LIPI database.

Table 11: Comparison of accuracy obtained for different existing text line methods and the proposed method on LIPI database

No	Algorithm for Text Line Extraction	No. of Correctly Segmented Text Lines	Accuracy (%)
1	A* Path Planning	3258	58.19
2.	Piecewise Painting	1495	26.7
3	Horizontal and Vertical Projection	4912	87.7
4	Proposed Method	5285	97.97

6. Conclusion

Text line extraction from handwritten documents is challenging because of the different handwriting styles. The proposed system addresses overlapping of text lines in extracted segments and varying gaps between characters due to the different handwriting styles, particularly when descenders and ascenders are written below one another, which can lead to incorrect segmentation of a single line into two. The input handwritten image is extracted as connected characters with scale-space technique and CCA. These connected characters are merged into text line using the proposed clustering algorithm. The system resolves these issues, achieving 93.27% and 95.09% match between extracted text lines and ground truth lines from Dataset I and 96.21% and 89.90% on Dataset II, as evaluated using the Pixel IU and Line IU metrics. Myanmar handwritten datasets for text line segmentation have created 405 images, and ground truth images for 6825 text lines. The proposed method is the first phase in digitizing handwritten document images of undergraduate Myanmar students. In the future, text recognition of the handwritten image will be performed on deep learning techniques.

Conflict of Interest

The authors declare no conflict of interest.

Author Contribution

The major portion of the work presented in this paper was carried out by the first author, Nilar Phyo Wai, under the supervision of the second author, Nu War also performed the data analysis, implementation, validation, and preparation of the manuscript.

Acknowledgment

I would like to thank Dr. Nu War, Professor of the Faculty of Computer Systems and Technologies at Myanmar Institute of Information Technology (MIIT), Mandalay, for her continuous guidance, support, and suggestions.

Conflict of Interest

The authors declare no conflict of interest.

References

[1] I. Sanasam, P. Choudhary, K.M. Singh, "Line and word segmentation of handwritten text document by mid-point detection and gap trailing," Multimedia Tools and Applications, **79**(41–42), 30135–30150, 2020, doi:10.1007/s11042-020-09416-1.

[2] X. Zhang, L. Duan, L. Ma, J. Wu, "Text extraction for historical tibetan document images based on connected component analysis and corner point detection," Communications in Computer and Information Science, **772**, 545–555, 2017, doi:10.1007/978-981-10-7302-1_45.

[3] X. Han, H. Yao, G. Zhong, "Handwritten text line segmentation by spectral clustering," Eighth International Conference on Graphic and Image Processing (ICGIP 2016), **10225**(Icgip 2016), 102251A, 2017, doi:10.1117/12.2266982.

[4] A. Fawzi, M. Pastor, C.D. Martínez-Hinarejos, "Baseline detection on Arabic handwritten documents," DocEng 2017 - Proceedings of the 2017 ACM Symposium on Document Engineering, 193–196, 2017, doi:10.1145/3103010.3121037.

[5] B.K. Barakat, R. Cohen, A. Droby, I. Rabaev, J. El-Sana, "Learning-free text line segmentation for historical handwritten documents," Applied Sciences (Switzerland), **10**(22), 1–19, 2020, doi:10.3390/app10228276.

[6] K. Sun, T. Liu, L. Zhang, M. Hao, "Handwritten Manchu Historical Document Segmentation with Anisotropic Gaussian Kernel," Proceedings - 2022 Chinese Automation Congress, CAC 2022, **2022**-Janua, 727–731, 2022, doi:10.1109/CAC57257.2022.10055732.

[7] P. P V, D. Sankar, "Handwriting-Based Text Line Segmentation from Malayalam Documents," Applied Sciences (Switzerland), 13(**17**), 2023, doi:10.3390/app13179712.

[8] Z. Li, W. Wang, Y. Chen, Y. Hao, "A novel method of text line segmentation for historical document image of the uchen Tibetan," Journal of Visual Communication and Image Representation, **61**, 23–32, 2019, doi:10.1016/j.jvcir.2019.01.021.

[9] B.K. Barakat, A. Droby, R. Alaasam, B. Madi, I. Rabaev, R. Shammes, J. El-Sana, "Unsupervised deep learning for text line segmentation," Proceedings - International Conference on Pattern Recognition, (d), 2304–2311, 2020, doi:10.1109/ICPR48806.2021.9413308.

[10] Q.N. Vo, S.H. Kim, H.J. Yang, G.S. Lee, "Text line segmentation using a fully convolutional network in handwritten document images," IET Image Processing, **12**(3), 438–446, 2018, doi:10.1049/iet-ipr.2017.0083.

[11] F.C. Fizaine, P. Bard, M. Paindavoine, C. Robin, E. Bouyé, R. Lefèvre, A. Vinter, "Historical Text Line Segmentation Using Deep Learning Algorithms: Mask-RCNN against U-Net Networks," Journal of Imaging, **10**(3), 2024, doi:10.3390/jimaging10030065.

[12] A. Nyein, H. Khaung Tin, "Handwritten Myanmar Character Recognition System using the Otsu's Binarization Algorithm," 2021, doi:10.4108/eai.27-2-2020.2303219.

[13] B. Barakat, A. Droby, M. Kassis, J. El-Sana, "Text line segmentation for challenging handwritten document images using fully convolutional network," Proceedings of International Conference on Frontiers in Handwriting Recognition, ICFHR, 2018-August, 374–379, 2018, doi:10.1109/ICFHR-2018.2018.00072.

[14] P. Shivakumara, T. Jain, U. Pal, N. Surana, A. Antonacopoulos, T. Lu, "Text line segmentation from struck-out handwritten document images," Expert Systems with Applications, 210(July 2021), 118266, 2022, doi:10.1016/j.eswa.2022.118266.

[15] J. Sklansky, "Finding the convex hull of a simple polygon," Pattern Recognition Letters, **1**(2), 79–83, 1982, doi:10.1016/0167-8655(82)90016-2.

[16] A. Benevento, F. Durante, "Correlation-based hierarchical clustering of time series with spatial constraints," Spatial Statistics, **59**(April 2023),

100797, 2024, doi:10.1016/j.spasta.2023.100797.

[17] N. Xu, R.B. Finkelman, S. Dai, C. Xu, M. Peng, "Average Linkage Hierarchical Clustering Algorithm for Determining the Relationships between Elements in Coal," ACS Omega, 6(**9**), 6206–6217, 2021, doi:10.1021/acsomega.0c05758.

[18] C. Clausner, S. Pletschacher, A. Antonacopoulos, "Aletheia - An advanced document layout and text ground-truthing system for production environments," Proceedings of the International Conference on Document Analysis and Recognition, ICDAR, 48–52, 2011, doi:10.1109/ICDAR.2011.19.

[19] M. Daszykowski, B. Walczak, "2.26 - Density-Based Clustering Methods," Comprehensive Chemometrics: Chemical and Biochemical Data Analysis, Second Edition: Four Volume Set, **2**, 565–580, 2020, doi:10.1016/B978-0-444-64165-6.03005-6.

[20] F. Simistira, M. Bouillon, M. Seuret, M. Wursch, M. Alberti, R. Ingold, M. Liwicki, "ICDAR2017 Competition on Layout Analysis for Challenging Medieval Manuscripts," Proceedings of the International Conference on Document Analysis and Recognition, ICDAR, **1**, 1361–1370, 2017, doi:10.1109/ICDAR.2017.223.

[21] O. Surinta, M. Holtkamp, F. Karabaa, J.P. Van Oosten, L. Schomaker, M. Wiering, "A Path Planning for Line Segmentation of Handwritten Documents," Proceedings of International Conference on Frontiers in Handwriting Recognition, ICFHR, **2014-Decem**, 175–180, 2014, doi:10.1109/ICFHR.2014.37.

[22] A. Alaei, U. Pal, P. Nagabhushan, "A new scheme for unconstrained handwritten text-line segmentation," Pattern Recognition, 44(**4**), 917–928, 2011, doi:10.1016/j.patcog.2010.10.014.

Advances in Science, Technology and Engineering Systems Journal Vol. 10, No. 1, 60-74 (2025)

www.astesj.com

ASTESJ

ISSN: 2415-6698

Selection of Rotor Slot Number in 3-phase and 5-phase Squirrel Cage Induction Motor; Analytic Calculation

Gábor Kovács *

Ganz Electric Works, 1095 Budapest, Hungary

ARTICLE INFO

Article history:
Received:20 November, 2024
Revised: 22 January, 2025
Accepted: 23 January, 2025
Online: 07 February, 2025

Keywords:
Induction motor
Squirrel cage
Rotor slot number
5-phase induction motor
Space harmonics
Synchronous parasitic torques
Radial magnetic force
Oscillating torques
Torque ripple

ABSTRACT

With the spread of inverters, the attention of designers naturally turned to 5-phase motors, due to their advantageous properties. In this regard, perhaps the most important issue in the design of such machines is the selection of the correct rotor slot number. Many articles have been published on multiphase machines, however, only few of them deal with the rotor slot number. Although very useful results are achieved, the result is not comprehensive, systematic approach still awaits. In this paper, the behavior of the full range of 3-phase machines is calculated by using our formulas developed before, and then the method is simply transferred to 5-phase. The point is that relative rotor slot numbers are applied therefore the results are valid for any pole number on a comprehensive way. Detailed, well established design rules are provided. For better understanding of the process, the behavior of the oscillating torques generated by the synchronous parasitic torques during run-up and operation will be presented, using the equations of the unified electric machine theory. During the noise calculation, the concept of the Noise Component Equivalence Measure is introduced, which enables an accurate comparative calculation of the spectra of the radial force waves that excite the noise; it provides the final, comprehensive criteria for the selection of the right rotor slot number. With the study, the entire range of the slot number of any rotor mounted in any stator with any number of poles and number of slots is covered.

1. Introduction

The electrical machine designers noticed from the very beginning, that the MMF space harmonics occurring in the machine, and within that the harmonics created by the number of rotor slots, are of decisive importance for the machine's torque-speed characteristic curve, that means the resulting synchronous parasitic torques and the radial magnetic forces, the latter being the fundamental cause of noise generation.

Synchronous parasitic torques and radial magnetic forces, however, have always been examined separately, as the forced, namely "proportional" physical relationship between the two phenomena has not been recognized. The fact is, which slot number is prohibited or recommended from one point of view, it will also be from the other point of view and vice versa.

Numerous studies are cited at the end of the article as examples of today's research directions. Several articles deal with the issue of noise [1]-[4], others research the effect on the torque characteristic [5], [6]. A wide range of works investigate the multiphase machines, only a few works are highlighted here [3], [7]-[9]. Intensive research is also underway in order to clarify the fundamental laws of the torque ripple [10]-[12].

All these works achieve serious results with the help of significant apparatus. However, as far as the correct rotor slot number is concerned, each result only applies to a certain unique slot number *combination*, generality is lacking. Based on the investigations and tests carried out, so-called *slot number rules* were formulated, namely always for a ready stator. The basis of the phenomenon according to which every induction machine behaves in a way determined by the number of the rotor slots, the role of the number of the stator slot is only that it amplifies certain elements through its slot harmonics, has not appeared anywhere so far.

Our approach, however, so far and this time on is just the opposite, we *start from the rotor slot number* and then see what happens if that rotor will be installed in different stators. This is the way to achieve the general, comprehensive results below.

This paper is a synthetic, summary work, it strongly relies on our previous works, as a completion, in order to achieve the final

*Corresponding Author: Gábor Kovács, Ganz Electric Works, Hungary, gabor.kovacs.ganz@gmail.com

https://dx.doi.org/10.25046/aj100107

goal, the right selection of the rotor slot number, therefore each of them should be put on the reference list ([13]-[18]).

Formulas not existed before were derived in [13], [15] and [18]. A general investigation on the influence of the relative rotor slot number on the behavior of the machine was carried out by using the new formulas in [14]. Detailed investigation was provided regarding parasitic torques and radial magnetic forces in [16] and [17]. The mutual correspondence of our formulas for the synchronous parasitic torques and the radial magnetic forces was proved also in [16], proving for the first time the direct link between the two phenomena. Experimental validation of the formula regarding synchronous parasitic torques was provided with the tests made by others in [17]. The effect of slot skew was investigated and new formulas were provided in [18].

The entire research is based on [19] as the very basic work of the electrical machine science history.

The tables for the three-phase machine developed before are now filled in by using our formulas with values of a "typical motor". The introduction of the "typical motor" also contributed to the comprehensive approach, since in practice the relative breakdown torque and the relative starting current only move within a narrow band, consequently the reactance in p.u. are almost the same for any machine, for the entire range.

The procedure is then simply applied to the harmonics generated by the stator of 5-phase machines.

The 5-phase machines are powered almost exclusively via an inverter, where the synchronous parasitic torque occurring either in the motoric, in braking range or in standstill is of no importance; the ranges they appear in do not need to be distinguished. However, it is important that all of these appear as oscillating torques in operation, further no matter appearing in motoric or break range or in standstill, they cause radial magnetic forces of r=0 order.

It is simpler to formulate the aspects and performing the calculation for synchronous parasitic torques, therefore that investigation will be performed first. Then, in the second part of the study, it will be turned to the radial magnetic forces.

In the absence of our formulas developed before, the investigations carried out so far were forced to concentrate only on the expectedly dangerous frequencies and on how to avoid the coincidence, or to get involved in the use of large apparatus. However, now, relying on our formula, we have the opportunity to define and introduce what we call the Noise Component Equivalence Measure (NCEM). This metric made it possible to accurately calculate the comparative spectra of the complete, noise-exciting radial forces. Until now, such a method, such a table, which is more suitable than ever, yet very simple, which actually enables the design engineer to select the most favorable rotor slot number, indeed, has not been available.

As a model, such a machine was assumed for which the basic formulas for determining the resulting harmonics are valid [20]: infinite relative permeability, two-dimensional fields without considering boundary and end effects, the machine consist of two smooth coaxial cylinders made of magnetic material, the cylinders are separated by the air gap, the conductors of infinitely small cross-section are located in the air gap. Harmonics of other origin were not involved. See Appendix for details. Since the derivations as well as the conclusions that can be drawn from the model are based on the fundamental laws of electrical engineering, they do not require validation.

2. Calculation of Synchronous Parasitic Torques and Radial Magnetic Forces

Order of harmonics by definition see Appendix:

$$\nu_a = 2mg_1 + 1; \quad \mu_a = e\,Z_2/p + \nu_a = e\cdot 2mq_2' + \nu_a \tag{1a}$$

$$\nu_b = 2mg_2 + 1 \tag{1b}$$

where

ν_a ,ν_b ,μ_a harmonic order numbers stator, rotor
e, g_1, g_2 different integers: 0, ±1, ±2, ±3 …
m number of phases
Z_1, Z_2 slot numbers stator, rotor
2p pole number
q_1, q_2' relative slot numbers: slot number per phase per pole, stator / rotor

The formula for the calculation of the synchronous torque, which was first derived by us ([13] (13)):

$$\frac{M_{synchronous}}{M_{breakdown}} = \frac{X_m}{X_s}\cdot 2\sum \frac{\xi_{1\nu_a}\xi_{1\nu_b}}{\mu_a}\eta_{2\nu_a}^2\frac{1}{\xi_1^2} \tag{2}$$

where

$$\eta_{2\nu} = \frac{\sin\nu\frac{p\pi}{Z_2}}{\nu\frac{p\pi}{Z_2}} = \frac{\sin\nu\frac{\pi}{2mq_2'}}{\nu\frac{\pi}{2mq_2'}}$$

M torque
X_m, X_s reactance, magnetizing, leakage
ξ_{1va} , ξ_{1vb} , ξ_1 winding factor of harmonics, of fundamental harmonic
$\eta_{2\nu}^2$ Jordan's coupling factor [19] (258b)

The formulas for calculation of radial magnetic forces also first derived by us [13] (25), (26):
Radial magnetic force wave r=0, 2, 3,…

$$f = \frac{W_m}{\left(V_{airgap}/2\right)}C \quad [\mathrm{N/m^2}] \tag{3a}$$

One sided magnetic pull

$$F_{r=1} = \frac{W_m}{\delta'}C \quad [\mathrm{N}] \tag{3b}$$

where the proportionality factor C is

$$C = \frac{\xi_{1\nu_b}\xi_{1\nu_a}}{\nu_b\mu_a}\eta_{2\nu_a}^2\frac{1}{\xi_1^2} \tag{3c}$$

W_m magnetic energy of the machine
V volume of airgap
δ' equivalent airgap

It is worth repeating our diagram developed in [14], which shows the change of the core element of the calculation $\eta_{2\nu}^2$ in a very visual way. It shows how much the rotor responds to a stator

harmonic. A zero or very low value indicates that the rotor does not respond to that harmonic.

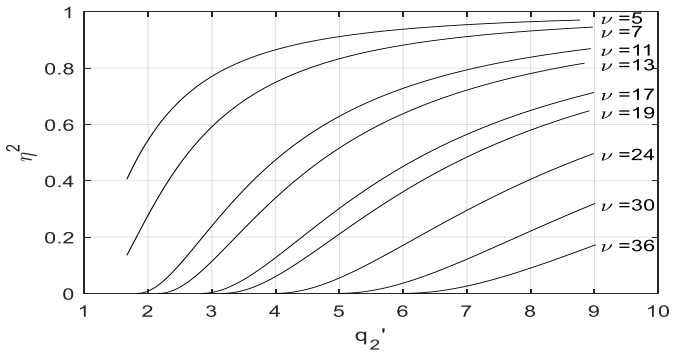

Figure 1: Representation of the value of $\eta_{2\nu}^2$ as a function of q_2' with ν as a parameter, for 3-phase machines. Higher odd harmonics are replaced mathematically by adjacent (actually with 3-phase not existing) even harmonics only for better transparency.

3. Synchronous Parasitic Torques and Radial Magnetic Forces in Three-Phase Machines

The rotor slot numbers resulting in a significant synchronous parasitic torque in the three-phase machine were presented in [16] Table III.A and those creating force waves of order r = 0 – 4 in [16] Table IV. Although the tables were elaborated independently of each other, still they clearly show the correlation between the parasitic torques and the force waves with order number r=0. These tables are not repeated here due to space limitations.

Now, using the new formulas a number of tables have been created like Table 1. for a wide range of relative rotor slot numbers. In order to make it easier for the Reader to follow, a simplification and approximation $\xi_{1a}\cdot\eta_{2\nu}^2/\xi_1^2\approx 1$ is considered, since only the quantities produced by the fundamental harmonic are considered for the moment: $\nu_a = 1$; this is generally a legitimate approximation [14] Figure 4. A machine with typical characteristics of $X_m/X_s=15$ was taken as basis with $X_m=3$ p.u., $X_s=0.2$ p.u., with this values M_{break} is usually ≈ 2 p.u. . The oscillating torque was calculated by the synchronous torque divided by the square of the value $I_{starting}/I_{rated} = 5$.

Thus the formulas applied:

$$\frac{M_{synchronous}}{M_{breakdown}} = 15 \cdot 2 \frac{\xi_{1\nu_b}}{\mu_a} \tag{4a}$$

$$C = \frac{\xi_{1\nu_b}}{\mu_a^2} \tag{4b}$$

Then these tables were summarized in a *single table* in Table 2. representing the *point of subject development*. For space limitation only those relative rotor slot numbers were included in Table 2. which are possible in a 4 pole machine excl. odd rotor slot numbers.

After that, it was easy to enter the evaluation of the individual rotor slot numbers. The obviously prohibited slot numbers were marked in red, the recommended ones in green, and the slot numbers that are permitted under certain conditions (suitably high torque characteristics of the machine during start-up) in yellow. Torques in brake range were not included in the evaluation. The limit of the classification was defined as the synchronous parasitic torque is approx. 0.25times breakdown torque. This means 1% for oscillating torques. In the case of a high power motor, this limit must be reduced. While the torques are real values, the C factor is only a proportionality factor, the actual force obviously depends from the size.

It is emphasized that the table includes each relative rotor slot number possible at 4 pole and due to working with relative slot numbers, relative synchronous torques, relative proportionality factors and data of a typical motor the table is valid for any motor, with any pole number (consider the relation 2mq=Z/p). The entire system could not have been built if the parasitic torque was not related to the breakdown torque at the beginning, when the formula itself was derived.

For a certain q_2' listed in Table 2 the machine's behavior and data are *numerically identical* on any pole number; this refers for the evaluation as well. Therefore, Table 2. *comprehensively* covers the entire range of three-phase asynchronous machines as a whole. At pole numbers higher than 4, all that happens is that

Table 1: Harmonics, Oscillating Torques and Radial Magnetic Force Waves of a Three-Phase Machine for a Relative Rotor Slot Number q_2'= 2 1/3.

m=		**3**	ν_b			q_1			ξ_b			Synchronous Torque / Breakdown Torque			Oscillating Torque / Breakdown Torque %			C proportionality factor for radial magnetic force wave density f[N/m²] *10000			C proportionality factor for radial magnetic force wave density f[N/m²] *10000 in dB		
q_2	p/r	e	$\nu_b=-\mu_a$	$\nu_b=\mu_a$	operation	q_1=2	q_1=3	q_1=4	q_1=2	q_1=3	q_1=4	q_1=2	q_1=3	q_1=4	q_1=2	q_1=3	q_1=4	q_1=2	q_1=3	q_1=4	q_1=2	q_1=3	q_1=4
2	**1/3**	-1	13		motoric	ξ_{slot}			-0,966	0,218	0,126	-2,23	0,50	0,29	-8,92	2,01	1,16	-57,16	12,87	7,46	17,57	11,10	8,73
		2	-29		break				0,259	-0,177	-0,205	-0,27	0,18	0,21	-1,07	0,73	0,85	3,08	-2,11	-2,44	4,88	3,24	3,88
		-3		-41	standstill				-0,259	0,218	-0,158	≈0	≈0	≈0	≈0	≈0	≈0	≈0	≈0	≈0	≈0	≈0	≈0
		3		43					0,259	-0,177	0,205												
		-4	55		motoric		ξ_{slot}		-0,259	0,960	-0,158	-0,14	0,52	-0,09	-0,56	2,09	-0,34	-0,86	3,17	-0,52	-0,68	5,01	-2,83
		5	-71		break	ξ_{slot}	ξ_{slot}	ξ_{slot}	0,966	0,960	-0,958	-0,41	-0,41	0,40	-1,63	-1,62	1,62	1,92	1,90	-1,90	2,82	2,80	2,79
		-6		-83	standstill	ξ_{slot}			-0,966	-0,177	0,126	0,35	≈0	≈0	1,40	≈0	≈0	-1,40	≈0	≈0	1,47	≈0	≈0
		6		85					-0,966	0,218	-0,126	-0,34			-1,36			-1,34			1,26		
		-9		-125	standstill		ξ_{slot}		0,259	0,960	-0,205	≈0	-0,23	≈0	≈0	-0,92	≈0	≈0	0,61	≈0	≈0	-2,12	≈0
		9		127					-0,259	0,960	0,158		0,23			0,91			0,60			-2,25	
		-12		-167	standstill	ξ_{slot}		ξ_{slot}	0,966	0,218	-0,958	-0,17	≈0	0,17	-0,69	≈0	0,69	0,35	≈0	-0,34	-4,60	≈0	-4,64
		12		169					0,966	-0,177	-0,958	0,17		-0,17	0,69		-0,68	0,34		-0,34	-4,71		-4,75

further relative rotor slot numbers like "+1/9q", "+1/12q", "1/4q" etc. become possible, the table is easy to supplement with them by creating further tables like Table 1. with a little investment of time; at high pole numbers and/or high phase numbers, odd slot numbers do not necessarily have to be ruled out.

Table 2: Largest Synchronous Torques, Oscillating Torques and the Largest Proportionality Factors of the Radial Magnetic Force Waves for a Three-Phase Machine

Relative rotor slot number q_2'	Operation	Synchronous Torque / Breakdown Torque			Oscillating Torque / Breakdown Torque %			C proportionality factor for radial magnetic force wave density f[N/m^2]·10000		
		q_1=2	q_1=3	q_1=4	q_1=2	q_1=3	q_1=4	q_1=2	q_1=3	q_1=4
q_1-2+**2/3**	motor	x	1,52	0,15	x	6,06	0,61	x	26,59	1,64
	brake		0,48	0,28		1,93	1,11		14,66	5,45
	standstill		0,64	1,20		2,56	4,80		2,37	8,33
q_1-2+**5/6**	motor	x	0,26	0,17	x	1,06	0,68	x	0,96	0,46
	brake		0,32	0,11		1,29	0,43		4,11	1,03
	standstill		0,29	0,00		1,16	0,00		0,49	0,00
q_1-1+**1/6**	motor	2,23	0,21	0,10	8,92	0,85	0,41	57,16	2,84	0,92
	brake	0,41	0,54	0,08	1,63	2,17	0,32	3,08	3,42	0,35
	standstill	0,68	0,24	0,00	2,72	0,96	0,00	2,74	0,35	0,00
q_1-1+**1/3**	motor	1,11	0,52	0,32	4,44	2,09	1,30	52,8	12,87	5,69
	brake	0,46	0,41	0,12	1,83	1,62	0,46	8,96	2,11	0,94
	standstill	2,42	0,46	0,48	9,68	1,84	1,92	33,70	1,21	1,33
q_1+**2/3**	motor	0,25	0,12	0,09	1,00	0,49	0,34	2,69	0,96	0,52
	brake	0,46	0,32	0,21	1,83	1,29	0,85	8,96	4,11	2,44
	standstill	1,21	0,22	0,34	4,84	0,88	1,36	8,39	0,30	0,68
q_1+**5/6**	motor	0,17	0,32	0,05	0,69	1,27	0,21	0,58	1,16	0,16
	brake	0,83	0,11	0,06	3,31	0,45	0,26	7,89	0,80	0,36
	standstill	0,28	0,00	0,00	1,12	0,00	0,00	0,46	0,00	0,00

Table 2. does not include the magnitude of the asynchronous parasitic torque. Consider the formula also derived by us first [15] (19)

$$\frac{M_{break\nu}}{M_{break}} = \frac{X_m}{X_s}\frac{\xi_\nu^2}{\xi_1^2}\frac{\eta_{2\nu}^2}{\nu} \tag{5}$$

Considering Figure 1. it is clear that if $Z_2<Z_1$, or if $Z_2>Z_1$, but according to practice is not much larger, then there is no need to deal with asynchronous parasitic torque because $\eta_{2\nu}^2$ is zero or very small. In extreme cases, (5) must be used, but we will not deal with such a rare case here. Nevertheless, machines with q_1=2 and q_2'>q_1 might suffer because of this phenomenon.

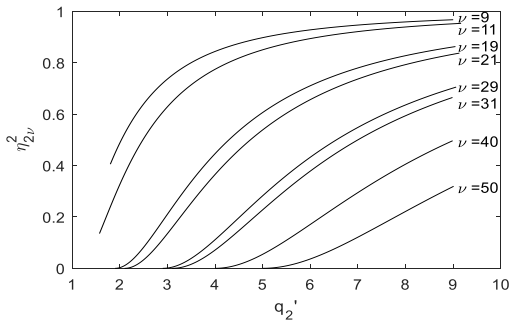

Figure 2: Representation of the value of $\eta_{2\nu}^2$ as a function of q_2' with ν as a parameter, for 5-phase machines. Higher odd harmonics are replaced mathematically by adjacent (actually with 5-phase not existing) even harmonics only for better transparency.

4. Synchronous Parasitic Torques and Radial Magnetic Forces in Five-Phase Machines

The study of this paragraph is started with Figure 2. showing the value of $\eta_{2\nu}^2$ as a function of q_2' with ν as a parameter defined for 5-phase machines, just for reference. It is not surprising that the figure is very similar to Figure 1.

The 5-phase machines are powered almost exclusively via an inverter, where the synchronous parasitic torque is of no importance. However, it is important that all of these appear as oscillating torques in operation and as a consequence radial magnetic forces appear at the same time influencing vibration and noise on the same way as in net-supplied machines. Therefore motors for inverter shall be designed that means the rotor slot number must be selected as if it were a mains powered motor with constant (rated) speed.

4.1. Slot numbers creating considerable synchronous parasitic torques

It was seen that, especially in machines with chording, the effect of higher ν_a harmonics is small. And in the case of 5-phase machines, since the first harmonics are already -9 and 11 instead of -5 and 7, their effect will be negligible even in non-chorded machines. Therefore, rotor harmonics created by the fundamental stator harmonic will be considered only.

$$\nu_a = 10g_1 + 1 \quad \rightarrow \quad \nu_a = 1, \tag{6a}$$
$$\nu_b = 10g_2 + 1 \quad \rightarrow \quad \nu_b = 1, -9, 11, 19, 21, -29, 31 \ldots \tag{6b}$$
$$\mu_a = e \cdot Z_2/p+1 = e \cdot 2mq_2' + 1 \tag{6c}$$

Compared with the harmonics of a three-phase machine, it can be seen that higher order numbers occur in the ratio of 5/3 in the five-phase machine. Therefore, it is expected that both its oscillating torque and radial magnetic force waves will be smaller; therefore it will be easier to find an ideal rotor slot number between the fewer prohibited ones.

In Table 3., the rotor slot numbers for the pole numbers 2p = 4 – 8, which generate significant synchronous torques are specified.

The tables show that the most critical slot numbers are: q_2'=integer, q_2'=q_2±1/5 obtained by e=±1.

4.2. Slot numbers creating considerable radial magnetic forces

The rotor slot numbers creating considerable (that means low order) radial magnetic forces are given in Table 4. As seen those ones given in 4.1 create significant radial magnetic forces of order number r=0. The slot numbers that appear in the same row result in radial magnetic forces with the same magnitude, due to $\xi_{1\nu b}$ is identical and differences in μ_a and ν_b with r= 1 – 4 are negligible.

The natural frequencies of the actual machine can be checked with the reported frequencies. These frequencies were calculated now with 50 Hz "rated" frequency.

In Table IV. of [16] referring to 3-phase 4 pole machines, the rotor slot ranges belonging to a certain q_1 "touched" each other that means there was no rotor slot number that does not generate radial magnetic forces with low order number. Here, however, *there are* rotor slot numbers between the ranges belonging to two adjacent q_1 without this harmful effect. At large machines,

however, where r=5, 6 matter, the table must be supplemented by those columns, then each rotor slot number will again generate low-order radial magnetic force wave.

Table 3: Rotor Slot Numbers that Create Considerable Synchronous Parasitic Torques for a Five-Phase Machine

m	5			p=	2				
				e=		e=		e=	
				-1	1	-2	2	-3	3
q_1	Z_1	$\mu_a = \nu_b$	$\mu_a = -\nu_b$						
1	20	-9		**20**		**10**			
			9		**16**		**8**		
		11			**20**		**10**		
			-11	**24**		**12**		**8**	
2	40	-19		**40**		**20**			
			19		**36**		**18**		**12**
		21			**40**		**20**		
			-21	**44**		**22**			
3	60	-29		**60**		**30**		**20**	
			29		**56**		**28**		
		31			**60**		**30**		**20**
			-31	**64**		**32**			
4	80	-39		**80**		**40**			
			39		**76**		**38**		
		41			**80**		**40**		
		-41	-41	**84**		**42**		**28**	

m	5			p=	3				
				e=		e=		e=	
				-1	1	-2	2	-3	3
q_1	Z_1	$\mu_a = \nu_b$	$\mu_a = -\nu_b$						
1	30	-9		**30**		**15**		**10**	
			9		**24**		**12**		**8**
		11			**30**		**15**		**10**
			-11	**36**		**18**		**12**	
2	60	-19		**60**		**30**		**20**	
			19		**54**		**27**		**18**
		21			**60**		**30**		**20**
			-21	**66**		**33**		**22**	
3	90	-29		**90**		**45**		**30**	
			29		**84**		**42**		**28**
		31			**90**		**45**		**30**
			-31	**96**		**48**		**32**	
4	120	-39		**120**		**60**		**40**	
			39		**114**		**57**		**38**
		41			**120**		**60**		**40**
			-41	**126**		**63**		**42**	

m	5			p=	4				
				e=		e=		e=	
				-1	1	-2	2	-3	3
q_1	Z_1	$\mu_a = \nu_b$	$\mu_a = -\nu_b$						
1	40	-9		**40**		**20**			
			9		**32**		**16**		
		11			**40**		**20**		
			-11	**48**		**24**		**16**	
2	80	-19		**80**		**40**			
			19		**72**		**36**		**24**
		21			**80**		**40**		
			-21	**88**		**44**			
3	120	-29		**120**		**60**		**40**	
			29		**112**		**56**		
		31			**120**		**60**		**40**
			-31	**128**		**64**			
4	160	-39		**160**		**80**			
			39		**152**		**76**		
		41			**160**		**80**		
			-41	**168**		**84**		**56**	

Table 4: Force Wave Order Numbers Created by the Given Rotor Slot Numbers and the Frequencies of the Wave, for Five Phases; Supply Frequency 50 Hz

m=	5			p=	2										
				r=	0	r=	1	r=	2	r=	3	r=	4		
				+	-	+	-	+	-	+	-	+	-		
q_1	Z_1	ν_b	ν'_b												
2	40	-19	-38	**36**	**40**	**37**	**41**	**38**	**42**	**39**	**43**	**40**	**44**		
		frequency Hz		1000	1000	1025	1025	1050	1050	1075	1075	1100	1100		
			e=±2	**18**	**20**			**19**	**21**			**20**	**22**		
			e=±3	**12**					**13**						
		-19	-38	**36**	**40**	**35**	**39**	**34**	**38**	**33**	**37**	**32**	**36**		
		frequency Hz		1000	1000	975	975	950	950	925	925	900	900		
			e=±2	**18**	**20**			**17**	**19**			**16**	**18**		
			e=±3	**12**			**13**			**11**			**12**		
		21	42	**44**	**40**	**45**	**41**	**46**	**42**	**47**	**43**	**48**	**44**		
		frequency Hz		1000	1000	1025	1025	1050	1050	1075	1075	1100	1100		
			e=±2	**22**	**20**			**23**	**21**			**24**	**22**		
			e=±3			**15**			**14**			**16**			
		21	42	**44**	**40**	**43**	**39**	**42**	**38**	**41**	**37**	**40**	**36**		
		frequency Hz		1000	1000	975	975	950	950	925	925	900	900		
			e=±2	**22**	**20**			**21**	**19**			**20**	**18**		
			e=±3				**13**	**14**					**12**		
3	60	-29	-58	**56**	**60**	**57**	**61**	**58**	**62**	**59**	**63**	**60**	**64**		
		frequency Hz		1500	1500	1525	1525	1550	1550	1575	1575	1600	1600		
			e=±2	**28**	**30**			**29**	**31**			**30**	**32**		
			e=±3		**20**	**19**					**21**	**20**			
		-29	-58	**56**	**60**	**55**	**59**	**54**	**58**	**53**	**57**	**52**	**56**		
		frequency Hz		1500	1500	1475	1475	1450	1450	1425	1425	1400	1400		
			e=±2	**28**	**30**			**27**	**29**			**26**	**28**		
			e=±3		**20**			**18**							
		31	62	**64**	**60**	**65**	**61**	**66**	**62**	**67**	**63**	**68**	**64**		
		frequency Hz		1500	1500	1525	1525	1550	1550	1575	1575	1600	1600		
			e=±2	**32**	**30**			**33**	**31**			**34**	**32**		
			e=±3		**20**			**22**			**21**				
		31	62	**64**	**60**	**63**	**59**	**62**	**58**	**61**	**57**	**60**	**56**		
		frequency Hz		1500	1500	1475	1475	1450	1450	1425	1425	1400	1400		
			e=±2	**32**	**30**			**31**	**29**			**30**	**28**		
			e=±3		**20**	**21**					**19**	**20**			
4	80	-39	-78	**76**	**80**	**77**	**81**	**78**	**82**	**79**	**83**	**80**	**84**		
		frequency Hz		2000	2000	2025	2025	2050	2050	2075	2075	2100	2100		
			e=±2	**38**	**40**			**39**	**41**			**40**	**42**		
			e=±3												
		-39	-78	**76**	**80**	**75**	**79**	**74**	**78**	**73**	**77**	**72**	**76**		
		frequency Hz		2000	2000	1975	1975	1950	1950	1925	1925	1900	1900		
			e=±2	**38**	**40**			**37**	**39**			**36**	**38**		
			e=±3			**25**			**26**			**24**			
		41	82	**84**	**80**	**85**	**81**	**86**	**82**	**87**	**83**	**88**	**84**		
		frequency Hz		2000	2000	2025	2025	2050	2050	2075	2075	2100	2100		
			e=±2	**42**	**40**			**43**	**41**			**44**	**42**		
			e=±3				**27**								
		41	82	**84**	**80**	**83**	**79**	**82**	**78**	**81**	**77**	**80**	**76**		
			frek Hz	2000	2000	1975	1975	1950	1950	1925	1925	1900	1900		
			e=2	**42**	**40**			**41**	**39**			**40**	**38**		
			e=3						**26**						

Still due to space limitations, the table is published here only for 4 poles and only for relative stator slot numbers q_1=2, 3, 4. However, this will *not* be sufficient for a complete analysis, it is necessary to reveal all the cases where a certain rotor slot number to be examined and any integer multiple of it appears anywhere, therefore the missing table parts q_1=1, 5... are also necessary; nevertheless they can be easily created based on the sample with

Table 5: Harmonics, Oscillating Torques and Radial Magnetic Force Waves of a Five-Phase Machine for a Relative Rotor Slot Number q_2'= 2 1/5

m		5	ν_b			q_1			ξ_b			Synchronous Torque / Breakdown Torque			Oscillating Torque / Breakdown Torque %			C proportionality factor for radial magnetic force wave density f[N/m^2] *10000		
q_2	p/r	e	ν_b=-μ_a	ν_b=μ_a	operation	q_1=2	q_1=3	q_1=4	q_1=2	q_1=3	q_1=4	q_1=2	q_1=3	q_1=4	q_1=2	q_1=3	q_1=4	q_1=2	q_1=3	q_1=4
2	**1/5**	-1	21		motoric	ξ_{sslot}			-0,988	0,127	0,077	-1,411	0,182	0,111	-5,64	0,73	0,44	13,50	4,60	2,45
		1	n.a.	n.a.																
		-4	n.a.	n.a.																
		4	-89		break		ξ_{sslot}		0,156	0,985	0,119	-0,053	-0,332	-0,040	-0,21	-1,33	-0,16	-7,04	0,95	-8,23
		-5		-109	standstill				-0,156	-0,113	0,102	0,043	0,031	-0,028	0,00	0	0	0	0	0
		5		111					0,156	0,127	-0,119	0,042	0,034	-0,032						
		-10		-219	standstill	ξslot			-0,988	0,127	0,077	0,135	-0,017	-0,011	0,54	0	0	-6,86	0	0
		10		221					-0,988	-0,113	-0,077	-0,134	-0,015	-0,011	-0,54			-6,94		

a little investment of time, the same was described and already published for 3 phases in [16].

In accordance with Table 1, we also provide in Table 5. below an example for 5-phase on how to calculate the order number of harmonics generated by a certain relative rotor slot number and the values created by it. We stayed with the reactance ratio value of (2) according to section 3, even though it differs from that of a three-phase machine [3], [7]-[9]. On the one hand, the linear conversion to the actual reactance ratio of the machine to be investigated does not cause any problem, on the other hand, the table shows clearly anyway which harmonics $\xi_{1\nu b}=\xi_1$ will apply for, i.e. are slot harmonics, being therefore dangerous and should be avoided. Equation (4b), as a relative number, remains still valid here.

We are not dealing with the speed range in which the parasitic synchronous torque occurs at 5-phase machines: we need them only for calculation of the oscillating torque; here always the largest of them was chosen. The largest value of the proportionality factor C does not necessarily belong to the largest value of the oscillating torque, but - if several torques of a similar magnitude are generated – it belongs to the one produced by the *lowest* order harmonic ν_b. That phenomenon is an important hint regarding noise, because it means that the noise is caused by only few, high noise component created by low order harmonics.

Table 6: Largest Oscillating Torques and the Largest Proportionality Factors of the Radial Magnetic Force Waves for Five-Phase Machines

Relative rotor slot number q_2'	Oscillating Torque / Breakdown Torque %			C proportionality factor for radial magnetic force wave density f [N/m^2] ·10000		
	q_1=2	q_1=3	q_1=4	q_1=2	q_1=3	q_1=4
q_1-2+**9/10**	x	0,78	0,32	x	0,84	0,22
q_1-1+**1/10**	5,64	1,13	0,15	22,40	0,70	0,21
q_1+**9/10**	4,09	0,35	0,19	2,84	0,18	0,08
q_1-2+**4/5**	x	2,63	0,42	x	3,12	1,21
q_1-1+**1/5**	3,95	1,33	1,47	12,93	2,89	1,24
q_1+**4/5**	1,69	0,78	0,98	1,86	0,84	0,5
q_1-2+**7/10**	x	0,49	0,73	x	0,27	0,38
q_1-1+**3/10**	1,50	1,30	0,59	1,58	1,19	0,25
q_1+**7/10**	0,74	0,79	0,42	0,38	0,44	0,12
q_1-2+**3/5**	x	3,81	1,5	x	10,25	1,58
q_1-1+**2/5**	2,89	0,98	0,49	5,88	0,45	0,21
q_1+**3/5**	1,5	1,31	0,13	1,58	0,61	0,12
q_1**±1/2**	≈ 6	≈ 2	≈ 0,5	≈ 10	≈ 0,5	≈ 0,1

A number of tables were created like Table 5. for a wide range of relative rotor slot numbers and then summarized in a single core table in Table 6., again *a point of subject development.*

Again for space limitation only those relative rotor slot numbers were included in Table 6. which are possible in a 4 pole machine. Odd rotor slot numbers remain still disregarded although the situation is not as strong as for 3-phase machines. As it can be seen - and in accordance with the expectations - the 5-phase machines are superior to 3-phase machines with regard to oscillating torques and the radial magnetic force density. However, unlike three-phase machines, we do not introduce here direct evaluation. In the case of a three-phase, mains-fed motor, the start-up, i.e. the *operation* itself becomes questionable or impossible in the case of an inadequate rotor slot number. However, there is no such danger in the case of a 5-phase machine powered by an inverter. In our opinion, however, a limit still should be introduced here as well, let it be again the value of 1% of the oscillating torque. After all, the 5-phase machine is used expressly in the hope of calm operation and less noise as a result of the smaller C proportionality factors. Should the data of the machine creep up into the range of three-phase machines just because the wrong rotor slot number it has no sense anymore to assume the excess costs of a non-standard motor plus an inverter.

As expected corresponding to Table 3, Table 6. shows that the "1/5" – "4/5" machines are the least favorable but "2/5 – 3/5" slot numbers are also better to avoid.

5. Further General Considerations, Selection of Rotor Slot Number

Write down again the rotor harmonics for ν_a=1 expressed by relative rotor slot number q_2':

$$\mu_a = e \cdot 2mq_2' + 1 \qquad (7)$$

where as before

e ±1, ±2, ±3…, integers
$q_2'=q_2+p/r$ with meaning that any relative rotor slot number can always be expressed by an improper fraction
q_2 positive integer
p, r positive integers and p≤r.

Substituting

$$\mu_a = e \cdot 2m(q_2 + \frac{p}{r}) + 1 = e \cdot 2mq_2 + e \cdot 2m\frac{p}{r} + 1 \qquad (8)$$

A necessary (but not sufficient) condition for the generation of synchronous parasitic torque is that μ_a is odd integer and in (8) the sum of the first two terms is even that means the second term is also even.

If we select the rotor slot number such that r=m or p/r=1 ("integer" rotor slot number), then this condition is already satisfied with the lowest value of e: e=±1. This means that with such a selection, the order number of synchronous torques will be as small as possible, and the synchronous torque itself will probably be as high as possible. The term "probably" refers to the fact that the torque still depends on whether $\xi_{1vb} = \xi_1$ or not see (3c), (4a), (4b). The final condition is that μ_a shall be identical to a stator harmonic (1b), (6b). This is fulfilled as above if q_2' = integer or if $q_2' = q_2 \pm 1/m$.

These (dangerous) rotor slot numbers are for 3-phase

$$q_2'=q_2, \quad q_2'=q_2+1/3, \quad q_2'=q_2+2/3 ,$$

for 5-phase

$$q_2'=q_2, \quad q_2'=q_2+1/5, \quad q_2'=q_2-1/5$$

and, regardless of the phase number, even though with e=±2, still the

$$q_2'=q_2+1/2$$

slot numbers.

Staying with the most common practical case that r=m, the maximum torques are generated alternately in braking mode and in motoric operation in three-phase by substitution e=±1 and e=±2, and always in standstill by substitution e=±3, then the same pattern is repeated with further $\underline{e}$ values [17]. The same substitutions e=±1, e=±4 and e=±5 cause the same effect in 5-phase, respectively. In industrial motor, a high torque generated during braking is not a problem. In the case of low-noise machines, no matter net supplied or via inverter, however, where these always produce significant force waves with order number r = 0 and significant oscillating torques, these slot numbers should be avoided at all costs.

Further considerations can be found in [17] Chapter III. G.

5.1. Influence of the phase number

The flux distribution images and animations created by FEM simulations do not show anything about the number of phases of the winding. So, the FEM simulation hides the fact that the influence of the phase number is also included in the circumferential change of the MMF, and that gives the MMF an additional specific periodicity, which is very important from the point of view of the present investigation. This is the case if $q_1>1$, it will be most visible with q_1 integer, full pitch winding. Instead of MMF of each slot differing in phase from the previous one by one slot pitch, like in the rotor, groups of slots consisting of q_1 slots with the same phase follow one after the other. This is the phenomenon which creates a periodicity according to the phase number. In the formulas: in the case of 3 phases, every third odd MMF harmonic is missing or the order numbers of the MMF harmonics are adjacent to every third even number and in the case of 5 phases, to every fifth even number. The rotor slot number must, therefore, be as far away from that periodicity as possible or the torque still created be as low as possible. Periodicity according to the phase number is created when the second term of (8) is an even integer multiple of the phase number; if it is not possible to avoid then as higher multiple as better ($q_2'=q_1$ and q_2'=integer are the worst cases). In such cases only standstill synchronous parasitic torques are created. Further analysis is required for achieving general results.

6. Design rules

The question is examined now in its entirety, using both our previous and current results. The wording is mainly related to 3-phase machines. The recommendations will not apply to individual slot numbers, which would be the approach we do not want, but to bands: recommended, to be avoided and prohibited bands will be defined. These bands sometimes slide into each other, they sometimes represent conflicting recommendations. The wording is corresponding to (8) especially to second term of it. The sequence of considerations shall be:

- the basic law is: it is *the p/r proper fractional part of the relative rotor slot number which determines the behavior of the squirrel cage asynchronous machine*. The denominator $\underline{r}$ determines the dangerousness of the rotor slot number, and the numerator determines the speed range in which the parasitic torque occurs when r=m. Therefore, during the entire investigation, above and below, the rotor slot number is expressed and named in the form of p/r without q_2.

- referring to (4a) and (4b) the lowest possible value of μ_a must be as high as possible. Referring to (8), therefore, the lowest possible value of $\underline{e}$ must be as high as possible; consequently *the value of $\underline{r}$ should be also as high as possible, this is the goal regarding the suitable rotor slot number*. As a default, *only standstill* synchronous parasitic torques are created.

- referring to (8), with p/r=0 (equal to p/r=1) and r=2 (p/r=1/2), however, still unacceptably high synchronous parasitic torques are created therefore they are *forbidden*

- slot numbers that create radial magnetic forces with order number r=1 are prohibited, even if they are created by a ξ_{1vb} non-slotharmonic; *these are always Z_2= odd slot numbers therefore they are forbidden;* even though these would have the advantage of creating only a small, practically negligible synchronous parasitic torque.

- in the case of r=3, 4, 5...acc. to (8), the magnitude of the highest synchronous parasitic torque is decreasing, they are acceptable, in fact, they are particularly low; further: e<r does not create synchronous parasitic torque. *Therefore, these slot numbers are expressly recommended, in fact, they should be selected primarily, but with condition r≠m.* The lowest pole number is 2p=8 where the condition r≠m or r≠integer·m can be met: the slot numbers *recommended* are: 1/4, 3/4.

- additional conditions apply, however, to slot numbers that $\underline{r}$ in (8) is equal to the phase number or multiples thereof: r=m, r=2m, r=3m etc. Per definition: r=m is possible at any pole number. As a matter of fact, in the case of 2p=2, 4, and 6, there is no other option (with the exception of odd slot numbers, which are otherwise prohibited especially at these low pole numbers due to dangerous radial forces of r=1). These slot numbers, in addition to standstill synchronous parasitic torques, create torques *also in rotation*. As a rule for r=m: substitution e=1 and e=-2 or e=-1 and e=2 create synchronous parasitic torques always in rotation; e=±3 (in pair) create in standstill.

Then this pattern repeats itself. Those with e=±1 are large, m times larger than the standstill torques created by e=m=3. Therefore, these slot numbers are to be selected only if there is no other choice, if the slot numbers r≠m are not possible. It should be noted that, despite of this, these are the most frequently used rotor slot numbers, even when there are acc. to the author more favorable options (e.g. in 4 pole).

- Possible slot numbers remaining for 2 pole: 1/3, 2/3, for 4 pole: 1/3, 2/3, 1/6, 5/6; for 6 pole: 1/3, 2/3, 1/9, 2/9, 4/9, 5/9, 7/9, 8/9.
- slot numbers creating the highest torque in the motor range with e=±1 therefore are to be *avoided*: 1/3, 1/6, 1/9, 4/9, 7/9, 1/12, 7/12.
- slot numbers creating the highest torque in the brake range therefore they are *recommended*: 2/3, 5/6, 2/9, 5/9, 8/9, 5/12, 11/12.
- the band q_1-1/2≤q_2'≤q_1+1/2 is *prohibited*, since then the low order radial magnetic forces are created by the $\xi_{1\nu b}$ slotharmonic
- band q_1-1<q_2'<q_1-1+1/2 is rather *not recommended* because the most of the slot numbers (except 2/9, 5/12 …) falling into this band create the highest torque in the motor range
- the remaining bands that may be *recommended*: q_1-2+2/3≤q_2'<q_1-1 and q_1+2/3≤q_2'<q_1+1 bands because the slot numbers falling into this band create the highest torque in the brake range
- the rule regarding Z_2=odd slot numbers is not so strict for high pole numbers. In that case, *there are* odd slot numbers that do not create r=1 force wave, and some of them that neither r=1 nor r=3 force wave: the former might be used, the latter are *expressly recommended* slot numbers. The rule q_1-1/2≤q_2'≤q_1+1/2 is also not so strict for high pole numbers and high phase numbers.
- there are special situations where further considerations apply:
- if the stator winding also creates even harmonics, such as some pole changing winding, q_2'<q_1 must be selected to avoid the high asynchronous parasitic torque created by the stator harmonic ν_a=4 in the motor range
- q_2'>q_1 should be selected to achieve lower synchronous parasitic torques and radial magnetic forces (noise)
- q_2'<1.25q_1 should be selected to avoid troublesome asynchronous parasitic torques
- finally: if the actual ν_b happens to be a slot harmonic with $\xi_{1\nu b}$=ξ_1 winding factor, the sequence of selection established above is changed: the concerned rotor slot number, which otherwise would belong to the range of recommended slot numbers, must be transferred to the prohibited ones
- since there is no rotor slot number that does not create synchronous parasitic torque, the design starts with checking the stator natural frequency for force wave order r=0.

7. Behavior of synchronous parasitic torques during run-up and at operating speed

As already found in [20] and cited in [15], the asynchronous machine with a squirrel cage rotor is to be modeled with small asynchronous machines ([15] Figure 2.) and *small synchronous machines* in shaft connection with the main motor in order to take into account the MMF harmonics. Now, for a deeper understanding of the behavior of synchronous parasitic torques, the small synchronous machines will be defined and their behavior will be studied.

First, we examine the operation of the asynchronous machine "taken hold" by the synchronous parasitic torque; by "taken hold" operation, we mean when the high synchronous parasitic torque does not allow the machine to run up, it either remains in standstill or runs on some s=(ν_b-1)/(ν_b+1) slip ([14] (11)). In this operating status, the usual equivalent circuit diagram of a synchronous machine can be used.

The corresponding element of the differential leakage will correspond to the synchronous reactance $X_d = X_m/\nu_b^2 \cdot \xi_b^2/\xi_1^2$, X_m is the fundamental harmonic magnetizing reactance of the asynchronous main machine. The mains voltage U corresponds to the voltage drop of the stator current on the investigated reactance element of the differential leakage:

$$U = I_1 X_d = I_1 \frac{X_m}{\nu_b^2} \frac{\xi_b^2}{\xi_1^2} \tag{9}$$

The U_p pole voltage corresponds to the voltage drop caused by the rotor current on a reactance of the same value - since ν_b=±μ_a – as the element above:

$$U_p = I_2' X_d = I_2' \frac{X_m}{\mu_a^2} \frac{\xi_b^2}{\xi_1^2}; \quad I_2' = -I_1 \frac{\xi_a}{\xi_b} \eta_2^2 \tag{10}$$

η_2^2 Jordan's coupling factor (2)

The reactance associated with the rotor voltage U_p *does not appear* even on the extended equivalent circuit diagram ([15] Figure 1); its value is the same as the reactance called X_d because, again, by definition ν_b=±μ_a ; ν_b and ξ_b are the harmonic number and winding factor of the stator MMF harmonic involved in generating the synchronous parasitic torque; μ_a and ξ_a are the rotor harmonic number created by the stator harmonic ν_a and the stator harmonic winding factor ξ_a. The multiplier of I_1 takes into account that $\nu_a \neq \nu_b$, so ξ_a and ξ_b may differ. If we did not take this into account, contrary to our intention, we would calculate the quantities of the asynchronous parasitic torque.

Let's start our investigation with the simplest case, when ν_b=μ_a (and both are positive) that is, the torque is generated in standstill.

Maximum power

$$P = \frac{U_1 U_2'}{X_d} = I_1^2 \eta_2^2 \frac{X_m}{\nu_b^2} \frac{\xi_a \xi_b}{\xi_1^2} = I_1^2 \frac{\xi_a}{\xi_b} X_d \tag{11}$$

The torque of the small synchronous machine is created by the field of the harmonic ν_b with angular velocity ω_0/ν_b, therefore

$$M = \frac{Pm}{\omega_0/\nu_b p} = \frac{m I_1^2 \eta_2^2}{\omega_0/\nu_b p} \frac{X_m}{\nu_b^2} \frac{\xi_a \xi_b}{\xi_1^2} \tag{12}$$

where m phase number
p pole pair number
ω_0 electrical angular velocity of supply net

Fundamental harmonic breakdown torque and stator current now being equal to starting current

$$M_{break} = \frac{p}{\omega_0}\frac{mU^2}{2X_s}\ ; \qquad I = \frac{U}{X_s} \tag{13}$$

where U net voltage
X_s leakage reactance of (main) motor

Torque of the small synchronous motor

$$M = \frac{M_{synchr}}{M_{break}} = \frac{mU^2/X_s^2\eta_2^2}{\omega_0/\nu_b p}\frac{X_m}{\nu_b^2}\frac{\xi_a\xi_b}{\xi_1^2}\frac{\omega_0 2X_s}{pmU^2} = 2\frac{X_m}{X_s}\frac{\eta_2^2}{\nu_b}\frac{\xi_a\xi_b}{\xi_1^2} \tag{14}$$

Thus, our previously derived formula is verified here using another method of derivation, see [13] (13).

Let's examine what happens when the machine somehow starts, runs up and then runs at rated speed. Then the poles of the rotor rotate in space under the poles of the stator, meaning that this small machine is "out of synchronism".

The precise investigation cannot be performed on the basis of the extended equivalent circuit diagram either, for this we have to go back to the basic relationships of the unified electric machine theory. The simplest way to start is from Figure 3 ([21] p. 111), later we will also introduce three-phase space vector considerations.

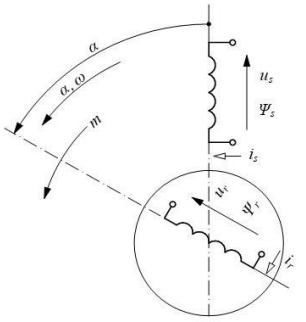

Figure 3: Two-winding basic slipring machine [21] p. 111.

Basic equations

$$u_s = i_s R_s + \frac{d\Psi_s}{dt} \qquad \Psi_s(\alpha,t) = l_s(\alpha)i_s + l_m(\alpha)i_r \tag{15}$$

$$u_r = i_r R_r + \frac{d\Psi_r}{dt} \qquad \Psi_r(\alpha,t) = l_m(\alpha)i_r + l_m(\alpha)i_r$$

$$\alpha(t) \qquad i(t)$$

$$u_s = i_s R_s + l_s\frac{di_s}{dt} + l_m\frac{di_r}{dt} + \omega i_s\frac{dl_s}{d\alpha} + \omega i_r\frac{dl_m}{d\alpha} \tag{16}$$

$$u_r = i_r R_r + l_r\frac{di_r}{dt} + l_m\frac{di_s}{dt} + \omega i_r\frac{dl_r}{d\alpha} + \omega i_s\frac{dl_m}{d\alpha}$$

$$m = \frac{1}{2}i_s^2\frac{dl_s}{d\alpha} + \frac{1}{2}i_r^2\frac{dl_r}{d\alpha} + i_s i_r\frac{dl_m}{d\alpha}$$

In (16), the first two induced voltages are the so-called transformer voltages, and the other two ones represent voltages due to rotation.

We are examining a cylindrical machine, therefore $dl_s/d\alpha=0$, $dl_r/d\alpha=0$. The dynamic phenomena that occur are not examined now ($d\omega/dt=0$). As an approximation and simplification, we also neglect resistances: this is a legitimate approach especially for low, dangerous ν_b harmonics. The perceptible synchronous parasitic torques generated in standstill are created by slot harmonics – this can be verified theoretically ([17], [18] Appendix) - therefore $\xi_b=\xi_a=\xi_1$.

First, the synchronous operation in standstill will be checked: $\omega=0$, α=const. The equations

$$u_s = l_s\frac{di_s}{dt} + l_m\frac{di_r}{dt}$$
$$u_r = l_r\frac{di_r}{dt} + l_m\frac{di_s}{dt} \tag{17}$$
$$m = i_s i_r\frac{dl_m}{d\alpha}$$

Since the MMF of both the stator and the rotor exerts its effect on the same path, $l_s=l_r=l_m=L=1/\omega_0\cdot X_m/\nu_b^2$ apart from the leakage to be interpreted for the actual small synchronous machine. The mutual inductance depends on the angle of the rotor position related to one rotor slot pitch: $l_m=L\cdot\cos\alpha=L\cdot e^{j\alpha}$.

Substituting and taking into account that the (excitation) currents are of 50 Hz and the system operates under forced current (i_s=const., i_r=const.), at a certain angle α of the rotor position, the equations in the own coordinate system of both the stator and the rotor

$$u_s = i_s j\frac{X_m}{\nu_b^2} + i_r\cos\alpha j\frac{X_m}{\nu_b^2} = j\frac{X_m}{\nu_b^2}(i_s + i_r e^{j\alpha})$$
$$u_r = i_r j\frac{X_m}{\nu_b^2} + i_s\cos\alpha j\frac{X_m}{\nu_b^2} = j\frac{X_m}{\nu_b^2}(i_r + i_s e^{-j\alpha}) \tag{18}$$
$$m = i_s i_r\frac{X_m}{\nu_b^2}(-\sin\alpha) = i_s i_r j\frac{X_m}{\nu_b^2}e^{j\alpha}$$

Equations of a synchronous machine are obtained. The maximum torque occurs at $\alpha=\pi/2$, in which case also i_s and i_r are perpendicular to each other, consequently, as in the usual vector diagram of a synchronous machine, u_s and u_r that means U and U_p are also perpendicular to each other. Omitting the derivation, our original formulas ([13] (13)) can also be derived in this way.

The examination of the synchronous torque during rotation will be omitted, the result is the same.

Next, the machine is investigated during start-up. This requires a more precise formulation of the task, since here in addition to transformer voltages, so called rotational voltages also appear. Although these are also included in the equations of the basic machine, we still choose the full three-phase vector theory method; within this, the common coordinate system attached to the stator is expedient [21] (10-19).

The basis of our calculation is [19] (309), according to which the rotor MMF creates the following induction harmonic wave

$$b_{\mu_a} = B_{\mu_a} \sin(1+(\mu_a-\nu_a)(1-s)\omega_0 t) = B_{\mu_a} \sin(\omega_0 t + eZ_2/p\cdot(1-s))\omega_0 t \quad (19)$$

where s slip of rotor of the main machine

The formula was derived based on equations reduced to the stator, i.e. it was written in a coordinate system fixed to the stator. The formula takes into account that the number of poles of the small synchronous machine has increased by a factor of eZ_2/p compared to the number of poles of the basic machine.

The stator current is written in the form

$i_s e^{j\omega_0 t}$

where ω_0 is the angular velocity of the mains voltage according to the fact that harmonics ν_b of the stator MMF induce a mains frequency voltage. The harmonic field of the stator ν_b itself rotates with a *mechanical* speed ω_0/ν_b, the harmonic field of the rotor μ_a rotates with the *same speed* compared to the rotor, ω_0/μ_a; therefore, if the rotor is in standstill ($\omega=0$), the stator and the rotor fields are able to generate a constant torque. The rotor current is written in the form

$i_r e^{j(\omega_0 t+eZ_2/p\cdot\omega_0 t)}$

The description is further simplified by the substitution $\alpha=eZ_2/p\cdot(1-s)$.

Flux equations

$$\Psi_s = i_s e^{j\omega_0 t} L_s + i_r e^{j\omega_0 t} e^{j\alpha\omega_0 t} L_m \quad (20)$$

$$\Psi_r = i_s e^{j\omega_0 t} L_m + i_r e^{j\alpha\omega_0 t} L_r$$

The induced voltages are written in the *transformed* form

$u\cdot e^{-j\omega_0 t}$

for the sake of a simple equation:

$$u_s e^{-j\omega_0 t} = \frac{d\Psi_s}{dt} e^{-j\omega_0 t} = i_s\, j\omega_0 L_s + i_r(1+\alpha)\, j\omega_0 e^{j\alpha\omega_0 t} L_m \quad (21)$$

$$u_r e^{-j\omega_0 t} = \left(\frac{d\Psi_r}{dt} - j\omega\Psi_r\right)e^{-j\omega_0 t} =$$

$$= i_s\, j\omega_0 L_m + i_r(1+\alpha)\omega_0\, j e^{j\alpha\omega_0 t} L_r - j\alpha\omega_0 i_s L_m - j\alpha\omega_0 i_r e^{j\alpha\omega_0 t} L_r =$$

$$= i_s(1-\alpha)\, j\omega_0 L_m + i_r\, j\omega_0 e^{j\alpha\omega_0 t} L_r$$

where the rotation speed ω of the rotor, due to the increase in the number of poles, is equivalent to the expression $\omega=\alpha\cdot\omega_0$.

Since the arrangement operates under forced current, the voltage is the output, resulting value. It can be seen that both the stator and the rotor have a rotational voltage of significant magnitude and frequency $\alpha\cdot f_{net}$. *This αtimes frequency is the reason why this whole phenomenon does not appear in the equivalent circuit even expanded with harmonic reactance.*

Near rated speed: $1+\alpha\approx 1-\alpha\approx e\cdot Z_2/p = e\cdot 2mq_2'$

The voltage: $u\approx i\cdot e\cdot 2mq_2'\cdot\omega_0\cdot L_m/\nu_b^2$

The torque is the vector product of the stator flux and the stator current (the operator *x* is intended to indicate this)

$$m = \Psi_s x i_s = i_s e^{j\omega_0 t} L_s x i_s e^{j\omega_0 t} + i_r e^{j\omega_0 t} e^{j\alpha\omega_0 t} x i_s e^{j\omega_0 t} L_m = \ldots =$$

$$= i_s i_r e^{j\alpha\omega_0 t} L_m = i_s i_r L_m \sin(\alpha\omega_0 t) \quad (22)$$

This torque is created in standstill if sign of ν_b and μ_a – that means rotation directions of stator and rotor - are identical in space: $\nu_b>0$, $\mu_a>0$ or $\nu_b<0$, $\mu_a<0$.

If the torque is created in rotation there are two possibilities.

If μ_a is negative (because $e<0$), necessarily $\nu_b>0$, the torque is created in the motoric range. Space rotation of rotor current shall be written as

$i_r e^{-(j\omega_0 t+\alpha\omega_0 t)}$

and the torque

$$m = i_s i_r L_m \sin((2-\alpha))\omega_0 t \quad (23a)$$

If μ_a is positive (because $e>0$), necessarily $\nu_b<0$, the torque is created in the brake range. Space rotation of stator current shall be written as

$i_s e^{-j\omega_0 t}$

and the torque

$$m = i_s i_r L_m \sin((2+\alpha))\omega_0 t \quad (23b)$$

The pulsating torque with constant peak means a linearly increasing peak power during the run-up, which is maintained by the also linearly increasing rotational induced voltage.

The voltage and torque oscillation frequencies are usually in the range of 600 Hz to 2000 Hz.

If the signs of μ_a and ν_b are different, the factor ξ_a/ξ_b must not be omitted.

Frequencies in (23), (23a) and (23b) correspond to the values summarized in the small table on p. 419 of [16], the latter shows the frequencies of the radial magnetic forces. This correspondence shows the *inherent* connection between the two phenomena. Since both derivations start from the *same* formula [19] (309), the results cannot be different.

If we calculate the synchronous parasitic torques created by the fundamental harmonic stator excitation, the rotor current is with a good approximation $i_r=-i_s\cos\varphi$, where φ is the angle between the rated voltage and rated current of the machine; otherwise $i_r=-i_s$.

To be substituted:

$I_s\approx 5$ p.u. starting current in the speed range of $s=1-s_{break}$

this means that in case of a possibly unfavorable rotor slot number, the high parasitic torque will oscillate with increasing frequency, but *of the same magnitude* (and the noise component resulting from the radial force occurring along with it) practically exists until the breakdown torque is reached

$I_s=1$ p.u. rated current on s_{rated} rated slip

$L_m=1/\omega_0\cdot X_m/\nu_b^2$ where $X_m\approx 3$ p.u.

Magnitude of induced voltage as example for

$e\cdot 2mq_2'=12$ and $\nu_b=13$ critical harmonic

resulting in very high synchronous parasitic torque

the range $s=1-s_{break}$ $u<5\cdot12\cdot3/13^2=1.06$ p.u.
on s_{rated} rated slip $u\approx1\cdot12\cdot3/13^2=0.21$ p.u.

8. Suitable Rotor Slot Numbers for Low-Noise 3-Phase and 5-Phase Machines

A radial force wave is directly related to the machine's magnetic energy through the proportionality factor C (3a), (3b). The magnitude of the same radial force wave has a natural relationship with its emission as noise power. Therefore, the expression of the proportionality factor C in dB does have a relation to the power of the noise excited by the respective force wave and with its human perception.

A part of Table 2. and Table 6. is repeated and put together below in Table 7. with C factors, therefore, re-calculated in dB; the 5-phase part is conveniently re-arranged. In both cases, the tables show only the largest components. The abbreviation n.a. in some cells means a very low level.

Of course, expressing the factor C (especially that of multiplied by an arbitrary number of 10^4) in dB has no any meaning in physic. Conclusions can and should be drawn not from the absolute values, but from the *difference* in the values expressed in dB on the same way as done generally with the noise power; also when used them for comparison of 3-phase and 5-phase machines.

Table 7: Proportionality Factors, Expressed in dB, for 3-Phase and 5-Phase Machines

Relative rotor slot number q_2'	Operation	C proportionality factor for radial magnetic force wave density f [N/m^2] ·10000 in dB			Relative rotor slot number q_2'	C proportionality factor for radial magnetic force wave density f [N/m^2] ·10000 in dB		
		q_1=2	q_1=3	q_1=4		q_1=2	q_1=3	q_1=4
q_1-2+**2/3**	motor	x	14,2	2,1				
	brake		11,7	7,4				
	standstill		3,7	9,2				
q_1-2+**5/6**	motor	x	-0,2	-3,4				
	brake		6,1	0,1				
	standstill		-3,1	n.a.				
q_1-1+**1/6**	motor	17,6	4,5	-0,4	q_1-2+**9/10**	x	-0,8	-6,6
	brake	4,9	5,3	-4,6	q_1-1+**1/10**	13,5	-1,5	-6,8
	standstill	4,4	-4,6	n.a.	q_1+**9/10**	4,5	-7,4	-11,0
q_1-1+**1/3**	motor	17,2	11,1	7,6	q_1-2+**4/5**	x	4,9	0,8
	brake	9,5	3,2	-0,3	q_1-1+**1/5**	11,1	4,6	0,9
	standstill	15,3	0,8	1,2	q_1+**4/5**	2,7	-0,8	-3,0
q_1+**2/3**	motor	4,3	-0,2	-2,8	q_1-2+**3/5**	x	10,1	2,0
	brake	9,5	6,1	3,9	q_1-1+**2/5**	5,9	-3,5	-6,8
	standstill	9,2	-5,2	-1,7	q_1+**3/5**	1,6	-0,2	-9,2
q_1+**5/6**	motor	-2,4	0,6	-8,0	q_1-2+**7/10**	x	-5,7	-4,2
	brake	9,0	-1,0	-4,4	q_1-1+**3/10**	2,0	0,8	-6,0
	standstill	-3,4	n.a.	n.a.	q_1+**7/10**	-4,2	-3,6	-9,2
					q_1**±1/2**	7,0	-3,0	-10,0

Let us take an example of comparing rotor slot numbers q_1=2, q_2'=q_1-1+1/3 vs. q_2'=q_1+5/6 in 3-phase. The C factors expressed in dB are for the first case number 17.2 dB, 9.5 dB, 15.3 dB, respectively, those for the second one are -2.4 dB, 9.0 dB, -3.4 dB, respectively. The *difference* between the noise excitation powers of the three power waves highlighted here are 19.6 dB, 0.5 dB, 18.7 dB, respectively. From this, the expected noise level *difference* of the two rotor slots compared to each other can really be deduced. Therefore the latter will exert much less noise because this short analysis is clearly highlighted the difference between the largest three of the many radial magnetic force waves generating the largest noise pressure waves; although the rest of waves further the frequencies of them are not included in the analysis at the moment, the conclusion is still valid.

Based on the above, a proposal is made hereby to introduce a general *Noise Component Equivalence Measure*. General definition

$$NCEM = 10\lg 10^4 \frac{\xi_{1\nu a}\xi_{1\nu b}}{\nu_b \mu_a}\eta_{2a}^2 \frac{1}{\xi_1^2} \tag{24}$$

for the noise component created by the fundamental harmonic only, appr.

$$NCEM = 10\cdot\lg 10^4 \frac{\xi_{1\nu b}}{\nu_b \mu_a} \tag{24a}$$

Here ξ, ν, μ and η^2 are real physical quantities. The 10^4 factor has no any physical meaning; its role is only that the resulting numerical value results in an order of magnitude convenient for human perception. Table 7 shows that a large positive value of the metric indicates a dangerous noise component, therefore the relevant slot number is not recommended, while a small positive and mainly a negative value is harmless and therefore indicates a recommended slot number. By calculating the metric for each significant excitation force wave and then including it in a single table, a complete, comprehensive and transparent picture of rotor slot number under investigation is obtained, which is thus more suitable than ever any previous method for judging the respective slot number. Those slot numbers that show high NCEM numbers are not worth investigating further with more advanced methods. We note that the applied factor could have been chosen just as arbitrarily for 10^{12}, so that the metric falls within the range of usual noise levels; this would give, however, the false impression, that the formula actually gives the expected noise level itself, indeed, so we deliberately do not do this.

$Z_2>Z_1$ is always recommended rather than $Z_2<Z_1$ from noise point of view [14].

Here too, we note that the reason for the outstanding values occurring in some cells in the tables is that the corresponding ν_b happens to be a slot harmonic.

It is strikingly apparent that, in 3-phase in case of some popular slot numbers, low-noise operation cannot be expected at all due to the noise component caused by the high synchronous torque component during brake mode; it is a torque that is not perceived during normal start-up and therefore generally not taken notice of, no attention is paid to it.

8.1. Design process of low-noise induction machines, evaluation of rotor slot number

The method is presented for a three-phase, 4-pole machine with a rotor slot number Z_2=28, which is otherwise inexplicably popular acc. to opinion of the author.

The design process starts with Table 1, which shows the synchronous parasitic torques generated in the case of the investigated rotor slot number, in order to check whether the machine will be able to run up at all. The chosen q_2'=2+1/3 relative number of slots in 4 poles means just Z_2=28 rotor slot

number. The table also provides some preliminary information by calculating the noise proportionally factor for the components created by the radial magnetic forces corresponding to the synchronous parasitic torques.

Table 8: Order Number and Frequency (at 50 Hz) of Radial Magnetic Force Waves Generated by Rotor Slot Numbers, in 3-phase, 4-pole Machines; just investigated Z_2=28 Rotor Slot Number Highlighted

				p=	2												
				r=	0			r=	1	r=	2	r=	3	r=	4		
				+	-			+	-	+	-	+	-	+	-		
q_1	Z_1	ν_b	ν'_b			μ_a	μ_a									μ_a	μ_a
2	24	-11	-22	20	24			21	25	22	26	23	27	24	28		-13
			freq.	600	600			625	625	650	650	675	675	700	700		
		-11	-22	20	24			19	23	18	22	17	21	16	20		
			freq.	600	600			575	575	550	550	525	525	500	500		
		13	26	28	24	-13		29	25	30	26	31	27	32	28		15
			freq.	600	600			625	625	650	650	675	675	700	700		
		13	26	28	24	-13		27	23	26	22	25	21	24	20		
			freq.	600	600			575	575	550	550	525	525	500	500		
3	36	-17	-34	32	36			33	37	34	38	35	39	36	40		
			freq.	900	900			925	925	950	950	975	975	1000	1000		
		-17	-34	32	36			31	35	30	34	29	33	28	32	15	
			freq.	900	900			875	875	850	850	825	825	800	800		
		19	38	40	36			41	37	42	38	43	39	44	40		
			freq.	900	900			925	925	950	950	975	975	1000	1000		
		19	38	40	36			39	35	38	34	37	33	36	32		
			freq.	900	900			875	875	850	850	825	825	800	800		
4	48	-23	-46	44	48			45	49	46	50	47	51	48	52		
			freq.	1200	1200			1225	1225	1250	1250	1275	1275	1300	1300		
		-23	-46	44	48			43	47	42	46	41	45	40	44		
			freq.	1200	1200			1175	1175	1150	1150	1125	1125	1100	1100		
		25	50	52	48			53	49	54	50	55	51	56	52	-27	
			freq.	1200	1200			1225	1225	1250	1250	1275	1275	1300	1300		
		25	50	52	48			51	47	50	46	49	45	48	44		
			freq.	1200	1200			1175	1175	1150	1150	1125	1125	1100	1100		
5	60	-29	-58	56	60	29		57	61	58	62	59	63	60	64		
			freq.	1500	1500			1525	1525	1550	1550	1575	1575	1600	1600		
		-29	-58	56	60	29		55	59	54	58	53	57	52	56		-27
			freq.	1500	1500			1475	1475	1450	1450	1425	1425	1400	1400		
		31	62	64	60			65	61	66	62	67	63	68	64	-33	33
			freq.	1500	1500			1525	1525	1550	1550	1575	1575	1600	1600		
		31	62	64	60	-31	31	63	59	62	58	61	57	60	56		29
			freq.	1500	1500			1475	1475	1450	1450	1425	1425	1400	1400		
7	84	-41	-82	80	84		-41	81	85	82	86	83	87	84	88	43	
			freq.	2100	2100			2125	2125	2150	2150	2175	2175	2200	2200		
		-41	-82	80	84		-41	79	83	78	82	77	81	76	80		
			freq.	2100	2100			2075	2075	2050	2050	2025	2025	2000	2000		
		43	86	88	84		43	89	85	90	86	91	87	92	88		
			freq.	2100	2100			2125	2125	2150	2150	2175	2175	2200	2200		
		43	86	88	84		43	87	83	86	82	85	81	84	80	-41	
			freq.	2100	2100			2075	2075	2050	2050	2025	2025	2000	2000		
9	108	-53	-106	104	108			105	109	106	110	107	111	108	112		-55
			freq.	2700	2700			2725	2725	2750	2750	2775	2775	2800	2800		
		-53	-106	104	108			103	107	102	106	101	105	100	104		
			freq.	2700	2700			2675	2675	2650	2650	2625	2625	2600	2600		
		55	110	112	108	-55		113	109	114	110	115	111	116	112		57
			freq.	2700	2700			2725	2725	2750	2750	2775	2775	2800	2800		
		55	110	112	108	-55	55	111	107	110	106	109	105	108	104		
			freq.	2700	2700			2675	2675	2650	2650	2625	2625	2600	2600		
11	132	-59	-118	116	120			117	121	118	122	119	123	120	124		
			freq.	3000	3000			3025	3025	3050	3050	3075	3075	3100	3100		
		-59	-118	116	120			115	119	114	118	113	117	112	116	57	
			freq.	3000	3000			2975	2975	2950	2950	2925	2925	2900	2900		
		61	122	124	120			125	121	126	122	127	123	128	124		
			freq.	3000	3000			3025	3025	3050	3050	3075	3075	3100	3100		
		61	122	124	120			123	119	122	118	121	117	120	116		
			freq.	3000	3000			2975	2975	2950	2950	2925	2925	2900	2900		
		-65	-130	128	132			129	133	130	134	131	135	132	136		
			freq.	3300	3300			3325	3325	3350	3350	3375	3375	3400	3400		
		-65	-130	128	132			127	131	126	130	125	129	124	128		
			freq.	3300	3300			3275	3275	3250	3250	3225	3225	3200	3200		
		67	134	136	132			137	133	138	134	139	135	140	136	-69	
			freq.	3300	3300			3325	3325	3350	3350	3375	3375	3400	3400		
		67	134	136	132			135	131	134	130	133	129	132	128		
			freq.	3300	3300			3275	3275	3250	3250	3225	3225	3200	3200		
12	144	-71	-142	140	144	71		141	145	142	146	143	147	144	148		
			freq.	3600	3600			3625	3625	3650	3650	3675	3675	3700	3700		
		-71	-142	140	144	71		139	143	138	142	137	141	136	140		-69
			freq.	3600	3600			3575	3575	3550	3550	3525	3525	3500	3500		
		73	146	148	144			149	145	150	146	151	147	152	148		
			freq.	3600	3600			3625	3625	3650	3650	3675	3675	3700	3700		
		73	146	148	144			147	143	146	142	145	141	144	140		71
			freq.	3600	3600			3575	3575	3550	3550	3525	3525	3500	3500		
14	168	-83	-166	164	168		-83	165	169	166	170	167	171	168	172	85	
			freq.	4200	4200			4225	4225	4250	4250	4275	4275	4300	4300		
		-83	-166	164	168		-83	163	167	162	166	161	165	160	164		
			freq.	4200	4200			4175	4175	4150	4150	4125	4125	4100	4100		
		85	170	172	168		85	173	169	174	170	175	171	176	172		
			freq.	4200	4200			4225	4225	4250	4250	4275	4275	4300	4300		
		85	170	172	168		85	171	167	170	166	169	165	168	164	-83	
			freq.	4200	4200			4175	4175	4150	4150	4125	4125	4100	4100		

Then Table IV. of [16] follows being *essential* for any noise calculation. Such a table is required for each pole number.

The table for 4 pole is repeated now as Table 8., omitting the parts of no interest at the moment, highlighting the rotor slot number Z_2=28 and integer multiple thereof.

The cell of the table in which the investigated slot number or its integer multiple appears creates a radial force wave with the corresponding *r* order number, with the frequency under it (in the case of 50 Hz power supply). As it is well known, the harmonic ν_b appearing not only in the row of the actual q_1 but also in the row of integer multiples thereof are also slotharmonics.

The table was supplemented with the μ_a induction wave harmonic produced by the investigated rotor slot number. In the table - although it was compiled by itself, independently of other tables -, the correlation between the synchronous parasitic torques and the radial magnetic forces stands out, and even that the radial force wave originates from the torque occurring in the rotation or in standstill (the latter always in pairs). The investigated rotor slot number, in addition to the always-occurring r=0 force waves, happens to only create r=4 force waves. Skipping the details: "of 1/3q" and "of 2/3q" rotor slot numbers only create r=0, 4 order numbers, while "of 1/6q", "of 1/2q" and "of 5/6q" rotor slot numbers create r=0, 2, 4 order numbers in 4 poles.

There is no other task than to insert the rest of force waves found here, order r>0, into Table 1, obtaining Table 9.

Table 9: Harmonics of a Three-Phase Machine, the Created Synchronous Parasitic Torques and NCEM Values for the Case of 4 poles,
q_2' = 2 1/3 (Z_2=28) Relative Rotor Slot Number

m=	3	ν_b				q_1			Synchronous Torque / Breakdown Torque			Noise Component Equivalence Measure			Freq.
q_2	+1/3	$\nu_b=\mu_a$	$\nu_b=\mu_a$	operation	order nr.	q_1=2	q_1=3	q_1=4	q_1=2	q_1=3	q_1=4	q_1=2	q_1=3	q_1=4	Hz
	e	ν_b	μ_a		r=										
2	-1	13		motoric	0	ξ_{slot}			-2,23	0,50	0,29	17,57	11,10	8,73	600
	-1	-11	13		4	ξ_{slot}						18,30	10,94	9,45	700
	1	13	15		4	ξ_{slot}						16,95	10,48	8,11	700
	1	-17	15		4		ξ_{slot}					10,06	15,76	7,91	800
	-2	25	-27		4	ξ_{slot}		ξ_{slot}				11,56	4,20	11,52	1300
	-2	-29	-27		4							5,19	3,55	4,19	1400
	2	-29		break	0				-0,27	0,18	0,21	4,88	3,24	3,88	1500
	2	31	29		4							4,59	3,84	2,44	1400
	3	-41	43		4							1,67	0,91	-0,49	2200
	-3	43	41		4							1,67	0,03	0,66	2000
	-3		-41	standstill	0				≈0	≈0	≈0	≈0	≈0	≈0	2100
	3		43												
	-4	-53	-55		4		ξ_{slot}					-0,52	5,18	-1,52	2800
	4	55	57		4		ξ_{slot}					-0,83	4,86	-2,99	2800
	-4	55		motoric	0		ξ_{slot}		-0,14	0,52	-0,09	-0,68	5,01	-2,83	2700
	4	-59	57		4	ξ_{slot}						4,43	-2,04	-4,41	2900
	-5	67	-69		4							-2,39	-3,15	-3,40	3400
	-5	-71	-69		4	ξ_{slot}	ξ_{slot}	ξ_{slot}				2,82	2,80	2,79	3500
	5	-71		break	0	ξ_{slot}	ξ_{slot}	ξ_{slot}	-0,41	-0,41	0,40	2,82	2,80	2,79	3600
	-5	73	71		4	ξ_{slot}	ξ_{slot}	ξ_{slot}				2,58	2,56	2,55	3500
	6	-83	85		4	ξ_{slot}						1,47	-5,89	-7,38	4300
	-6	85	-83		4	ξ_{slot}						1,26	-5,21	-7,58	4100
	-6		-83	standstill	0	ξ_{slot}			0,35	≈0	≈0	1,47	≈0	≈0	4200
	6		85						-0,34			1,26			
	-9		-125	standstill	0		ξ_{slot}		≈0	-0,23	≈0	≈0	-2,12	≈0	6300
	9		127							0,23			-2,25		
	-12		-167	standstill	0	ξ_{slot}		ξ_{slot}	-0,17	≈0	0,17	-4,60	≈0	-4,64	8400
	12		169						0,17		-0,17	-4,71		-4,75	

With Table 9., the *final table as the very point of present development* was achieved, which provides the radial excitation force spectra exactly corresponding to the noise spectra to be measured later in the Testroom. This table thus actually, *numerically*, provides a basis for the design engineer's decision regarding the rotor slot number investigated. For this very purpose, the values of the synchronous parasitic torque were let remain in the table.

Table 9. confirms our previous view that the average noise pressure level of the machine established in the factory test room is actually caused by only a few low order harmonics, therefore it is usually sufficient to work with a table smaller (less harmonics that means less row) than Table 9.

The table cannot be as general and comprehensive as Table 1. or Table 5., this can only apply to a single rotor slot number. However, the stator slot number can be arbitrary; all that is required is to insert the relevant winding factors in a suitable way. For other pole numbers, the additional tables published in [16] should be used or to create with little investment of time.

Finally, the resonance frequencies must be checked so that the resonance does not unduly amplify even one single component. The resonance frequencies depend on the machine size; it is an old knowledge (Jordan, Heller) that some slot numbers, therefore, may or may not be suitable depending on the size of the machine.

8.2. Effect of rotor skewing on noise

The effect of skew is discussed in detail in [18]. Using our results and new formulas, let's examine the effect of skew *numerically* in Table 10. The calculations were performed for skewing by both the rotor and the stator slot pitch. As expected, the effect of skewing is not uniform, it is different for each component, depending on whether the harmonic causing the respective noise component is a slot harmonic on the stator or not.

Table 10a: Harmonics of a Three-Phase Machine, the Created Synchronous Parasitic Torques and NCEM Values for the Case of 4 poles, $q_2' = 2\ 1/3$ (Z_2=28) Relative Rotor Slot Number with rotor slot skewing *by one rotor slot pitch*; stator winding: full pitch

m=	3	ν_b				q_1			Synchronous Torque / Breakdown Torque			Noise Component Equivalence Measure			Freq.
q_2	+1/3	$\nu_b=\mu_a$	$\nu_b=\mu_a$	operation	order nr.	q_1=2	q_1=3	q_1=4	q_1=2	q_1=3	q_1=4	q_1=2	q_1=3	q_1=4	Hz
	e	ν_b	μ_a		r=										
2	-1	13		motoric	0	ξ_{slot}			-0,17	0,04	0,02	6,39	-0,08	-2,45	600
	-1	-11	13		4	ξ_{slot}						7,12	-0,24	-1,72	700
	1	13	15		4	ξ_{slot}						5,15	-1,32	-3,69	700
	1	-17	15		4		ξ_{slot}					-1,73	3,96	-3,89	800
	-2	25	-27		4	ξ_{slot}		ξ_{slot}				-2,79	-10,15	-2,83	1300
	-2	-29	-27		4							-9,16	-10,80	-10,16	1400
	2	-29		break	0				-0,01	0,01	0,01	-9,78	-11,42	-10,78	1500
	2	31	29		4							-10,07	-10,82	-12,22	1400
	3	-41	43		4							-14,70	-15,46	-16,86	2200
	-3	43	41		4							-14,50	-16,14	-15,50	2000
	-3		-41	standstill	0				≈0	≈0	≈0	≈0	≈0	≈0	2100
	3		43												

Table 10b: Harmonics of a Three-Phase Machine, the Created Synchronous Parasitic Torques and NCEM Values for the Case of 4 poles, $q_2' = 2\ 1/3$ (Z_2=28) Relative Rotor Slot Number with rotor slot skewing *by one stator slot pitch*; stator winding: full pitch

m=	3	ν_b				q_1			Synchronous Torque / Breakdown Torque			Noise Component Equivalence Measure			Freq.
q_2	+1/3	$\nu_b=\mu_a$	$\nu_b=\mu_a$	operation	order nr.	q_1=2	q_1=3	q_1=4	q_1=2	q_1=3	q_1=4	q_1=2	q_1=3	q_1=4	Hz
	e	ν_b	μ_a		r=										
2	-1	13		motoric	0	ξ_{slot}			-0,17	0,17	0,17	6,38	6,38	6,38	600
	-1	-11	13		4	ξ_{slot}						7,11	6,22	7,11	700
	1	13	15		4	ξ_{slot}						9,50	3,29	4,83	700
	1	-17	15		4		ξ_{slot}					2,62	8,57	4,63	800
	-2	25	-27		4	ξ_{slot}		ξ_{slot}				1,56	-2,54	1,86	1300
	-2	-29	-27		4							-4,81	-3,18	-5,47	1400
	2	-29		break	0				-0,03	0,03	0,03	-4,07	-4,07	-4,07	1500
	2	31	29		4							-4,36	-3,47	-5,51	1400
	3	-41	43		4							-9,00	-8,11	-10,15	2200
	-3	43	41		4							-8,79	-9,68	-7,64	2000
	-3		-41	standstill	0				≈0	≈0	≈0	≈0	≈0	≈0	2100
	3		43												

The numerical equalization occurring in Table 10b that means residual synchronous torque after skewing is always the same being independent from q_1 is derived by formula in [18].

It is not to forget that the decreasing factor shall be calculated acc. to μ_a: $\Delta_{rotor} = \sin(\mu_a\beta)/(\mu_a\beta)$

Comparing the tables, it is worth noting that in this case skewing by one rotor slot pitch gives better results.

When calculating the effect of slot skew the modification of the leakage reactance shall also be considered [18]; the tables in section 6.2, however, does not contain this for the moment.

9. Summary

This paper is a synthetic, closing work; our results before and now are sufficient for providing a complete foundation for achieving the final goal, the correct rotor slot number. All 3+1 formulas derided by us before [13], [14], [18] have been used for the purpose.

The tables developed in [16] for three-phase machines were further developed by substitution of the data of a typical machine into our formulas. We then used all of these to select the rotor slot number for the increasingly common 5-phase motors as well. It is shown that inverter fed multiphase motor's rotor slot number must be chosen as if it were a mains-supplied machine.

We worked with a relative rotor slot number and with p.u. data of a typical motor, which enables a systematic and comprehensive approach to the question and the incorporation of the entire range of rotor slot numbers for any pole. We have specified the favorable, acceptable and prohibited relative rotor slot numbers for 3-phase for the most common relative stator slot numbers regarding synchronous parasitic torque. The method can be transferred to 5-phase and any higher number of phases. At this point, a detailed, comprehensive recommendation, actual design rules are given the engineer on a new basis for how to select the rotor slot number for the entire range. The entire investigation relies on the basic law formulated by us that it is the p/r proper fractional part of the relative rotor slot number which determines the behavior of the asynchronous machine.

Then we dealt with the calculation of the noise-exciting radial force waves, in order to check the number of rotor slots resulting in low-noise motors. Relying on our formula, we have defined and introduced what we call the Noise Component Equivalence Measure (NCEM). This made it possible to accurately calculate the comparative spectra of the complete, noise-exciting radial forces; this enables the design engineer to select the most favorable rotor slot number and to exclude the a priori unfavorable rotor slot numbers from further examination.

Using the NCEM value and our results in [18] the effect of the rotor slot skewing was accurately calculated. The effect of skewing is not uniform, but different for each noise component.

In this study, we continued to follow the approach of starting the investigation from the rotor slot number. The reason for this is that the harmonics of the stator MMF (at least when q_1=integer) are always the same; on the contrary, the MMF harmonic order numbers of the rotor *depend* on the rotor slot number. This manner of vision made it possible to recognize relationships and laws that cannot be found in the works so far. The stator slot number affects the processes only to the extent that the actual slot harmonic amplifies some individual torque or noise components and others not, but the basic characteristics are determined by the rotor slot number.

The above summarized results should indicate the direction of further research using more advanced methods and measurements in terms of which rotor slot numbers are worth investigating further and which ones will definitely not be suitable.

With present study the entire range of rotor slot numbers in terms of parasitic torques and radial magnetic forces of all squirrel cage induction motors as a whole is covered on a comprehensive way being not available so far.

The conclusion and contribution to the research consists in the fact that thanks to our new formulas it is possible for the first time to give the machine designer a completely comprehensive, numerical recommendation for the entire range of asynchronous machines, for any size, for each number of poles and for each number of stator slots in order to select the correct number of slots for the rotor. Also for the first time, it was possible to numerically map the radial, noise-generating force waves according to the spectrum measured in the test room, for not skewed and skewed machines.

The entire examination of us on the effects of space harmonics in squirrel cage induction motors has come now to an end.

Acknowledgment

The author gratefully acknowledges the contributions of **István Laczkó**, Chief Engineer of the United Electric Machine Factory, EVIG, Budapest, Hungary, for his valuable comments.

Conflicts of Interest

The author declares no conflicts of interest.

Appendix

MMF harmonics in squirrel cage induction machines

The basic formulas for the order number of MMF space harmonics:

$$\nu_a = 6g_1 + 1 \quad (25a)$$

$$\mu_a = e\cdot Z_2/p + \nu_a = e\cdot 2mq_2' + \nu_a \quad (25b)$$

$$\nu_b = 6g_2 + 1 \quad (26)$$

The rotor harmonics generated by the fundamental MMF harmonic $\nu_a = 1$

$$\mu_a = e\cdot Z_2/p + 1 = e\cdot 2mq_2' + 1 \quad (27)$$

The harmonics of the stator MMF called here ν_b are considered now for $q_1 = 2$, together with the response of the rotor

$\nu_b = -5$	$0<\eta_{2,-5}^2<1$
$\nu_b = 7$	$0<\eta_{2,7}^2<1$
$\nu_b = -11$	$\eta_{2,-11}^2 \approx 0$
$\nu_b = 13$	$\eta_{2,13}^2 \approx 0$

The magnitude of these harmonic fields is attenuated due to response of the rotor by the Δ_ν rotor attenuation factor [19] (269) p. 154:

$\nu_b = -5$	ξ_5	$\xi_5 \cdot \Delta_5 = \xi_5 \cdot (1- \eta_{2,-5}^2)$
$\nu_b = 7$	ξ_7	$\xi_7 \cdot \Delta_7 = \xi_7 \cdot (1- \eta_{2,7}^2)$
$\nu_b = -11$	$\xi_{11} = \xi_1$	$\xi_{11} \cdot \Delta_{11} = \xi_{11} \cdot (1- \eta_{2,-11}^2)$ $(= \xi_1)$
$\nu_b = 13$	$\xi_{13} = \xi_1$	$\xi_{13} \cdot \Delta_{13} = \xi_{13} \cdot (1- \eta_{2,13}^2)$ $(= \xi_1)$

The *apparent* winding factor of the slot harmonics remains the same, as it generates only a small current in the rotor to attenuate it.

The stator harmonics according to (25a) and (26), which are both numerically and physically *identical*, are called ν_a or ν_b according to their roles. If we examine the creation and order number of the harmonics of the rotor, specifically the $\mu_a = f(\nu_a)$ function as (25b), we use the marking ν_a for the stator harmonics; if these are examined by themselves, in a role independent of the order number of the rotor harmonics as in (26), then the marking ν_b is applied to them, as described above. From this marking, it is stated that if among the harmonics of rotor μ_a created by ν_a there is one for which $\nu_b=\pm\mu_a$ and $\nu_b\neq\nu_a$, then these harmonics form a synchronous parasitic torque.

On the other hand, the same harmonics marked as ν_a also create additional rotor harmonics:

$\nu_a = -5$	$\mu_a = e\cdot Z_2/p + \nu_a = e\cdot 2mq_2' - 5$	(28)
$\nu_a = 7$	$\mu_a = e\cdot Z_2/p + \nu_a = e\cdot 2mq_2' + 7$	
$\nu_a = -11$	$\mu_a = e\cdot Z_2/p + \nu_a = e\cdot 2mq_2' - 11$	
$\nu_a = 13$	$\mu_a = e\cdot Z_2/p + \nu_a = e\cdot 2mq_2' + 13$	

By substituting e=0 into formulas (28), we obtain the rotor harmonics that produce asynchronous parasitic torque *in any case*; for these, $\nu_b=\nu_a$. In the author's opinion, instead of equality of harmonics [22], it should be said here that ν_b does not appear in this physical phenomenon, it has no role whatsoever. These currents flow in the small harmonic circuits and are therefore part of the equivalent circuit diagram ([15] Figure 2).

By substituting e=±1, ±2, ±3,. into the formulas (28), we obtain the rotor harmonics that *can* produce synchronous parasitic torque with a ν_b other than ν_a. Only here does ν_b (26) enter this phenomenon. The role, impact and behavior of these fields being out of usual equivalent circuit diagram are presented in Chapter 7.

If $\nu_b=\mu_a$, then the torques are always generated in pairs and in standstill; if $\nu_b = -\mu_a$, the torque is generated “alone” and in rotation.

These further harmonics and their action can be studied "clearly,” they can be separated from the action of the harmonics of the fundamental stator current harmonic if the rotor rotates synchronously. That is, if the rotor is rotated by a synchronous motor powered by the same network with the same number of poles. In this case, no fundamental harmonic rotor current occurs, and only currents generated by the stator harmonics flow. The coincidence of these further μ_a harmonics in (28) with any ν_b harmonic in (26) produces further synchronous parasitic torques and radial magnetic force waves. Therefore, in the proposed testroom arrangement, only these will work; however, they are excited by the low magnetizing current instead of the high starting current. In any case, in case of increased supply voltage (using saturation) upto the rated current, the effect of the investigated phenomenon on the rated operation can be accurately modeled. In most cases, especially with chorded winding the effect of rotor harmonics generated by stator harmonics other than fundamental harmonic is insignificant. In the case of skew they are sure insignificant.

Contrary to the perception so far *it is the q_2’ relative number of rotor slots (see Figure 1.) which determines* at the end *how many* of the infinite number of *harmonics* occurring in the machine acc.

to (28) and their reaction and repeated counter-reaction *should actually be considered* when calculating the asynchronous machine with a cage rotor; the smaller q_2', the less should be considered. The result is that significantly fewer harmonics than those usually applied in by researchers so far.

Conflict of Interest

The author declares no conflict of interest.

References

[1] J. Le Besnerais, *Reduction of Magnetic Noise in PWM-Supplied Induction Machines – Low-Noise Design Rules and Multi-Objective Optimization*, Electric Power, Ecole Centrale de Lille, 2008. HAL: https://theses.hal.science/tel-00348730v1

[2] H. Chen, J. Zhao, Y. Xiong, S. Yan, H. Xu, "An Improved Model for Five-Phase Induction Motor Based on Magnetic Noise Reduction Part II: Pole-Slot Scheme," *Processes*, **10**, 1430, 2022. https://doi.org/10.3390/pr1008143

[3] J. Le Besnerais, V. Lanfranchi, M. Hecquet, P. Brochet, "Optimal Slot Numbers for Magnetic Noise Reduction in Variable-Speed Induction Motors," *IEEE Transactions on Magnetics*, **45(8)**: 3131–3136, 2009. DOI: 10.1109/TMAG.2009.2020736

[4] I. Milažar, D. Žarko, "Influence of Rotor Slot Number on Magnetic Noise in a Squirrel-Cage Induction Motor for Traction Applications," *2021 Int. Conf. on Electrical Drives & Power Electronics (EDPE)*: 243–248, 2021. DOI: 10.1109/EDPE53134.2021.9604100

[5] N. Gyftakis, J. Kappatou, "The Impact of the Rotor Slot Number on the Behavior of the Induction Motor," *Advances in Power Electronics*, Volume 2013, Article ID 837010. http://dx.doi.org/10.1155/2013/837010

[6] G. Joksimovic, "Optimal Selection of Rotor Bar Number for Minimizing Torque and Current Pulsations Due to Rotor Slot Harmonics in Three-Phase Cage Induction Motors," *IEEE Access*, **8**: 228572–228585, 2020. DOI: 10.1109/ACCESS.2020.3045766

[7] A. Mekahlia, E. Semail, F. Scuiller, T. Hamiti, R. Benlamine, "Effect of Rotor Bar Number on Performance of Five-Phase Induction Machine for Traction," *HAL Open Science*, October 2018.

[8] A. Gautam, O. Ojo, M. Ramezani, O. Momoh, "Computation of Equivalent Circuit Parameters of Nine-Phase Induction Motor in Different Operating Modes," *IEEE ECCE*, 2012: 142–149. DOI: 10.1109/ECCE.2012.6342830

[9] L.A. Pereira, S. Haffner, L.F.A. Pereira, R.S. da Rosa, "Comparison of Five Phase and Three Phase Induction Machines of the Same Size," *IECON 2014 – 40th Annual Conf. of the IEEE Industrial Electronics Society*, 2014. DOI: 10.1109/IECON.2014.7048539

[10] A. Marfoli, G. Sala, L. Papini, P. Bolognesi, C. Gerada, "Torque Ripple Investigation in Squirrel Cage Induction Machines," *IEEE IEMDC*, 2019: 140–146. DOI: 10.1109/IEMDC.2019.8785364

[11] J. Otýpka, J. Sobra, R. Pechanek, "The Summary of Induction Motor Torque Ripple Theories for Motor Torque Analysis," *IEEE 21st Int. PEMC*, Sept 2024. DOI: 10.1109/PEMC61721.2024.10726339

[12] K. Yamazaki, K. Shimada, "Torque Ripple Generation Mechanism of Induction Motors by Time and Space Harmonic Fields," *IEEE Transactions on Magnetics*, **59(5)**, May 2023. DOI: 10.1109/TMAG.2023.3261439

[13] G. Kovács, "Calculation of Synchronous Torques and Radial Magnetic Forces for Pole-Changing Winding Using the 3//Y / 3//Y Method," *ICEM 2020*, Gothenburg, Sweden: 90–96, 2020. DOI: 10.1109/ICEM49940.2020.9270765

[14] G. Kovács, "Influence of the Rotor Slot Numbers on the Parasitic Torques and the Radial Magnetic Forces of the Squirrel Cage Induction Motor; an Analytic Approach," *ICEM 2022*, Valencia, Spain. DOI: 10.1109/ICEM51905.2022.9910809

[15] G. Kovács, "Harmonics in the Squirrel Cage Induction Motor; Analytic Calculation; Part I: Differential Leakage, Attenuation, and Asynchronous Parasitic Torques," *CES Transactions on Electrical Machines and Systems*, **7(3)**: 320–329, Sept 2023. DOI: 10.30941/CESTEMS.2023.00034

[16] G. Kovács, "Harmonics in the Squirrel Cage Induction Motor; Analytic Calculation; Part II: Synchronous Parasitic Torques, Radial Magnetic Forces," *CES Transactions on Electrical Machines and Systems*, **7(4)**: 404–421, Dec 2023. DOI: 10.30941/CESTEMS.2023.00035

[17] G. Kovács, "Harmonics in the Squirrel Cage Induction Motor; Analytic Calculation; Part III: Influence on the Torque-Speed Characteristic," *CES Transactions on Electrical Machines and Systems*, **8(1)**, Mar 2024. DOI: 10.30941/CESTEMS.2024.00006

[18] G. Kovács, "The Effect of Rotor Slot Skew on the Synchronous Parasitic Torque of the Squirrel Cage Induction Machine – Based on the True Physical Background; Analytic Calculation," *ASTES Journal*, **10(1)**: 20–36, 2025. https://dx.doi.org/10.25046/aj100104

[19] R. Richter, *Elektrische Machinen, Vierter Band, Die Induktionsmaschine*, Springer Verlag, 1936, 1950.

[20] B. Heller, V. Hamata, *Harmonic Field Effects in Induction Machines*, Elsevier Scientific Publishing Company, Amsterdam, Oxford, New York, 1977.

[21] Gy. Retter, *Egységes Villamosgépelmélet*, Műszaki Könyvkiadó, Budapest, 1980.

[22] J. Pyrhönen, T. Jokinen, V. Hrabovcová, *Design of Rotating Electrical Machines*, John Wiley & Sons Ltd., 2007. ISBN: 978-0-470-69516-6